The Dissertation Committee for Marc Stephen Ramirez certifies that this is the approved version of the following dissertation:

A 20-Coil Array System for High-Throughput Dynamic Contrast-Enhanced Mouse MRI

Committee:

James A. Bankson, Supervisor

John D. Hazle, Co-Supervisor

Mia K. Markey

Konstantin V. Sokolov

Ali E. Yilmaz

A 20-Coil Array System for High-Throughput Dynamic Contrast-Enhanced Mouse MRI

by

Marc Stephen Ramirez, B.S.E.E.; M.S.E.E.

Dissertation

Presented to the Faculty of the Graduate School of

The University of Texas at Austin

in Partial Fulfillment

of the Requirements

for the Degree of

Doctor of Philosophy

The University of Texas at Austin

December 2011

Dedication

I dedicate this work to: W.L. Cotton, Arminda P. Stephens-Cotton, Jose H. and Gloria J. S. Ramirez, Daniella R. Meinelt, Carly B. Ramirez, and Ryder B. Ramirez.

Acknowledgements

I would first like to acknowledge my supervisor and mentor Jim Bankson for his knowledge, dedication, vision, support, and guidance while working in his laboratory. I would also like to thank John Hazle for his strong leadership and for serving on my committee. I am grateful to the rest of my committee members, Mia Markey, Kostia Sokolov, and Ali Yilmaz and thank them for their advice, time serving on my committee, and their dedication to higher learning.

I thank my wife Carly Ramirez for her love, patience, and commitment during our time together. I also thank her for our precious son, Ryder. I would like to acknowledge Arminda P. Stephens-Cotton and W. L. Cotton for their generosity and support throughout my life and particularly my academic career. I also acknowledge my wonderful parents Jose and Gloria Ramirez for their endless love and financial support and my sister Daniella Meinelt for always being there for me.

Finally, I wish to thank my core group of friends who have kept life fun and always entertaining, along with colleagues at the University of Texas at Austin, Stanford University, and M. D. Anderson Cancer Center. I particularly thank Dustin Ragan, Emilio Esparza-Coss, Kunal Panda, Charles Kinglsey, Jorge de la Cerda, Douglas Webb, Richard Beaver, Wilma Mason, Georgeanne Moore, Mai Dinh, and Roseann Martinez.

A 20-Coil Array System for High-Throughput Dynamic Contrast-Enhanced Mouse MRI

Publication No._____

Marc Stephen Ramirez, Ph.D.

The University of Texas at Austin, 2011

Supervisor: James A. Bankson

Co-Supervisor: John D. Hazle

MRI is a versatile tool for systematically assessing anatomical and functional changes in small animal models of human disease. Its noninvasive nature makes MRI an ideal candidate for longitudinal evaluation of disease progression in mice; however achieving the desired level of statistical power can be expensive in terms of imaging time. This is particularly true for cancer studies, where dynamic contrast-enhanced (DCE-) MRI, which involves the repeated acquisition of anatomical images before, during, and after the injection of a paramagnetic contrast agent, is used to monitor changes in tumor vasculature. A means of reducing the overall time required to scan multiple cohorts of animals in distinct experimental groups is therefore highly desirable. Multiple-mouse MRI, in which several animals are simultaneously scanned in a common MRI system, has been successfully used to improve study throughput. However, to best utilize the next generation of small-animal MRI systems that will be equipped with an increased number of receive channels, a paradigm shift from simultaneously scanning as

many animals as possible to scanning a more manageable number, at a faster rate, must be considered. Given a small-animal MRI system with 16 available receive channels, the simulations described in this work explore the tradeoffs between the number of animals scanned at once and the number of array elements dedicated to each animal for maximizing throughput. An array system consisting of 15 receive and 5 transmit coils allows throughput-optimized acceleration of a DCE-MRI protocol by a combination of multi-animal and parallel imaging techniques. The array system was designed and fabricated for use on a 7.0-T / 30-cm MRI system, and tested for high-throughput imaging performance in phantoms. Results indicate that up to a nine-fold throughput improvement is possible without sacrificing image quality compared to standard single-animal imaging hardware. A DCE-MRI study throughput improvement of just over six times that achieved with conventional single-mouse imaging was realized. This system will lower the barriers for DCE-MRI in preclinical research and enable more thorough sampling of disease pathologies that progress rapidly over time.

Table of Contents

List of Tables

List of Figures

Chapter 1: Introduction

1.1 Versatility of MRI

Unlike other noninvasive imaging modalities such as projection radiography or computerized tomography (CT), magnetic resonance imaging (MRI) offers the ability to visualize internal body structure with spatial resolutions that are much finer than the wavelength of energy transmitted into the subject and without the use of ionizing radiation. Whereas X-ray modalities offer excellent contrast for bone imaging, MRI excels in the visualization of soft tissues (1). Ultrasound can also be used for soft-tissue imaging, however with less tissue contrast than MRI and requiring an acoustic window from the transducer to the tissue of interest to minimize image reconstruction artifacts.

In many circumstances, detection of physiological changes through functional imaging offers more utility than anatomical visualization alone. Optical imaging can inexpensively provide fast sampling of functional changes and is more portable than MRI, but it has limited ability for noninvasively probing deep tissues (2,3). Position emission tomography (PET) is a functional imaging technique that provides information regarding radioactive tracer distribution. PET suffers from poor resolution and requires integration with another image modality (i.e. CT) for anatomical registration.

MRI is a versatile modality that permits both high-resolution viewing of anatomical structure (4) and functional imaging during a single examination. Spatially localized functional imaging can significantly impact early diagnosis of disease and early detection of therapeutic response (5,6). Cancer, a disease classified by uncontrolled cell growth, destruction of tissue, and spread of diseased cells throughout the body, is the second leading cause of mortality in the United States (7). To help fight this disease, oncologists often rely on the utility of anatomical and functional MRI. Some such

functional techniques involve imaging the brain (8), heart (9), or tumor microvasculature (10). For instance, functional MRI (fMRI) is commonly used to map brain activation locations in response to external stimuli, which can be helpful for preoperative planning for brain tumor surgeries (11). Cardiac MRI (CMRI), in which image series of a beating heart are generated, is often used to detect chemotherapy related cardiac dysfunction (CRCD) by means of measuring ventricular volume changes and ejection fractions (12). Dynamic contrast-enhanced (DCE-) MRI can be used to detect changes in tumor microvasculature and permits efficient evaluation of antiangiogenic cancer drugs that impede the formation of new blood vessels and therefore aim to starve the tumor of nutrients.

1.2 DYNAMIC CONTRAST-ENHANCED MRI

DCE-MRI involves the repeated acquisition of spoiled T_1-weighted anatomical images of disease tissue before, during, and after the intravenous injection of a contrast agent (CA) that is composed of paramagnetic particles of a low molecular weight (13-15). Tissues with a leaky microvasculature, such as tumors with a malformed network of vessels (16), will have CA extravasation into the interstitium (or extravascular extracellular space, EES) and will accumulate CA over time (17,18). The paramagnetic nature of the CA reduces the longitudinal relaxation time (T_1) of the tissue and as a result, tissues that have accumulated CA appear brighter on T_1-weighted images.

With knowledge of the relationship between signal intensity and T_1 contrast through fundamental MR principles, pixel-by-pixel changes in signal intensities over time can be converted into temporal CA concentration curves in the tissue and blood plasma. Semi-quantitative parameters, such as normalized initial area under the curve (NIAUC) (19) or the initial slope of the CA enhancement curves do not have a direct

physiological interpretation but have been successfully used as experimental endpoints (20).

Extraction of the concentration time-course in the blood, known as the arterial input function (AIF), is typically required for robust DCE-MRI analysis of single-tracer experiments. Pharmacokinetic (PK) models are employed to relate the AIF to tissue concentration curves, and characteristics about the tumor microenvironment, including vessel permeability and compartment volume fractions, can be calculated. Quantitative parameters, such as the forward (K^{Trans}) and return (k_{ep}) rate constants, the blood volume fraction (v_b), and the EES volume fraction (v_e) directly reflect physical characteristics (21,22), and have been shown to be more reproducible than parameters from a semi-quantitative analysis (23).

1.3 Challenges of Small-Animal DCE-MRI

DCE-MRI has become a common exploratory tool for evaluating disease status and detecting early indications of response to therapy (24-26). Preclinically, this method is also extremely powerful for use with small animal models of human disease. For instance DCE-MRI can provide a method to track functional changes as disease progresses in normal animals and in animals that have been given experimental therapies. Such longitudinal experiments are critical for therapy evaluation and dose-response testing before the therapies are used in humans. Repeated measurements on the same animal, rather than sacrificing animals at each time point, reduces the number of animals that must be purchased for the experiment and permit robust statistical tests to be used for data analysis. Furthermore, preclinical DCE-MRI offers a vehicle to identify quantitative image-based biomarkers, with potentially direct clinical analogues, that can help identify

when the disease is responding to therapy. Doing so at an early stage can more rapidly personalize treatment plans on a patient-by-patient basis.

Unfortunately, preclinical DCE-MRI is not without its own unique challenges. Mice have a very small blood volume and a rapid cardiovascular cycle compared to humans (27), making accurate estimation of the AIF difficult. A well-accepted method for estimating the AIF in humans is to measure intensity changes in pixels that are contained within blood vessels that are feeding the tissue of interest (28). The faster cardiovascular cycle of mice produces flow artifacts, and the small size of feeding vessels results in partial volume effects, both of which contribute to higher variability in AIF estimation (18,29).

For a given level of sensitivity, high temporal resolution is achieved through sacrifices in the spatial resolution of the acquisition. The signal-to-noise ratio (SNR) can be thought of as a currency for MRI acquisitions that can be spent on combinations of spatial resolution, temporal resolution (or throughput), and/or sensitivity (30). Given constraints in spatiotemporal resolution (31,32), the maximum achievable SNR is unavoidably sacrificed. These tradeoffs illustrate fundamental challenges of preclinical DCE-MRI.

Unfortunately, DCE-MRI also requires a relatively long imaging protocol, typically including positioning, scout setup, and pre-contrast T_1- and T_2-weighted scans followed by a T_1-mapping scan, the DCE-MRI acquisition, and finally a post-contrast T_1-weighted scan. Furthermore, the dynamic acquisition must be long enough to calculate all of the PK modeling parameters of interest (33). The total duration of this protocol, along with animal preparation times, make DCE-MRI a low-throughput experiment. Furthermore, the complexity of the experiment is compounded by fundamentally noisy

data, which in turn requires many animals to be scanned to achieve adequate statistical power. The cost associated with such a study is therefore high, requiring many animals to make up each of several experimental animal groups, long imaging times, and costly experimental therapeutics. Furthermore, the complexity of synchronizing instrument access with multi-stage animal preparation procedures is challenging, particularly if experimental timepoints among animal groups begin to spread across multiple imaging days because of long protocol scan times. These issues can be prohibitive for investigators whose academic focus is on the development of novel cancer therapeutics, and illustrate a problem that is hindering the progress of cancer drug development today (30). Therefore, a solution to improve the throughput of functional MRI studies, and in particular DCE-MRI, is desperately needed to promote the use of MRI for preclinical evaluations of cancer therapies.

1.4 HIGH-THROUGHPUT PRECLINICAL MRI

Improving throughput of MRI acquisitions is a common goal for MRI research. For instance, parallel imaging (PI) (34-39) with phased array coils (40), details of which are in Section 2.2.8, has been developed to reduce scan times. The clinical use of PI improves patient comfort and compliance within the imaging protocol. In preclinical imaging, minimizing the duration a mouse spends on the scanner becomes part of a larger goal to reduce the time required to scan multiple cohorts of animals in distinct experimental groups. Fortunately, the small size of a mouse in relation to the available magnet bore space permits multiple animals to be simultaneously scanned in a single MRI system (30). Many methods have been suggested to accomplish this goal (30,41). One method is to use a large radiofrequency (RF) coil within a single gradient set (42-45). This method (illustrated in Figure 1-1) is cost effective, however the SNR of the

resulting images is reduced since the larger coil is sensitive to all of the lossy subjects that are contained within the coil. Additionally, the imaging speed is only moderately improved since the field-of-view (FOV) must also be scaled with the number of mice simultaneously scanned.

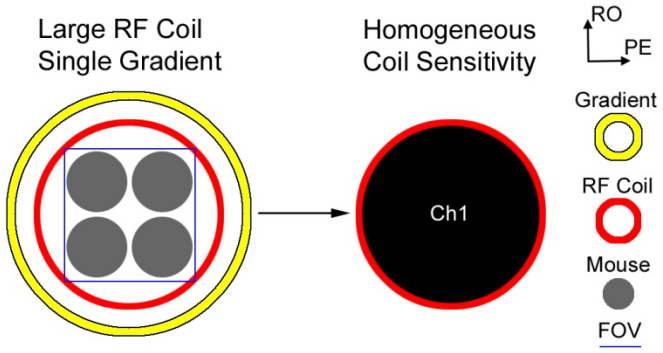

Figure 1-1: Multi-animal MRI with a single RF coil and gradient coil requires a large FOV and matrix size

Another approach to multi-channel MRI uses a multi-coil design in which independent coils are each contained within a separate gradient coil (Figure 1-2) (46). Benefits include independent shimming and uncompromised gradient performance, which allows a vast number of MRI applications to be considered for multi-animal use.

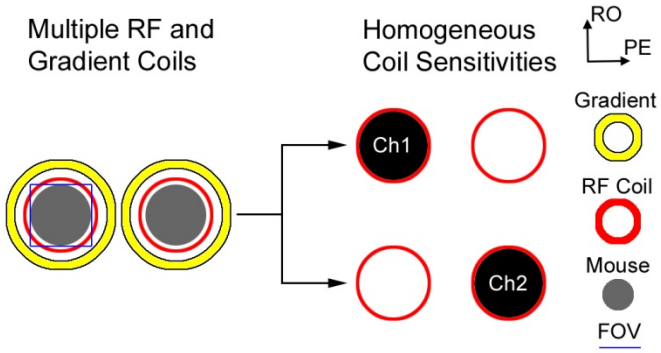

Figure 1-2: Multi-animal MRI with separate gradient coils limits the available packing density and increases cost, but also has many advantages

However, the drawbacks are significant, including increased complexity, increased cost, and reduced packing density compared to single-gradient approaches, meaning that fewer animals can be scanned simultaneously (41). For these reasons, a single-gradient coil approach to multi-animal MRI is often preferred.

A common multi-animal imaging method involves arrays of volume coils that are placed within a single gradient set (41,47). This technique allows the use of the PILS (36) PI technique to reduce the FOV along the phase encode (PE) direction to cover only a single animal, while at the same time, encoding all animals. This theoretically reduces the acquisition time by the number of animals scanned at once. If the volume coils are independent (i.e. perfectly decoupled from one another with individual homogeneous sensitivities as shown in Figure 1-3), images from each animal can be perfectly reconstructed (48,49) without a loss in SNR compared to an equivalent single-animal imaging method.

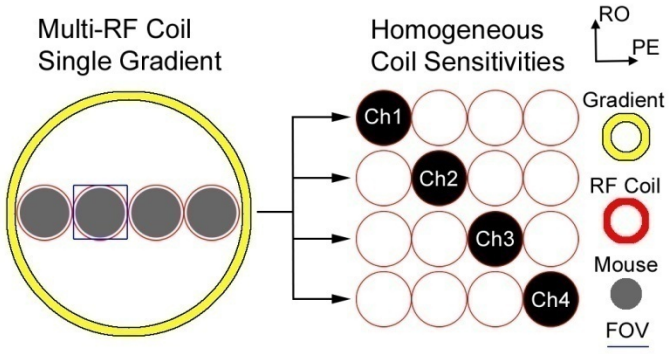

Figure 1-3: Multi-animal MRI with independent volume coils is efficient and cost-effective, but is throughput-limited by the number of mice scanned at once

This imaging strategy has been used to accelerate two functional imaging applications: CMRI (50,51) and DCE-MRI (52). Traditional single-animal CMRI permits the use of prospective gating by synchronizing the acquisition with EKG readings

from the subject. However, since data acquisition schemes cannot be synchronized with non-coincident cardiac cycles from several mice, data must be retrospectively reordered and reconstructed. Bishop and Henkelman demonstrated retrospective gating on three simultaneously-scanned mice by reordering data according to recorded EKG signals measured with wired electrodes on each mouse (50). Esparza et al. incorporated a "wireless" approach (53-55) to simultaneously scan four mice (51) with a previously developed array of four independent volume coils (56).

The array was also used to demonstrate the feasibility of multi-mouse DCE-MRI (52) that achieved a three-fold throughput improvement over conventional imaging methods. For that study, the drawbacks of using a large gradient coil for multi-animal MRI were apparent, including a reduced maximum gradient strength, a reduced slew rate, more acoustic noise, and the potential for rapid gradient heating when fast imaging sequences are used (30,52). For instance, the dynamic acquisition required image update rates to be reduced by a factor of two in order to avoid overheating the gradient coil even after integration of additional heat exchangers into the gradient temperature control system. The affect of decreasing the image update rate on PK parameter estimation was investigated by both quantitatively and qualitatively comparing resulting PK parameter maps derived from single-animal and multi-animal data, along with single-animal datasets that were downsampled to correspond with the multi-animal acquisition parameters. Statistical analyses were performed using a Kruskal-Wallis test and results indicated that no statistically significant difference ($p > 0.05$) in PK parameter estimation was detected.

An alternate approach for multi-animal MRI is to use a single gradient and transmit coil with a distributed surface coil array for reception (57,58). Here, the full

FOV is that which contains the multiple mice being scanned (Figure 1-4), and PI can be used to reduce acquisition time. Because the distributed surface coils are unshielded, PI-accelerated images contain data from multiple animals that may share deleterious imaging artifacts across multiple volumes of interest (VOIs). Therefore, decoupling the coils to improve SNR and PI performance is a priority. Coil decoupling methods are discussed in Section 4.3.3.

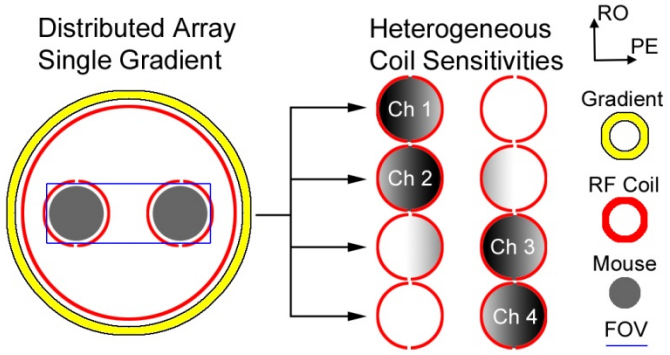

Figure 1-4: Multi-animal MRI with a distributed surface coil array allows the use of multi-animal and parallel imaging accelerations

A final approach also involves a single gradient coil yet dedicates an independent phased array to each of the mice being scanned. Separate shielded transmit coils can be used to restrict the sensitivity of each receive array (Figure 1-5).

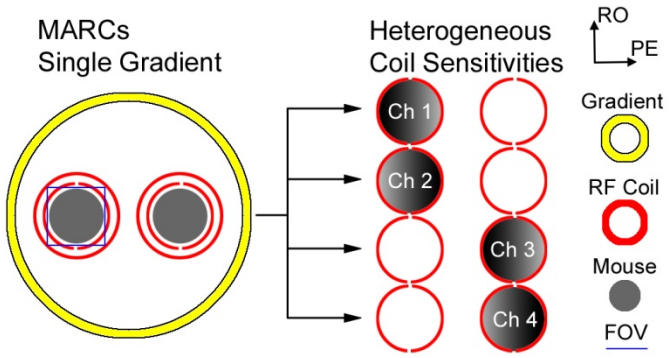

Figure 1-5: Multi-animal MRI with multiple arrays of receive coils (MARCs)

The use of multiple arrays of receive coils (MARCs) permits both multi-animal and PI techniques to be used for improving throughput (59). Since each subarray is independent and specific to a particular animal, traditional single-animal scan parameters can be used to encode all mice being simultaneously scanned and the PI reconstruction can be performed individually by using only coils from the proximal subarray.

1.5 MULTI-MOUSE MRI PARADIGM SHIFT

For multi-animal DCE-MRI studies that require significant time to prepare, anesthetize, stabilize, and insert tail vein catheters into each animal, maximizing throughput requires consideration beyond increasing the number of mice scanned at once. Based on prior studies, a model estimating experiment time as a function of the number of animals simultaneously scanned in a DCE-MRI experiment was generated (52). Results from this model, illustrated in Figure 1-6, indicate that scanning five animals at once is optimal for maximizing throughput improvement, and imaging six or more mice would result in scanner dead time while a set of animals are prepared for the next imaging session. This unnecessarily increases the complexity of simultaneously monitoring and maintaining many animals at once, while not improving study efficiency. This illustrates a paradigm shift from scanning as many animals as can fit in the scanner (60) to scanning a more manageable and optimized number of animals at a faster rate. As such, it is feasible that the use of MARCs will be able to provide more efficient throughput acceleration for functional DCE-MRI studies since the number of mice being scanned at once can be limited to a manageable number, while the number of elements comprising each subarray can be increased to improve PI performance. Tradeoffs between the number of mice scanned at once and the number of array elements sensitive to each mouse will be the focus of Chapter 3.

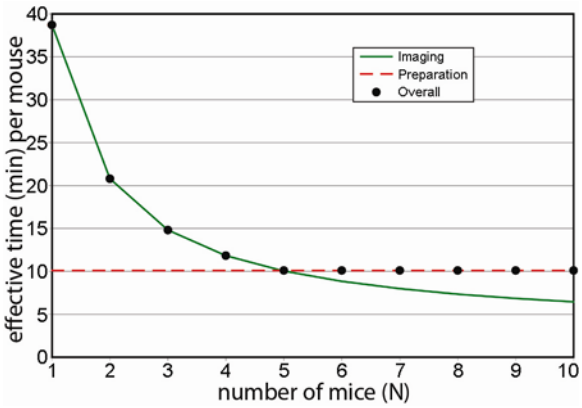

Figure 1-6: Timing estimates from a multi-animal DCE-MRI study. Scanning five animals at once is most efficient.

1.6 Need for State-of-the-Art Multi-Animal MRI System

To date, the majority of small-animal MRI systems have been limited to four or fewer receive channels, however commercial small-animal MRI system electronics can now be configured with up to 16 receive channels. The Small Animal Imaging Facility (SAIF) at The University of Texas M. D. Anderson Cancer Center has recently invested in the development of a digital receiver system that will be capable of simultaneous acquisitions on 16 receive channels. Such a system is imperative to achieve throughput improvements beyond those accomplished to date, which were approximately three-fold for a DCE-MRI study (52). Higher throughput will lower the cost for investigators of novel cancer therapeutics and promote the use of MRI for such investigations. High-throughput DCE-MRI has been successfully used in the SAIF to help speed up dose-optimization studies that would have otherwise not been feasible (61).

1.7 Hypothesis

A throughput-optimized multi-animal array system will enable the most efficient murine DCE-MRI acquisition to date, with a data throughput improvement that is greater

than the number of mice scanned at a time, and without sacrificing image quality compared to a standard single-animal DCE-MRI protocol with conventional imaging hardware.

1.8 RESEARCH PLAN

The purpose of this work is to simulate a variety of multi-animal configurations to determine a throughput-optimized system for accelerating preclinical DCE-MRI studies beyond that afforded by current methods. Tradeoffs associated with various coil designs for realizing the multi-animal imaging system will be discussed and evaluated. Practical consideration of acquisition and reconstruction of accelerated multi-animal DCE-MRI will also be addressed.

An introduction to MR physics, imaging principles, and receive concepts will be presented in Chapter 2. The selection of a throughput-optimized multi-mouse array system will be discussed in Chapter 3, while the hardware design, manufacturing, and testing specifics will be addressed in Chapter 4. The development of a multi-animal imaging protocol on phantoms, and the demonstration of an accelerated multi-animal DCE-MRI protocol on mice will be discussed in Chapter 5. Protocol execution times will be used to estimate the throughput that is achieved compared with traditional single-animal imaging methods using a commercially available volume coil. Finally, an overview of the contributions to advancing preclinical MRI developed in this work and a discussion of the unique challenges to be investigated in future research will be described in Chapter 6.

Chapter 2: Overview of MRI

2.1 MR PHYSICS

The basic physics and imaging principles required to understand a standard MRI experiment will be described in this section. A quantum mechanical description will introduce the fundamentals of MRI after which the classical theory, where the mathematical descriptions are generally more familiar, will be described.

2.1.1 Quantum Mechanical Basis of MRI

Atomic nuclei with an odd number of protons and/or neutrons possess the fundamental property of spin angular momentum or *spin*, denoted as vector $\boldsymbol{S}$, which obeys the same mathematical laws as quantized angular momentum. The magnitude of the spin angular momentum is:

$$S = \frac{h}{2\pi}\sqrt{\mathrm{s(s+1)}}, \qquad (2-1)$$

and the *z*-component is given by:

$$S_z = \frac{h}{2\pi}m_s, \qquad (2-2)$$

where s is the spin quantum number, m_s is the magnetic quantum number, and h is Planck's constant. A magnetic dipole moment $\boldsymbol{\mu}$ (also a vector quantity) is associated with $\boldsymbol{S}$ and is given by:

$$\boldsymbol{\mu} = \gamma \boldsymbol{S}, \qquad (2-3)$$

where the gyromagnetic ratio, γ is an experimentally-determined constant that is unique to the particular nuclear species. Hydrogen atoms have the largest natural abundance in the body (predominantly due to water) and a high NMR sensitivity ($\gamma \,/\, 2\pi = 42.58\, MHz/T$). As a result, hydrogen is the most significant nucleus for MRI.

Hydrogen nuclei, often simply referred to as *spins* or *protons*, are spin one-half particles, where $s = 1/2$ and $m_s = \pm 1/2$.

Since the spin angular momentum is discrete, it makes sense that the interaction of a proton's magnetic moment with an external magnetic field also results in discrete energy levels. Consider a static magnetic field along the z direction with strength B_0 given by:

$$\boldsymbol{B} = 0\hat{\imath} + 0\hat{\jmath} + B_0\hat{k}. \qquad (2-4)$$

The potential energy E of $\boldsymbol{\mu}$ in field $\boldsymbol{B}$ is given by the scalar product:

$$E = -\boldsymbol{\mu} \cdot \boldsymbol{B} = -\mu_z B_0 = -\gamma S_z B_0 = -\gamma \frac{h}{2\pi} m_s B_0, \qquad (2-5)$$

which implies that the energy is lowest when the magnetic moment is aligned along the magnetic field, i.e. is parallel to B_0 with $m_s = +1/2$. The higher energy state will be anti-parallel to B_0 with $m_s = -1/2$. Two populations of nuclei, with probability n_+ for the parallel state and probability n_- for the anti-parallel state, will arise in two energy levels that are separated by the Zeeman energy gap:

$$\Delta E = \gamma \frac{h}{2\pi} B_0. \qquad (2-6)$$

Each proton must occupy one of the two states:

$$n_+ + n_- = 1. \qquad (2-7)$$

With the system in thermal equilibrium, Boltzmann's law describes the ratio of the two populations (62):

$$\frac{n_+}{n_-} = \exp\left(\frac{\Delta E}{kT}\right) = \exp\left(\frac{\gamma h B_0}{2\pi k T}\right), \qquad (2-8)$$

where k is the Boltzmann constant and T is absolute temperature in Kelvin.

If a proton changes from one energy state to the other, it will either emit or absorb a photon of frequency f found from the Bohr relation:

$$\Delta E = hf. \qquad (2-9)$$

Combining Equations $2-6$ and $2-9$, and solving for the angular frequency $\omega = 2\pi f$, gives rise to the Larmor relationship:

$$\omega = \gamma B_0. \qquad (2-10)$$

2.1.2 Bulk Magnetization and the Classical Description of MRI

Classically, the angular momentum $\boldsymbol{J}$ of a charged particle describes a circulating electric current and an associated dipole magnetic moment $\boldsymbol{\mu}$. The relationship between $\boldsymbol{J}$ and $\boldsymbol{\mu}$, as determined from experimental observation, is given by the analogue of Equation $2-3$:

$$\boldsymbol{\mu} = \gamma \boldsymbol{J}. \qquad (2-11)$$

The torque $\boldsymbol{\tau}$ applied to a moment in the presence of an external magnetic field $\boldsymbol{B}$ is given by the classical relationship:

$$\boldsymbol{\tau} = \boldsymbol{\mu} \times \boldsymbol{B}. \qquad (2-12)$$

The torque will cause the angular momentum of this particle to be altered according to (63):

$$\frac{d\boldsymbol{J}}{dt} = \boldsymbol{\tau}. \qquad (2-13)$$

By combining Equations $2-11$, $2-12$, and $2-13$, a general equation of motion for a spin can be derived:

$$\frac{d\boldsymbol{\mu}}{dt} = \boldsymbol{\mu} \times \gamma \boldsymbol{B}. \qquad (2-14)$$

However, MRI is only sensitive to contributions from many spins in a sample volume. It is therefore important to shift the description to the net magnetization $\boldsymbol{M}$, which results from the summation of all $\boldsymbol{\mu}$ in the volume specified by coordinates $\boldsymbol{r}_i$ i.e.:

$$\boldsymbol{M} = \sum_{i=1}^{n_i} \boldsymbol{\mu}(\boldsymbol{r_i}). \qquad (2-15)$$

In the absence of an externally applied magnetic field ($\boldsymbol{B} = 0$), a collection of spins will be randomly oriented by thermal motion (as shown in Figure 2-1). Because there is no spin coherence, the average contribution from all spins will cancel to produce zero net magnetization ($\boldsymbol{M} = 0$).

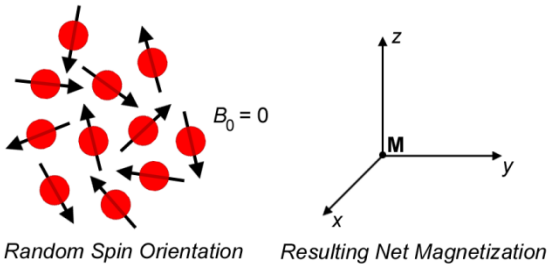

Figure 2-1: Spin orientation and net magnetization without static field B_0. Random spins cancel to produce no net magnetization.

A more interesting result for MRI ensues when spins are placed in a nonzero static magnetic field, as described in Equation $2-4$. For ^{1}H nuclei at room temperature in current MRI field strengths, the difference in state occupancy, described by Equation $2-8$, is only a few parts per million (ppm). This small fractional difference would seem to have a relatively minor effect. However, when considering the abundance of spins in the body, the resulting net magnetization $\boldsymbol{M}$ is significant and will point along B_0 as illustrated in Figure 2-2, since the random contributions along the transverse (x-y) plane will sum to zero and the excess spins in the lower energy state will constructively add

along z. The magnitude of the net magnetization vector due to spin population differences illustrates the logic behind moving to higher magnet field strengths in order to improve the strength of the MR signal.

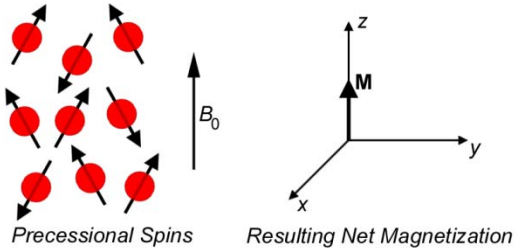

Figure 2-2: Spin orientation and net magnetization with applied B_0. Excess spins in the lower energy state add along the direction of B_0.

By applying the concept of net magnetization $(2-15)$ to the general equation for spin motion $(2-14)$, the fundamental equation of motion in terms of the net magnetization emerges:

$$\frac{d\boldsymbol{M}}{dt} = \boldsymbol{M} \times \gamma \boldsymbol{B}, \qquad (2-16)$$

which is a simplified version of the Bloch equation.

As in the previous section, the effect of the static magnetic field given by Equation $2-4$ is considered. Computing the cross product of Equation $2-16$ results in three differential equations:

$$\frac{dM_x}{dt} = \gamma M_y B_0 \qquad (2-17)$$

$$\frac{dM_y}{dt} = -\gamma M_x B_0 \qquad (2-18)$$

$$\frac{dM_z}{dt} = 0. \qquad (2-19)$$

Combining $2-17$ and $2-18$, gives the following system of differential equations for the transverse components:

$$\frac{d^2}{dt^2}\begin{pmatrix}M_x\\M_y\end{pmatrix}+(\gamma B_0)^2\begin{pmatrix}M_x\\M_y\end{pmatrix}=0. \qquad (2-20)$$

Solving $2-19$ and $2-20$ with the initial condition:

$$\boldsymbol{M}(0)=M_{x0}\hat{\imath}+0\hat{\jmath}+M_{z0}\hat{k}, \qquad (2-21)$$

implying that the magnetization has now gained a transverse component along the *x*-axis, results in (64):

$$\boldsymbol{M}(t)=M_{x0}\cos\omega t\,\hat{\imath}-M_{x0}\sin\omega t\,\hat{\jmath}+M_{z0}\hat{k}. \qquad (2-22)$$

This represents the precession of the net magnetization vector about B_0 at the Larmor frequency

$$\omega=\gamma B_0\,. \qquad (2-23)$$

2.1.3 Return to Equilibrium and the Block Equation

A nonzero transverse component of the net magnetization was introduced in Equation $2-21$. A discussion of how this excitation occurs in practice will be deferred until Section 2.2.1. Equation $2-22$ suggests that the transverse component of the magnetization vector will continually precess about the *z*-axis at the Larmor frequency. This is not a physical result. Rather, the magnetization vector will return to equilibrium according to two relaxation rates. The relaxation mechanism that characterizes the recovery of the longitudinal component of $\boldsymbol{M}$ back to thermal equilibrium along the *z*-axis is known as spin-lattice relaxation. The following differential equation describes this behavior:

$$\frac{dM_z(t)}{dt} = -\frac{M_z(t) - M_{z0}}{T_1}, \qquad (2-24)$$

where M_{z0} is the equilibrium longitudinal magnetization just prior to excitation. The time constant associated with this recovery is given by T_1. Assuming the longitudinal component of the magnetization vector is zero (i.e. the entire magnetization vector resides in the transverse plane), the longitudinal magnetization will return to equilibrium according to the following equation:

$$M_z(t) = M_{z0}\left(1 - e^{-\frac{t}{T_1}}\right). \qquad (2-25)$$

This relaxation mechanism describes the process of dissipating the energy, which was initially gained from the excitation into the transverse plane, through interactions with the surrounding environment, known as the lattice.

The relaxation mechanism that characterizes the decay of $\boldsymbol{M}$ in the transverse plane is known as spin-spin relaxation. This behavior is described by the following differential equation:

$$\frac{dM_{xy}(t)}{dt} = -\frac{M_{xy}(t)}{T_2}. \qquad (2-26)$$

The solution to Equation $2-26$, following an excitation of $\boldsymbol{M}$ completely into the transverse plane, is given by:

$$M_{xy}(t) = M_{z0}e^{-\frac{t}{T_2}}, \qquad (2-27)$$

where the relaxation time constant is T_2. It is the dephasing of the initially in-phase spins that causes T_2 relaxation and the associated loss in signal coherence. This is due to magnetic field interactions between the neighboring spins. T_2 values are unique for different tissue types and are determined by the chemical environment. An additional

relaxation term, T_2* results from the presence of local field inhomogeneities that cause a more rapid dispersion of spin coherence than predicted by T_2 alone. It is important to note that these exponential behaviors are approximate given the phenomenological nature of the relaxation equations.

These relaxation mechanisms can be used to form a more accurate model of the net magnetization motion following an excitation than that given in Equation $2-16$. The complete form of the Bloch equation, taking relaxation into account, is given by:

$$\frac{d\boldsymbol{M}}{dt} = \boldsymbol{M} \times \gamma \boldsymbol{B} - \frac{M_x \hat{\imath} + M_y \hat{\jmath}}{T_2} - \frac{(M_z - M_{z0})\hat{k}}{T_1}. \qquad (2-28)$$

2.2 IMAGING PRINCIPLES

2.2.1 Spin Excitation

An explanation of how the net magnetization is *excited* or *tipped* away from its equilibrium state by application of an RF pulse ($B_1(t)$) that is perpendicular to B_0 will now be presented. To do this, a change of reference from the stationary *laboratory* frame to a frame of reference that is rotating with the same phase and frequency as the precession of $\boldsymbol{M}$, is beneficial. As a result, $\boldsymbol{M}$ will appear stationary in the *rotating* frame:

$$\boldsymbol{M} = M_{x0}\hat{\imath}' + M_{z0}\hat{k}, \qquad (2-29)$$

where from Equation $2-22$, $\hat{\imath}' = \cos\omega t\,\hat{\imath} - \sin\omega t\,\hat{\jmath}$. Similarly, $\hat{\jmath}' = \sin\omega t\,\hat{\imath} + \cos\omega t\,\hat{\jmath}$. Ignoring relaxation effects, Equation $2-16$ can be cast into the rotating frame (63,65):

$$\frac{d\boldsymbol{M}}{dt}_{lab} = \boldsymbol{\Omega} \times \boldsymbol{M} + \frac{d\boldsymbol{M}}{dt}_{rot}, \qquad (2-30)$$

where subscripts *lab* and *rot* represent the laboratory and rotating frames respectively and $\boldsymbol{\Omega} = -\omega\hat{k}$. Combining Equations $2-16$ and $2-30$ and rearranging terms, the time derivative of $\boldsymbol{M}$ in the rotating frame is achieved:

$$\frac{d\boldsymbol{M}}{dt}_{rot} = \frac{d\boldsymbol{M}}{dt}_{lab} - \boldsymbol{\Omega} \times \boldsymbol{M} = \boldsymbol{M} \times \gamma\boldsymbol{B} - \boldsymbol{\Omega} \times \boldsymbol{M} = \boldsymbol{M} \times \gamma\left(\boldsymbol{B} + \frac{\boldsymbol{\Omega}}{\gamma}\right), \quad (2-31)$$

or more compactly:

$$\frac{d\boldsymbol{M}}{dt}_{rot} = \boldsymbol{M} \times \gamma\boldsymbol{B}_{eff}\,, \quad (2-32)$$

with:

$$\boldsymbol{B}_{eff} = \boldsymbol{B} + \frac{\boldsymbol{\Omega}}{\gamma}. \quad (2-33)$$

Consider a radiofrequency excitation field $B_1(t)$ applied along the rotating *x* axis, x':

$$\boldsymbol{B} = \underbrace{B_1(t)}_{RF}\hat{\imath}' + \underbrace{B_0}_{static}\hat{k}\,. \quad (2-34)$$

The effective excitation field in the rotating frame will be:

$$\boldsymbol{B}_{eff} = B_1(t)\hat{\imath}' + \left(B_0 - \frac{\omega}{\gamma}\right)\hat{k}. \quad (2-35)$$

If the excitation is *on-resonance* with the Larmor frequency, the *z*-directed component in Equation $2-35$ will cancel, leaving $\boldsymbol{B}_{eff}$ pointing only along the x' axis. When the excitation frequency is constant, the solution to the governing motion equation becomes (65):

$$\boldsymbol{M}(t) = \boldsymbol{R}_{x'}(\gamma B_1 t)\boldsymbol{M}(0), \quad (2-36)$$

This represents a rotation about x' at a frequency dependent on γ and B_1. $\boldsymbol{R}_{x'}$ is a rotational matrix about $x = x'$ given by:

$$\boldsymbol{R}_x(\alpha) = \begin{pmatrix} \cos\alpha & \sin\alpha & 0 \\ -\sin\alpha & \cos\alpha & 0 \\ 0 & 0 & 1 \end{pmatrix}. \qquad (2-37)$$

In general, the magnetization vector will rotate about the axis of the applied B_1 field. The desired flip angle α depends on the strength and duration of the applied RF pulse. An $\alpha = 90°$ RF pulse completely tips $\boldsymbol{M}$ into the transverse plane.

2.2.2 Magnetic Field Gradients and Selective Excitation

In addition to the main static field B_0 and the time-varying RF field $B_1(t)$, MRI also requires gradient fields $\boldsymbol{G}(t)$ to selectively excite and spatially encode images. Traditional MR imaging requires three orthogonal gradient fields that are linear over the imaging volume, including $G_x = dB_z/dx$, $G_y = dB_z/dy$, and $G_z = dB_z/dz$. The solution to the Bloch equation for a space- (described by $\boldsymbol{r}$) and time-varying gradient field:

$$\boldsymbol{B}(\boldsymbol{r}, t) = (B_0 + \boldsymbol{G}(t) \cdot \boldsymbol{r})\hat{k}, \qquad (2-38)$$

is (65):

$$M_\perp(\boldsymbol{r}, t) = M_\perp(\boldsymbol{r}, 0) e^{\frac{-t}{T_2(\boldsymbol{r})}} e^{-i\omega_0 t} \exp\left(-i\gamma \int_0^t \boldsymbol{G}(\tau) \cdot \boldsymbol{r} d\tau\right), \qquad (2-39)$$

where the complex-valued $M_\perp = M_x + iM_y$ is used because vectors rotating at ω_0 are conveniently described with the phase term $e^{-i\omega_0 t}$ in the laboratory frame.

For 1D spectroscopy, the use of a nonselective hard pulse that excites all spins within the transmit coil sensitivity volume is often sufficient. For MRI however, a particular imaging volume is most often selectively excited. The general approach to selective excitation is to apply a $B_1(t)$ field in the presence of a constant gradient field. For selecting a particular axial slice along the z axis, a constant magnetic field gradient $G_z = dB_z/dz$ can be superimposed with the main field:

$$B_z = (B_0 + G_z z)\hat{k}. \qquad (2-40)$$

The Larmor relationship of $2-23$ indicates that the frequency of spin precession is directly proportional to the magnetic field strength. Therefore, the range of space to be excited i.e. from $z = z_0 - \Delta z/2$ to $z = z_0 + \Delta z/2$ with a slice thickness Δz, corresponds with a frequency range from $\omega = \omega_0 - \Delta\omega/2$ to $\omega = \omega_0 + \Delta\omega/2$. If the time signal $B_1(t)$ has a frequency bandwidth $\Delta\omega = \gamma G_z \Delta z$, the desired slice can be selectively excited. In the low flip angle regime ($\alpha < 30°$), the slice excitation profile is well approximated by the Fourier transform of the $B_1(t)$ field (Figure 2-3). Although the Fourier relationship does not generally hold for larger flip angles, iterative methods involving linearized models have been successfully implemented to design high fidelity large tip angle excitations (66).

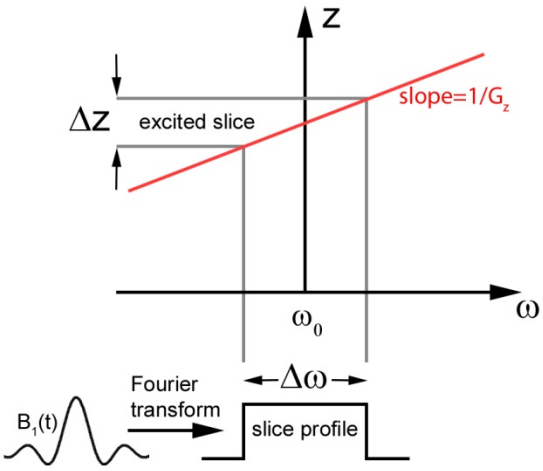

Figure 2-3: Selective slice excitation with gradient field. The Fourier relationship determines the slice profile.

2.2.3 Signal Equation and Fourier Relationship

Ideally, RF coils (which are described in Section 2.3.1) are homogeneously sensitive to the transverse magnetization in the VOI. Although perfect homogeneity is

never possible in practice, we can make this assumption to derive an equation that gives insight into image formation. The received time signal, ignoring constant gain and phase terms, may be approximated as (65):

$$s_r(t) = \int_x \int_y \int_z M_\perp(x,y,z,t)dx\,dy\,dz. \qquad (2-41)$$

Using Equation $2-39$, the received signal is expressed as:

$$s_r(t) = \int_x \int_y \int_z M_\perp(\boldsymbol{r},0)\, e^{\frac{-t}{T_2(\boldsymbol{r})}} e^{-i\omega_0 t} \exp\left(-i\gamma \int_0^t \boldsymbol{G}(\tau)\cdot \boldsymbol{r} d\tau\right) d\boldsymbol{r}. \quad (2-42)$$

This work focuses on 2D imaging only, so this example will be restricted to the 2D function over an axial slice $m(x,y)$ of thickness Δz at some position z_0. Assuming an ideal slice selection with a rectangular profile, $m(x,y)$ is given by:

$$m(x,y) = \int_{z_0-\Delta z/2}^{z_0+\Delta z/2} M_\perp(x,y,z,0)dz. \qquad (2-43)$$

Ignoring the spin-spin relaxation term and the frequency modulation term produces the baseband signal:

$$s(t) = \int_x \int_y m(x,y) exp\left(-i\gamma \int_0^t \boldsymbol{G}(\tau)\cdot \boldsymbol{r}\, d\tau\right) dx\,dy. \qquad (2-44)$$

For this 2D imaging example, only *x* and *y* gradient fields must be considered. This further simplifies Equation $2-44$ to the *signal equation*:

$$s(t) = \int_x \int_y m(x,y) e^{-2\pi i\left[k_x(t)x + k_y(t)y\right]} dx\,dy, \qquad (2-45)$$

where

$$k_x(t) = \frac{\gamma}{2\pi} \int_0^t G_x(\tau)\, d\tau \qquad (2-46)$$

and

$$k_y(t) = \frac{\gamma}{2\pi}\int_0^t G_y(\tau)\, d\tau. \qquad (2-47)$$

The signal equation is the 2D Fourier transform of $m(x,y)$:

$$s(t) = \mathcal{F}_{2D}\{m(x,y)\} = \mathcal{M}\big(k_x(t), k_y(t)\big). \qquad (2-48)$$

Assuming an ideal single-shot acquisition, this result indicates that the signal at any time *t* is the value of the 2D Fourier transform of $m(x,y)$ at a particular spatial frequency in Fourier space or *k*-space. In practice, most sequence acquisitions collect the set of signals $\{s(t)\}$ that cover all desired spatial frequencies of $m(x,y)$, in a raster-style sampling pattern through separate excitations and receptions. This process, known as phase-encoding, is described in Section 2.2.4.

2.2.4 Frequency and Phase Encoding

To simplify the investigation of typical MRI acquisition strategies, imaging can first be restricted to one dimension. To do this, the *y*-gradient of Equation $2-47$ can be turned off (i.e. $G_y = 0$), resulting in the following signal equation:

$$s(t) = \mathcal{F}_{1D,x}\{m(x,y)\} = \mathcal{M}(k_x(t),0)\,. \qquad (2-49)$$

By the projection slice theorem (67), this implies that the acquired time signal will be the 1D Fourier transform of a projection of the 2D object $m(x,y)$ onto the *x*-axis. In other words, the linear gradient G_x frequency-encodes the spin density $m(x,y)$ about its position along *x*. The direction of frequency encoding is often described as the readout (RO) direction. Applying an inverse Fourier transform to $s(t)$ will recover the projection of $m(x,y)$.

Most often, it is desirable to recover $m(x,y)$ rather than simply a 1D projection of $m(x,y)$. To do this, spatial information about the spin density $m(x,y)$ along the *y*-

dimension must be gained. This can be accomplished by repeating the acquisition RO with different, but consistently-incremented initial phase distributions, which can be achieved by varying the intensity of the phase-encoding (PE) gradient G_y. Phase encoding ultimately results in a similar encoding of the spin density $m(x, y)$ along the *y*-direction as frequency encoding has along the *x*-direction. Once all of *k*-space is acquired, $m(x, y)$ can be recovered by a 2D Inverse Fourier Transform as illustrated in Figure 2-4.

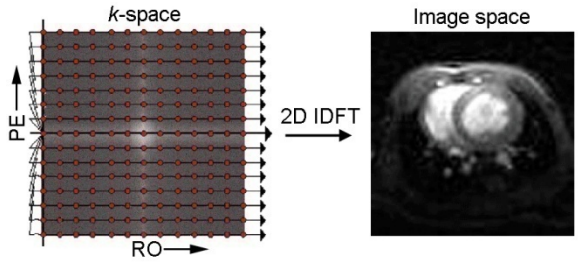

Figure 2-4: Cartesian sampling pattern in *k*-space and image reconstruction by an inverse Fourier Transform.

Sequentially incrementing the initial phase within the subject requires significantly more time than does frequency encoding. As such, methods to reduce the number of time-consuming PE steps will be discussed in Section 2.2.8.

2.2.5 Gradient and Spin Echo Imaging

Acquiring phase-coherent signals in the form of gradient echoes and spin echoes will now be described. The following description is for general 2D axial imaging, with slice-select along *z*, frequency-encoding along *x*, phase-encoding along *y*, and Cartesian sampling.

2.2.5.1 Gradient Echo Imaging

A diagram of the gradient echo pulse sequence is shown in Figure 2-5. To achieve selective excitation, as discussed in Section 2.2.2, a constant positive gradient G_z is applied during the RF pulse. Unfortunately, the applied gradient introduces field inhomogeneities (as a function of position) and as a result, the excited spins begin to dephase or lose coherence across the slice thickness. To instead begin imaging with excited spins that are coherent throughout the slice, a negative rephasing gradient is applied just after the positive gradient to cancel the spin dephasing that has accumulated since the center of the RF excitation pulse (63).

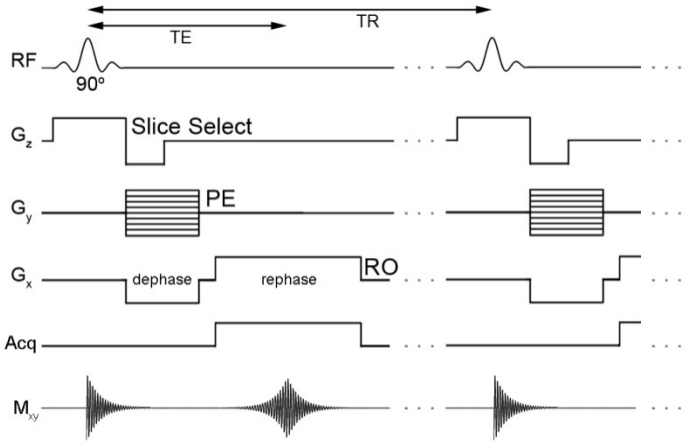

Figure 2-5: Gradient echo pulse sequence. The resulting echo is produced at TE during which the signal is acquired.

As described in 2.2.4, phase encoding is accomplished by varying the strength of the G_y gradient during every sequential repetition time (TR) interval (Figure 2-5). For optimized pulse sequence timing, the dephasing lobe of the RO gradient G_x can be initiated during the PE gradient. As was the case for the slice select gradient, the negative RO dephasing gradient will introduce spin incoherence in the form of phase

shifts. After the direction of the RO gradient is switched, the spin coherence will be partially restored (minus T_2* relaxation effects) when the accumulated RO dephasing gradient is cancelled. A gradient echo (GRE), whose amplitude will be maximum at the echo time (TE), is formed and digitized during the acquisition window. GRE sequences are often used to acquire T_1-weighed or T_2*-weighted images.

2.2.5.2 Spin Echo Imaging

The formation of a spin echo (SE) is often described by a track race analogy. Consider a race of athletes: 1, 2, and 3, each running at the same constant velocity. At any point in time, the runners, like coherent spins precessing at a single frequency ω, are in-phase. However, imagine the case where the runners/spins simultaneously start the race at time zero (Figure 2-6 A) and are all advancing along the track at different, but constant velocities (Figure 2-6 B).

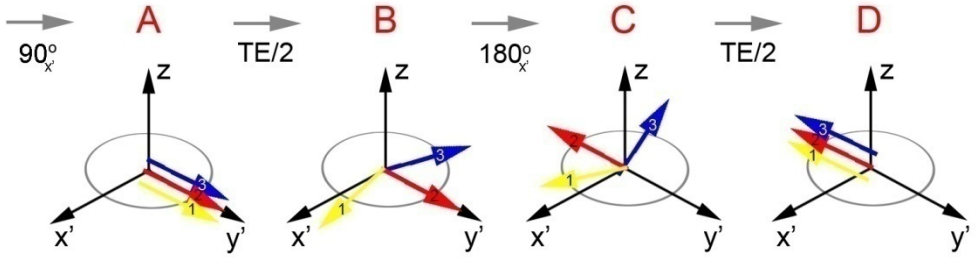

Figure 2-6: Spin echo formation in rotating frame is dependent on the phase coherence of excited spins

The different velocities represent variations in magnetic field strength that spins located at different positions experience. In the rotating frame, this can be illustrated as runner/spin 2 *on resonance* with the average group velocity, runner/spin 1 leading the group, and runner/spin 3 lagging the group. If halfway through the race (at time TE/2) the starting line is changed to the finish line, the runners will immediately switch their

direction (Figure 2-6 B to C). Runner/spin 3 would lead the group and runner/spin 1 would lag the group. By the time the runners arrive to the finish line (at TE), they would all be in-phase (Figure 2-6 D) as they were at time zero.

Spin echoes follow the same logic. Field inhomogeneities dephase spins until a 180° pulse is applied at TE/2, instantaneously reversing the direction of the spins. After another time TE/2 passes, the spins will again be in-phase. A benefit compared to gradient echoes, is that spin echoes will not be influenced by local magnetic field inhomogeneities, and spin echoes restore transverse signal decay to the T_2 relaxation rate of the subject.

A diagram of the SE pulse sequences is shown in Figure 2-7. Slice-select and PE gradient waveforms are identical to those describing GRE. Here, the RO gradient, however, takes a slightly different form. Note that the initial dephasing lobe is actually positive in Figure 2-7. The nonselective 180° *hard pulse* inverts the spins to where the combination (of positive dephase and 180° pulse) acts like a negative dephasing gradient. The positive RO gradient is then applied and the spin echo, formed at time TE, is acquired. Incrementing G_y for every repetition results in full *k*-space coverage.

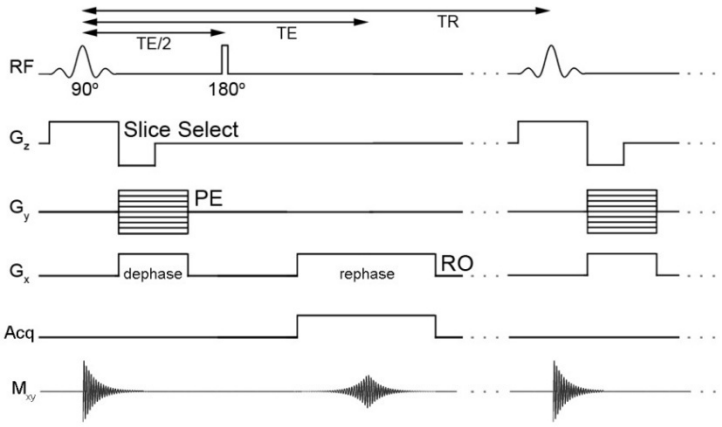

Figure 2-7: Spin echo pulse sequence requires a nonselective 180° pulse

2.2.5.3 k-Space Perspective

Conceptualizing encoding and echo formation in the image domain is typically more difficult than in *k*-space. From the *k*-space perspective, the integral of G_y and $G_x$with respect to any point in time indicates the location of the sampled data in *k*-space. For instance, if a constant PE gradient is on for a duration d_{PE}, the *k*-space spatial frequency associated with the *y* direction is (63):

$$k_y(G_y) = \frac{\gamma}{2\pi} G_y d_{PE}. \qquad (2-50)$$

Prior to the acquisition of a line in *k*-space, k_y and the initial value of k_x should be established. From the gradient echo diagram of Figure 2-5, if G_y is first initiated as the most negative gradient and duration d_{PE}:

$$k_{y_{min}} = -G_{y_{max}} \frac{\gamma}{2\pi} d_{PE}, \qquad (2-51)$$

and since the dephasing lobe of G_x will also be of the same direction, amplitude, and duration:

$$k_{x_{min}} = -G_{x_{max}} \frac{\gamma}{2\pi} d_{PE}, \qquad (2-52)$$

the acquisition will commence in the lower left-most portion of *k*-space ($k_{x_{min}}, k_{y_{min}}$). When the rephasing RO gradient is then *played out*, the *k*-space line corresponding to $k_y = k_{y_{min}}$ will be traversed along the $+k_x$ direction. The maximum amplitude of each echo corresponds with sampling at $k_x = 0$ and the maximum overall amplitude will occur at the center of *k*-space i.e. corresponding with zero frequency or DC. During each repetition, the amplitude and direction of G_y will be incrementally changed to vary the acquisition starting point ($k_{x_{min}}, k_y$). This will ultimately result in full Cartesian sampling of *k*-space as shown in Figure 2-4. For spin echoes, application of the 180° pulse will move the *k*-space position k_x and k_y to $-k_x$ and $-k_y$ respectively.

2.2.6 Image Contrast

MRI is a unique imaging modality in that the tissue contrast of images can be readily changed by modifying the sequence structure and pulse sequence parameters, such as TE and TR. The most common anatomic imaging sequences exploit differences in tissue relaxation rates to produce excellent soft-tissue contrast. Spin-density or proton-density weighting, as the name implies, gives a contrast based on the number of protons in a given location and is achieved with a long TR and short TE, where T_1 and T_2 relaxation effects are minimal. This weighting results in the maximum signal, but is rarely used because of long acquisition time and the lack of contrast between tissue types. If TR is reduced, to the point that longitudinal magnetization will not fully recover, the image contrast will be weighted by differences in spin-lattice relaxation rates. The combination of a short TE and short TR therefore results in T_1-weighted images. On the other hand, if TE is increased compared to T_1-weighted acquisition parameters, transverse magnetization will have more time to evolve and will reflect differences in spin-spin relaxation rates. T_2-weighted images can be formed with a combination of a long TE and a long TR.

2.2.7 Field of View and Aliasing

Sampling of *k*-space entails converting the continuous spatial frequency domain into a set of discrete samples. Mathematically, the sampled version of *k*-space $\mathcal{M}_s(k_x, k_y)$ can be represented as a product between the continuous time domain signal $\mathcal{M}(k_x, k_y)$ and a 2D comb function III, which consists of delta functions spaced at regular intervals Δk_x and Δk_y:

$$\mathcal{M}_s(k_x, k_y) = \mathcal{M}(k_x, k_y) \frac{1}{\Delta k_x \Delta k_y} III\left(\frac{k_x}{\Delta k_x}, \frac{k_y}{\Delta k_y}\right). \qquad (2-53)$$

The Fourier transform of this comb function is another comb function with delta functions spaced at intervals $1/\Delta k_x$ and $1/\Delta k_y$:

$$\mathcal{F}_{2D}\left\{\frac{1}{\Delta k_x \Delta k_y} III\left(\frac{k_x}{\Delta k_x}, \frac{k_y}{\Delta k_y}\right)\right\} = III\big(\Delta k_x x, \Delta k_y y\big). \qquad (2-54)$$

Multiplication in *k*-space corresponds to convolution in image space. The discretized image is given by:

$$m_s(x,y) = m(x,y) ** III\big(\Delta k_x x, \Delta k_y y\big), \qquad (2-55)$$

where ** represents a 2D convolution. Discrete sampling in *k*-space results in replicates of $m(x,y)$ that are positioned at intervals of $FOV_x = 1/\Delta k_x$ and $FOV_y = 1/\Delta k_y$. If an adequate sampling rate is not achieved, signals from outside the FOV may be incorrectly mapped onto the image of the object (of width W and height H) within the FOV. This phenomenon, known as aliasing, is typically avoided by Nyquist sampling with:

$$sampling\ frequency_{k_x} = \frac{1}{\Delta k_x} > W \qquad (2-56)$$

and

$$sampling\ frequency_{k_y} = \frac{1}{\Delta k_y} > H. \qquad (2-57)$$

It is important to note that anti-aliasing low pass filters can be applied along RO but not along the PE direction.

2.2.8 Parallel Imaging

Parallel imaging utilizes the inherent encoding offered by the distinct coil locations to reduce data acquisition time. As Equations $2-56$ and $2-57$ suggest, Cartesian sampling at the Nyquist rate results in *k*-space lines that are spaced Δk_y apart. However, if sampling is reduced by R times along the PE direction (still assumed to be along the y direction), lines in *k*-space will instead be spaced $R \times \Delta k_y$ distance apart.

Thus, the imaging FOV becomes too small to contain the object and image aliasing (or fold over) occurs. As an example, Cartesian undersampling by $R = 2$ is illustrated in Figure 2-8. Because phase encoding takes approximately the number of PE points times the repetition time (i.e. $N_{PE} \times TR$), while sampling along RO takes on the order of milliseconds, PI aims to reduce the number of PE steps required to accurately reconstruct an image. Many different PI acquisition strategies, which vary in their effectiveness and acquisition requirements, have been developed. These strategies are typically separated into two categories based on if they are reconstructed in image space (36,39) or *k*-space (35,38).

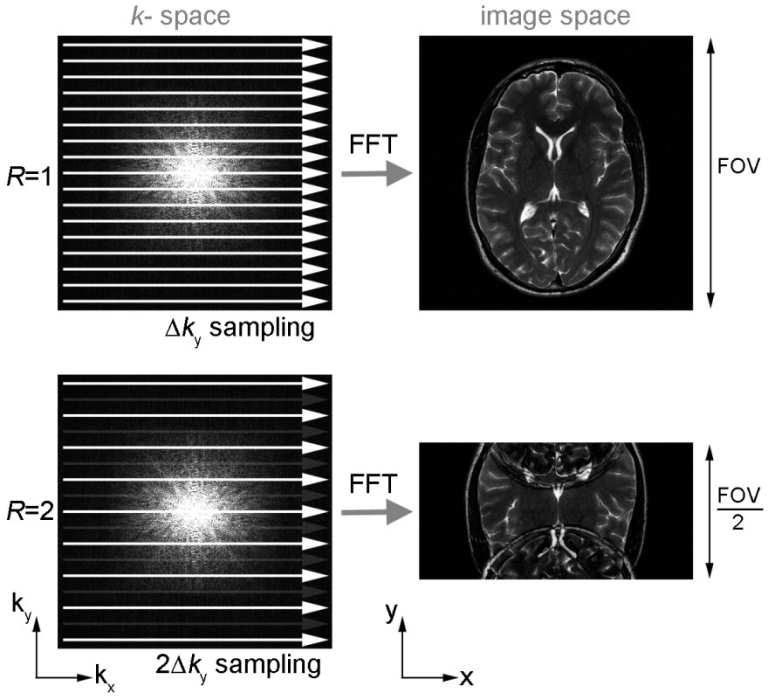

Figure 2-8: Image undersampling by $R = 2$ (shown on left) results in image fold-over or aliasing (right)

2.2.8.1 PILS

Partially parallel imaging with localized sensitivities, or PILS, is an image-domain reconstruction method that relies on independent coil locations which cover distinct regions of the total VOI (36). The coils must be placed along the PE direction and the reduced imaging FOV must be extended further than the sensitive region of a single coil. If each coil is precisely independent, the resulting reconstructed image will have no loss in resolution and will only suffer a SNR loss equal to the square root of the PI reduction factor *R* (36):

$$SNR_{PI} = \frac{SNR_{full}}{\sqrt{R}}. \qquad (2-58)$$

This is because SNR is proportional to the square root of the acquisition time or number of observations, and *R* times fewer PE lines will be acquired (65). The basic PILS strategy is illustrated in Figure 2-9. The full FOV can be reduced along the PE direction if the coil locations (1 through 8 here) are sufficiently varied over the object along the PE direction. Individual coil images can be formed and combined via a method such as a sum of squares (SOS) image combination.

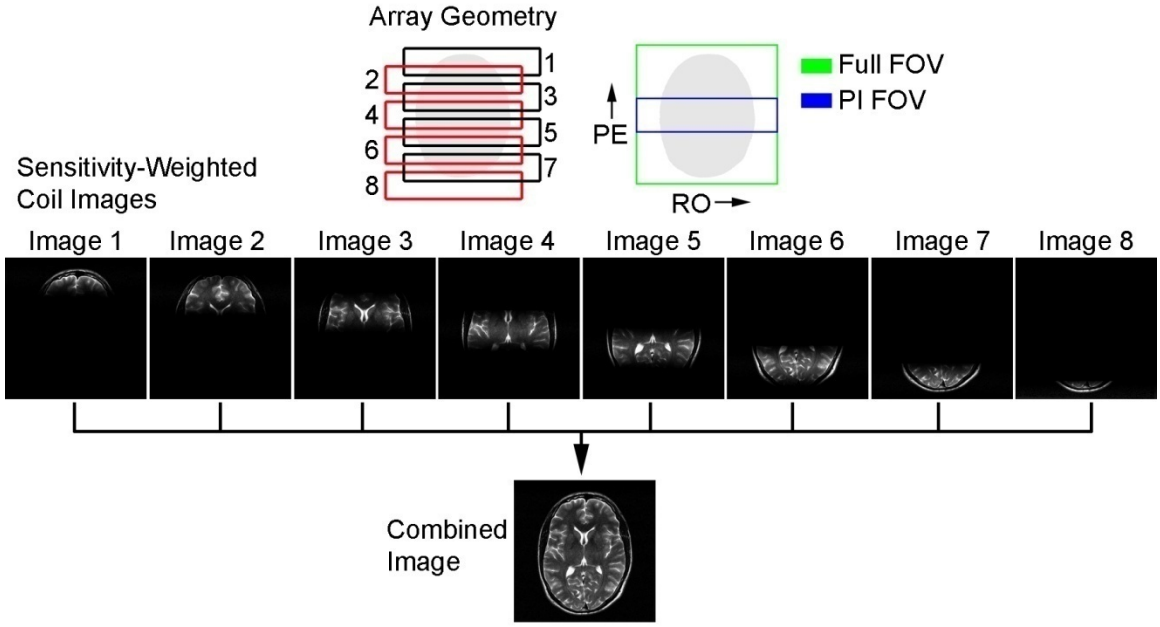

Figure 2-9: PILS parallel imaging strategy. A FOV larger than the coil sensitivity permits image reconstruction.

2.2.8.2 SENSE

Sensitivity encoding (SENSE) (39) is the most well known image-domain PI method (34). In the most basic terms, SENSE can be described as an image unfolding algorithm. More specifically, applying the reduction factor R will result in N_c coil images with $FOV = FOV_{full}/R$. Thus, each pixel in the folded coil images will correspond with R pixels in the FOV_{full} reconstructed image. However, the image pixels will also be weighted by the inhomogeneous sensitivity C of each coil as it relates to the FOV_{full}. Thus, the image signal at a particular folded pixel location $I_k(x, y)$ can be mathematically written as:

$$I_k = \sum_{r=1}^{R} C_{k,r}\rho_r, \qquad (2-59)$$

where k indexes the coils from 1 to N_c, r indexes the R pixels in the FOV_{full} image, and ρ corresponds with the pixel values of the FOV_{full} image. For all N_c coils, the matrix notation becomes:

$$\boldsymbol{I} = \boldsymbol{C\rho}. \qquad (2-60)$$

Including noise correlation between receive coils/channels, the desired unfolded pixel values can be determined from the pseudoinverse of the sensitivity matrix $\boldsymbol{C}$. This can be written as (34):

$$\boldsymbol{\rho} = (\boldsymbol{C}^H\boldsymbol{\Psi}^{-1}\boldsymbol{C})^{-1}\boldsymbol{C}^H\boldsymbol{\Psi}^{-1}\boldsymbol{I}, \qquad (2-61)$$

where $\boldsymbol{\Psi}$ is the noise covariance matrix of the array and superscript ^{H} represents the complex conjugate transpose. Accurate estimation of $\boldsymbol{C}$ must be determined, often through a separate prescan (39). Solving Equation $2-58$ is possible as long as the sensitivity matrix is well conditioned. This places a theoretical restriction on R to be less than the number of coils in the array, N_c. Unlike PILS, SENSE allows image reconstruction with an arbitrary coil configuration; however, there is an additional SNR penalty given by the geometry factor or g-factor. The g-factor is a sequence- and array geometry-dependent map which relates the SNR due to PI with respect to the SNR from the fully-encoded image (39):

$$SNR_{PI} = \frac{SNR_{full}}{g\sqrt{R}}. \qquad (2-62)$$

This is the general equation for SNR resulting from PI. The g-factor has a minimum value of one.

2.2.8.3 SMASH

Simultaneous acquisition of spatial harmonics (SMASH) is similar to SENSE in that it requires prior estimation of the array coil sensitivities. SMASH uses linear combinations of the estimated sensitivities to directly generate missing phase-encode lines (38) in *k*-space. Unfortunately, SMASH is highly restricted by the particular coil placement to provide accurate image reconstruction (34) and thus offers only limited applicability to the multi-animal imaging methods of this work.

2.2.8.4 GRAPPA

The generalized autocalibrating partially parallel acquisitions (GRAPPA) technique is an evolution of SMASH that estimates missing *k*-space lines through a combination of a training phase and a writing phase. To do this, a few autocalibrating signal (ACS) lines in addition to the *R*-fold subsampled *k*-space lines are acquired through each of the N_c coils (Figure 2-10 left).

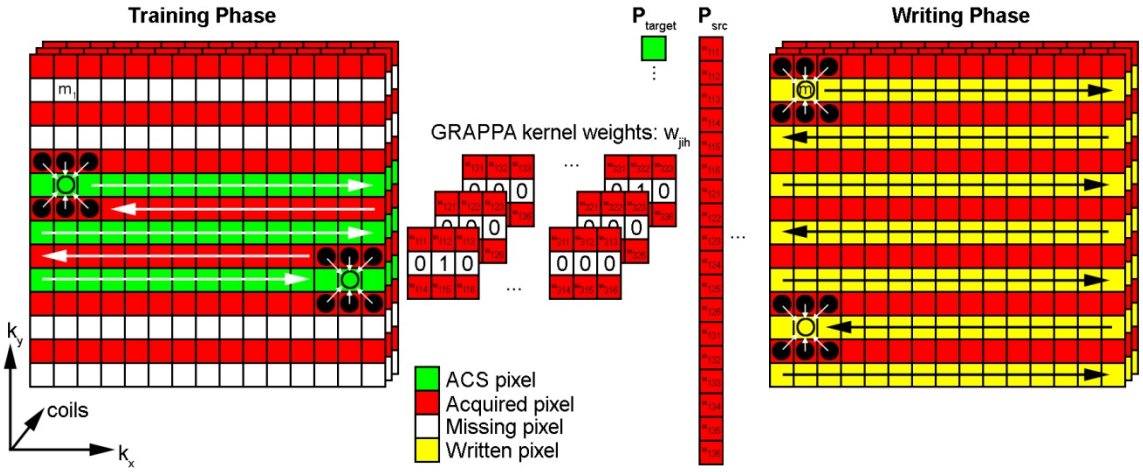

Figure 2-10: Training and writing phases of the GRAPPA reconstruction. GRAPPA weights are determined during the training phase and are used to estimate missing data during the writing phase.

For the training phase, the number of points in the GRAPPA convolution kernel $N_{2D\ kernel}$ and the number of target points per kernel N_{target} are initially selected. The kernel is then slid through N_{rep} positions of the training data (i.e. the central portion of *k*-space where the ACS lines reside), at which time the target and corresponding source points are assembled into matrices $\boldsymbol{P}_{target}$and $\boldsymbol{P}_{src}$ of size $N_{target}N_c \times N_{rep}$ and $N_{2D\ kernel}N_c \times N_{rep}$ respectively. The kernel weights in matrix $\boldsymbol{w}$ of size $N_{target}N_c \times N_{2D\ kernel}Nc$, are related to the assembled matrices by:

$$\boldsymbol{P}_{target} = \boldsymbol{w}\boldsymbol{P}_{src}, \tag{2-63}$$

and can be solved for with a pseudoinverse (68):

$$\boldsymbol{w} = \boldsymbol{P}_{target}{\boldsymbol{P}_{src}}^{-1}. \tag{2-64}$$

During the writing phase, the missing *k*-space data can be estimated via convolution to form the accelerated *k*-space of each coil *j*:

$$\boldsymbol{k}_j^{acc} = \sum_{i=1}^{N_c} \boldsymbol{k}_i^{subsampled} ** \boldsymbol{w}_{j,i}, \tag{2-65}$$

where $\boldsymbol{k}_i^{subsampled}$ represents the subsampled *k*-space matrix from the i^{th} coil (Figure 2-10 left) and $\boldsymbol{w}_{j,i}$ represents the GRAPPA kernel coefficients from the i^{th} coil used to estimate the j^{th} coil *k*-space $\boldsymbol{k}_j^{acc}$. Fourier transformations of each $\boldsymbol{k}_j^{acc}$ yield the coil images which can be combined into a final image.

To help illustrate what the convolution is doing, consider the example in Figure 2-10, where $N_c = 3$, $N_{2D\ kernel} = 6$, $N_{target} = 1$, and $N_{rep} = 65$. The value of a single missing pixel m_j from $\boldsymbol{k}_j^{acc}$, is calculated by:

$$m_j = \sum_{i=1}^{N_c} \sum_{h=1}^{N_{2D\,kernel}} w_{j,i,h} \cdot data_{i,h}, \qquad (2-66)$$

where h indexes the 2D kernel points, i indexes the coils, and $data$ represents known acquired pixels. Due to the robustness of the reconstruction, GRAPPA has been chosen as the PI reconstruction method of choice for many commercial MRI systems, including the Bruker system used for this work.

2.3 Signal Reception

A brief overview of concepts and hardware for signal reception will be given in this section.

2.3.1 Signal Induction and RF Coils

Once the net magnetization has been perturbed to have a transverse component, the precession of $\boldsymbol{M}$ about the static field can be detected with a loop antennae, or RF coil. When the spins' magnetic flux Φ_B cuts through the RF coil loop, an electromotive force ϵ will be generated across the coil:

$$\epsilon = -\frac{\partial \Phi_B}{\partial t}, \qquad (2-67)$$

a consequence of Faraday's law of induction. The flux is proportional to the number of field lines that penetrate the effective area making up the coil loop:

$$\Phi_B = \int_{coil\,area} \boldsymbol{B} \cdot d\boldsymbol{S}, \qquad (2-68)$$

where $d\boldsymbol{S}$ is the infinitesimal surface vector that is normal to the surface plane. By the principle of reciprocity, the flux detected by a coil can be found by instead calculating the fields produced by the coil (63). The rapid oscillations of the transverse magnetization at the Larmor frequency (i.e. the free induction decay or FID) induce the dominant signal in

the receive coil (63). Thus, RF coils must be placed along the transverse direction for optimal signal detection.

A simple surface coil model is shown in Figure 2-11. The inductance of the coil L_c is determined by the physical geometry of the loop conductor. The total resistance R is a combination of the coil resistance R_c and the sample resistance R_s caused by losses due to thermal motion in the subject.

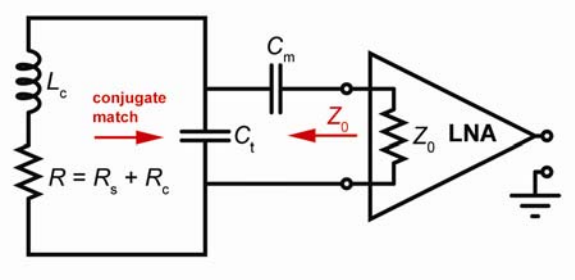

Figure 2-11: Basic model of surface coil. A conjugate match from the coil perspective and a noise match from the preamplifier can be simultaneously achieved.

The tuning capacitor C_t is critical for manipulating the coil resonance to be near the Larmor frequency ω_0. If the coil is isolated from matching circuitry, the resonance frequency is approximately:

$$\omega_0 = \frac{1}{\sqrt{L_c C_t}}. \qquad (2-69)$$

For optimal performance, the RF coil must be matched to a receiver system. The combination of C_t and matching capacitance C_m transforms the coil impedance $Z_c = R + j\omega L_c$ to the characteristic impedance of the transmission line Z_0 and input impedance of the preamplifier. This maximizes power transferred from the coil and provided the output resistance required to minimize the noise figure of the second stage of the cascade, the preamplifier. For most RF instrumentation Z_0 = 50 Ω. Historically, this value has

been selected as a compromise between that which gives the maximum power-handling capability (Z_0 = 30 Ω) and minimal loss (Z_0 = 77 Ω) for an air dielectric transmission line (69). To match the coil to 50 Ω at the Larmor frequency, the following two conditions must be met:

$$Real\left\{(R + j\omega_0 L_c) \parallel \left(\frac{-j}{\omega_0 C_t}\right) - \frac{j}{\omega_0 C_m}\right\} = 50 \qquad (2-70)$$

$$Imag\left\{(R + j\omega_0 L_c) \parallel \left(\frac{-j}{\omega_0 C_t}\right) - \frac{j}{\omega_0 C_m}\right\} = 0. \qquad (2-71)$$

This results in a conjugate match of impedance Z_c (as shown in Figure 2-12) at the Larmor frequency. The implications of tuning and matching with relation to noise are addressed in Section 2.3.3.

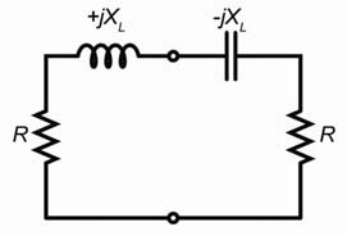

Figure 2-12: Conjugate match condition of the coil

The optimization of the RF coil is an effective means to improve image SNR, independent of increasing the field strength or optimizing pulse sequences. To minimize losses, surface coils can be made just larger than the target VOI, eliminating coupling to unnecessary portions of the lossy subject volume. This results in improved local SNR, with the drawback of a smaller, heterogeneous sensitivity. Although the heterogeneous sensitivities of receive coils can be corrected, this is not the case for transmission.

To achieve a homogenous excitation, a complex structure of coil conductors can produce a sensitivity that is homogeneous over a large imaging volume. Although such

volume coils can generally be useful for both transmission and reception, losses from electric coupling to the entire sample volume increase sample noise and ultimately degrade image SNR. Therefore, volume coils are most commonly used for homogeneous excitation only with a separate surface coil dedicated for reception.

2.3.2 Coil Arrays

To achieve a large VOI associated with a volume coil, while maintaining the SNR advantages associated with surface coils, a coil array can be used (40). Coil arrays consist of multiple surface coils that each posses a unique sensitivity to the sample volume. By increasing the number of coils, the intrinsic SNR can be increased, thus reducing the need for signal averaging to achieve the desired image quality (40).

Arrays have become ubiquitous for clinical MRI and are becoming more popular for small-animal MRI as system manufacturers offer multi-channel receivers as an upgrade option. Until Roemer introduced the NMR phased array in 1991 (40), MRI systems had primarily used a single channel for signal reception. At the time, the cost of receive channels was prohibitively expensive, and methods to acquire multicoil data without parallel receivers, such as time-domain multiplexing, were investigated (70). Today, the cost of multichannel receivers is no longer as much of an obstacle and MRI system manufacturers are offering an ever increasing number of channels for end users. This allows coil arrays to be used for improved SNR and the flexibility to use PI for increased acquisition speed.

For human MRI, where noise is often dominated by body losses, coil arrays with many elements (> 32) have been used to achieve enhanced SNR in peripheral regions of the body (71-73). However, recent results have claimed only marginal improvements in SNR (72,74) (and in some cases worse SNR (72)) with 128-element arrays compared

with 32-element arrays. It remains to be seen if improvements in PI performance (71,72,74) will continue to drive development of large arrays for routine clinical practice.

Although volume coils are still the most utilized RF coil for small-animal MRI, SNR limitations and the desire to accelerate imaging have led to development of small-animal arrays for single-animal imaging (75-78). So far, these arrays have primarily consisted of eight or fewer elements, but have achieved better SNR than volume coils of an equivalent size (79). For many applications, this increased SNR provides additional flexibility including the possibility of faster image acquisition time with the PI techniques discussed in 2.2.8 (34).

The effect of using multiple coils in close proximity for imaging can be described with the illustrative aid of Figure 2-13. From Equation $2-67$, the emf introduced in a primary coil (left side of Figure 2-13) is given by:

$$\epsilon_1 = -\frac{\partial \Phi_B}{\partial t}. \qquad (2-72)$$

This emf and the finite coil resistance R_c will set up a current in the primary loop according to Ohm's law:

$$i_1 = \frac{\epsilon_1}{R_c}. \qquad (2-73)$$

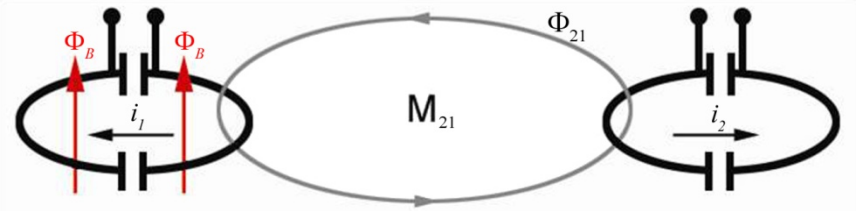

Figure 2-13: Mutual inductive coupling between two nearby coils is caused by a current-induced magnetic flux that penetrates a secondary coil.

The current flowing around the primary coil i_1 will generate its own magnetic flux Φ_{21} that can penetrate a secondary coil according to the relationship:

$$\Phi_{21} = M_{21} i_1, \qquad (2-74)$$

where M_{21} is the mutual inductance. Using Equation $2-67$ and the relationship of $2-74$, the generation of an emf in the secondary coil (ϵ_2) due to the signal in the first coil is evident:

$$\epsilon_2 = -\frac{\partial \Phi_{21}}{\partial t} = -M_{21}\frac{\partial i_1}{\partial t}. \qquad (2-75)$$

A method to reduce M_{21}, known as coil decoupling, is critical to maximize SNR and maintain low g-factors for parallel imaging. Decoupling strategies are discussed in Section 4.3.3.

2.3.3 Noise Considerations

To gain insight on the effect of receive components on noise performance, consider the receive chain in Figure 2-14 that consists of cascaded stages, each with a particular gain (G) and noise performance or noise figure (F).

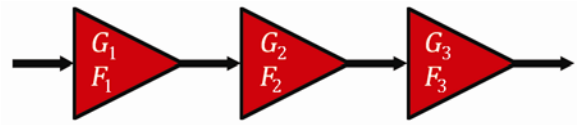

Figure 2-14: Cascade of amplifiers for noise analysis

For a general two-port network, noise figure is defined as the ratio of the output noise power to the portion due to the thermal noise in the input at a standard noise level (69), and it is expressed in dB. This allows one to consider only the input/output noise behavior of a system without keeping track of all internal noise sources. The total noise figure of a cascaded system is given by:

$$F_{total} = F_1 + \frac{F_2 - 1}{G_1} + \frac{F_3 - 1}{G_1 G_2} + \cdots \qquad (2-76)$$

Here, the RF coil is considered the first stage of the cascade to gain insight on how the coil and associated matching circuitry affect SNR. Consider a circuit model with the addition of a generic source voltage v_g as shown in Figure 2-15.

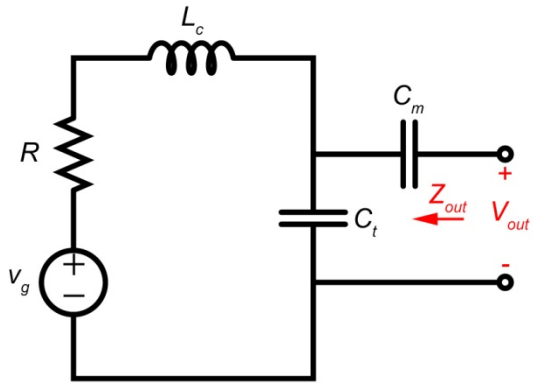

Figure 2-15: Surface coil model with tuning and matching network and a generic voltage source

The available power gain G_a is defined as the power available at the output of a system divided by the power available from the input (69). The power available at the output of the tuning and matching network is given by:

$$P_{out} = \frac{{V_{out}}^2}{Re\{Z_{out}\}}, \qquad (2-77)$$

where V_{out} and Z_{out} are defined according to Figure 2-15. The available power from the input (shown in Figure 2-16) is given by:

$$P_{input} = \frac{{v_g}^2}{4R}. \qquad (2-78)$$

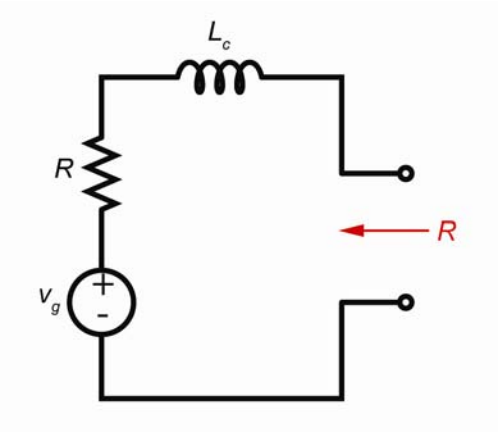

Figure 2-16: Surface coil model without matching network

The ratio of Equations $2-77$ and $2-78$ can be used to form the available power gain of the tuning and matching network:

$$G_a = \frac{{V_{out}}^2}{{v_g}^2}\frac{4R}{Re\{Z_{out}\}}. \qquad (2-79)$$

If the coil is tuned and matched to the characteristic impedance, then:

$$Re\{Z_{out}\} = Z_0, \qquad (2-80)$$

and because the matching network consists of only passive components, G_a is unity. It is then easy to determine the square of the matching network voltage gain:

$$\left(\frac{V_{out}}{v_g}\right)^2 = \frac{Re\{Z_{out}\}}{4R} = \frac{Z_0}{4R}, \qquad (2-81)$$

which has implications to the first stage gain G_1 of the cascade. Figures 2-15 and 2-16 are of the form required to perform circuit noise analysis, where v_g can now be replaced with the root mean square (RMS) noise voltage expected from a lossy coil with resistance R (69):

$$v_g = \sqrt{\overline{e_n^2}} = \sqrt{4kTR\Delta f}. \quad (2-82)$$

The square of the output noise voltage can be expressed as:

$$V_{out,noise}{}^2 = \frac{Z_0}{4R} 4kTR\Delta f = kT\Delta f Z_0. \quad (2-83)$$

To determine the output signal voltage, v_g can be replaced with the induced electromotive force (EMF) from the MR signal v_{MR}. The squared of the output signal voltage is then given by:

$$V_{out,signal}{}^2 = \frac{Z_0}{4R} v_{MR}{}^2. \quad (2-84)$$

The SNR is defined as the mean signal divided by the standard deviation of noise. From Equations $2-83$ and $2-84$, the SNR of the coil with tuning and matching circuit can be estimated by:

$$SNR \propto \frac{v_{MR}}{\sqrt{4kT\Delta fR}}. \quad (2-85)$$

Considering that R is actually composed of R_c and R_s, SNR can be rewritten as:

$$SNR \propto \frac{v_{MR}}{\sqrt{4kT_c\Delta fR_c + 4kT_s\Delta fR_s}}, \quad (2-86)$$

where T_c and T_s represent the temperature of the coil and sample/subject respectively.

From Equation $2-86$, RMS noise levels can be reduced by lowering the operating temperature T, the bandwidth Δf, and the resistance R. Unfortunately, the temperature of the subject should not be reduced *in vivo*. However, the temperature of the coil can be reduced. As such, cryogenically cooled coils that decrease T_c can significantly improve SNR (80). Unfortunately, cryogenically cooled coils are also cumbersome to design, manufacture, and use for routine imaging.

The coil and sample resistance are the final parameters of Equation $2-86$ which ultimately determine SNR. Sample loss is dependent on the coil geometry, how strongly the E-fields couple with the subject, and the conductivity of the subject. Varying the coil size not only varies the sample resistance, but also the coil resistance. The quality factor defined by:

$$Q = \frac{\omega L_c}{R}, \tag{2-87}$$

represents the ratio of energy stored to energy lost in a resonator, and gives a practical indication of coil performance.

Measurement of the coil Q with a lossy phantom/subject in place (the loaded condition) and without a lossy load (the unloaded condition) can give insight into the dominant source of loss. Larger Q_U/Q_L values indicate increasing dominance by subject over coil loss. This can be shown by dividing the unloaded Q:

$$Q_U = \frac{\omega L_c}{R_c}, \tag{2-88}$$

by the loaded Q:

$$Q_L = \frac{\omega L_c}{R_s + R_c}. \tag{2-89}$$

The unloaded to loaded Q is given by:

$$\frac{Q_U}{Q_L} = \frac{R_s + R_c}{R_c} = \frac{R_s}{R_c} + 1. \tag{2-90}$$

Rearranging terms gives a convenient formula for determining the dominant source of loss:

$$\frac{R_s}{R_c} = \frac{Q_U}{Q_L} - 1. \tag{2-91}$$

For a given coil size, it is desirable for losses to be dominated by the subject rather than the coil.

Low-noise preamplifiers represent the second stage of the cascade and are critical for low-noise operation. The preamplifier should have a low noise figure F_2 and a high gain G_2. The preamplifier should also present the correct output impedance to the third stage so that F_3 is minimized. Thus, if preamplifiers are designed with a low noise figure, high gain, and proper output match, the overall system noise can be minimized.

Preamplifiers are an important part of the receiver system, where the analog RF signal is mixed down to an intermediate frequency and then converted into the digital domain for further processing. Multichannel receiver systems have become the norm for clinical systems and have been offered as a system upgrade for small-animal research systems. Small animal MRI systems have traditionally been equipped with fewer receive channels than human systems.

Chapter 3: Selection of a Throughput-Optimized Array Geometry

As discussed in Chapter 1, the small size of the mouse in relation to the magnet bore permits the use of multi-animal MRI methods to improve imaging throughput on systems with multiple receive channels. However, the optimal placement of coils around (or within) a multi-animal volume for throughput-optimized imaging with a combination multi-animal and PI methods has not been established.

At present, small-animal MRI system electronics can support up to 16 parallel receiver channels. These additional channels offer new opportunities for achieving greater acceleration and throughput for functional MRI than have been previously reported. *The first specific aim of this work is to determine the optimal design of an array of up to 16 channels, for throughput-optimized multiple-mouse DCE-MRI.* In particular, the tradeoff between the numbers of animals to be simultaneously scanned, N, and the number of array elements that can be dedicated to each animal, C, was investigated. Extremes of this concept include the use of a 16-element coil array to scan a single animal, compared to the use of an array of 16 volume coils that are each dedicated to an individual animal (60).

A variety of potential array geometries, consisting of 16 or fewer receive elements, were considered for maximizing the throughput of a DCE-MRI mouse protocol. PI performance, based on g-factor maps, was used to determine which array configuration allowed the greatest imaging throughput without amplifying image noise beyond an acceptable level. Tolerable g-factors depend on the target anatomy, the application, and the baseline (unaccelerated) SNR including degradations indicated in Equation $2-62$. A throughput-optimized multi-animal coil configuration was selected based on achieving the maximum throughput that was under the g-factor threshold.

3.1 DESIGN CONSTRAINTS

Some practical design constraints were employed. The number of simultaneously-scanned mice was limited to five, which was previously shown to be most efficient for multi-mouse DCE-MRI (52). Although the size of small-animal research scanners varies, we imposed a limitation on the 7.0-T system that this project was developed for. With the largest gradient coil (BGA20), usable bore space is limited to only 20 cm. This poses significant limitations on the size of the RF coils and necessitates careful attention to coil decoupling.

3.2 DISTRIBUTED ARRAYS

Simulations were performed to select a throughput-optimized distributed array configuration. This consisted of two parts: selecting a unit subarray to surround each animal and comparing the throughput performance of distributed geometries made from replicates of the unit subarray.

3.2.1 Selection of Unit Subarray

To determine an optimal four-element subarray geometry that surrounds each mouse, SNR and uniformity simulations were developed in Matlab. For simplicity, circular coil elements were assumed. The four coil radii and their distance from a virtual 26-mm diameter cylindrical phantom were varied. By the principle of reciprocity, receive coil sensitivities can be determined from the field patterns generated in response to a unit current flowing on the coil loop (63). To estimate the signal for the SNR calculation, the spatially-dependent transverse component of $\boldsymbol{B}_1$ (i.e. $\boldsymbol{B}_\perp$) was determined according to the Biot Savart integral:

$$\boldsymbol{B}_1 = \frac{\mu_0 \boldsymbol{I}}{4\pi} \oint_{vol} \frac{d\boldsymbol{s} \times (\boldsymbol{r} - \boldsymbol{r}')}{|\boldsymbol{r} - \boldsymbol{r}'|^3}, \qquad (3-1)$$

where μ_0 is the permeability in free space, $\boldsymbol{I}$ is the directional current, $\boldsymbol{r}$ is the 3D position under investigation, and $\boldsymbol{r}'$ is the source current location.

Although noise in the receive electronics is not always negligible, the primary noise in the MR measurement depends on resistive losses in the coil and sample losses due to electric coupling with the sample, as discussed in Section 2.3.3. Losses from the coil were estimated according to the resistance of the loop conductor:

$$R_c = \frac{l\rho}{a} = \frac{\pi d\rho}{a}, \qquad (3-2)$$

where l is the length of the coil loop, d is the coil diameter, ρ is the resistivity, and a is the cross-sectional area, modified when appropriate to account for the skin effect (69). Losses from the sample were calculated as:

$$R_s = \sigma \int_{vol} |\boldsymbol{E}(\boldsymbol{r})|^2 dv, \qquad (3-3)$$

where σ is the subject conductivity, $\boldsymbol{E}$ is the electric field produced by a unit coil current, and the integral is over the whole subject volume (indexed by position vector $\boldsymbol{r}$) (79). The box surrounding the phantom, on whose surface the coils were positioned, was varied from 27 mm to 40 mm and the loop radii were varied from 5 mm to 25 mm (Figure 3-1). A SOS method was used to combine the coil data.

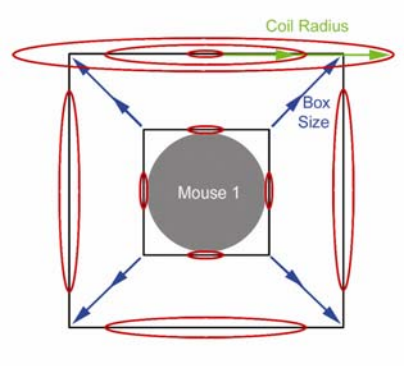

Figure 3-1: Variations in coil radius and distance from mouse

Relative SNR was calculated by dividing the transverse component of the $\boldsymbol{B}_1$ field by the square root of the total resistance:

$$SNR \propto \frac{\boldsymbol{B}_\perp}{\sqrt{R_c + R_s}}. \qquad (3-4)$$

Normalized surface plots for mean SNR over the whole phantom within the axial slice (Figure 3-2) and central SNR within the axial slice (Figure 3-3) are shown for various unit subarray geometries.

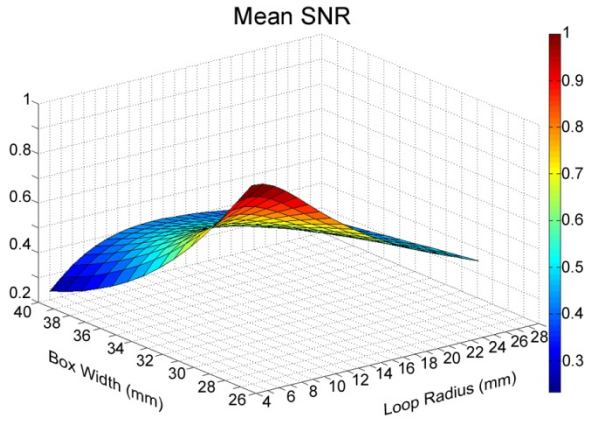

Figure 3-2: Mean SNR based on subarray geometry as a function of the box width and the loop radii

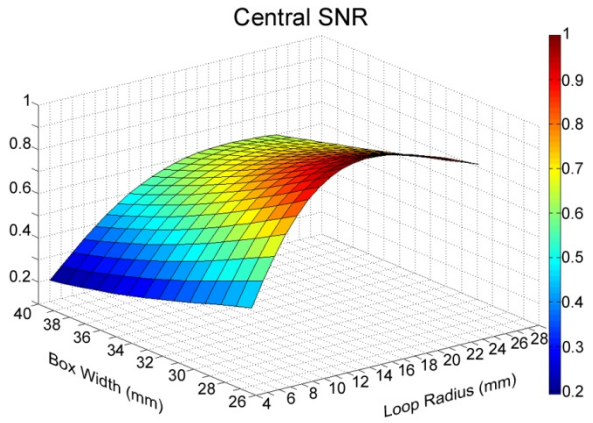

Figure 3-3: Central SNR based on subarray geometry

Mean SNR over the phantom monotonically decreases as box widths and coil loops go from small to large. For practical imaging however, SNR increases in the subject periphery should not be at the expense of central SNR. The plot for central SNR indicated an optimal coil size of 15-mm radius for the smallest box width that could surround the subject.

Image uniformity was calculated as the ratio of the mean to the standard deviation of the axial phantom slice. The resulting relative uniformity surface plot is shown in Figure 3-4.

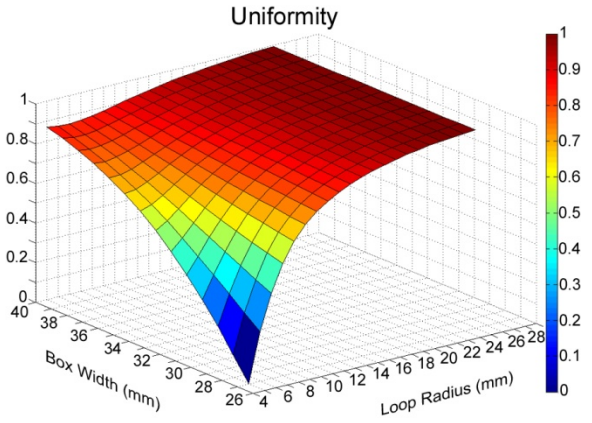

Figure 3-4: Predicted image uniformity based on geometry

To allow room for unobstructed entry of the mice into the array cavities, a box width of 28 mm was selected. At this value, the uniformity is more than 80%. Post-processing can be used to remove inhomogeneous coil modulation but would likely be unnecessary for general imaging.

3.2.2 Selection of Distributed Array

Throughput improvement is of little benefit if images from one animal are substantially worse than the image of another animal. To maintain consistent image

quality between mice, the unit subarray selected in Section 3.2.1 was replicated in a distributed fashion to cover five mice using 16 array elements. The three candidate geometries, including the +, ×, and linear geometries, are shown in Figure 3-5. The × geometry is simply the + configuration rotated by 45°. This may seem like a trivial modification, but differences between the coil geometry with respect to aliasing along the PE direction can have substantial impact on PI performance (39).

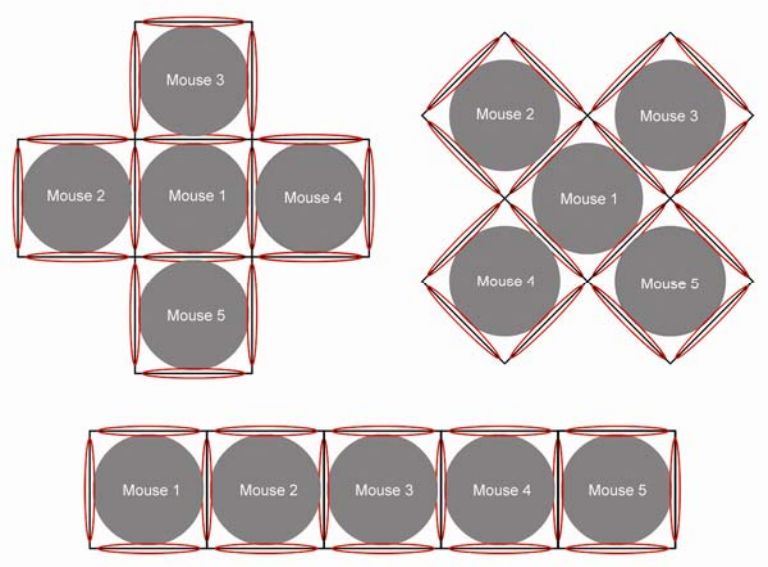

Figure 3-5: Front view of +, ×, and linear distributed array geometries

The $\boldsymbol{B}_1$ fields of each array element were calculated according to Equation $3-1$ and $\boldsymbol{B}_\perp$ was pointwise multiplied with numerical phantoms consisting of five homogeneous cylinders. This produced FOV_{full} coil images that were used to evaluate PI and consequently, throughput performance. To quantify throughput while avoiding confusion between scan acceleration and changes to the encoding matrix due to multi-animal imaging, throughput is defined as (59):

$$T = \frac{R \times N}{F}, \qquad (3-5)$$

where R is the traditional PI reduction factor, N is the number of simultaneously-scanned mice, and F is the factor by which the unaccelerated multi-mouse FOV is extended relative to the unaccelerated single-animal FOV. This relationship allows a consistent comparison between prescribing PI over a single-animal FOV to encode all animals (where $F = 1$) or applying PI over a larger multi-animal FOV (with $F > 1$). In general, g-factors will rise with increasing T, so the best performance is achieved with the lowest maximum g-factor for the highest throughput.

The 16 coil sensitivity images from the + geometry are shown in Figure 3-6. As can be seen, individual coil elements can be significantly sensitive to up to four mouse volumes.

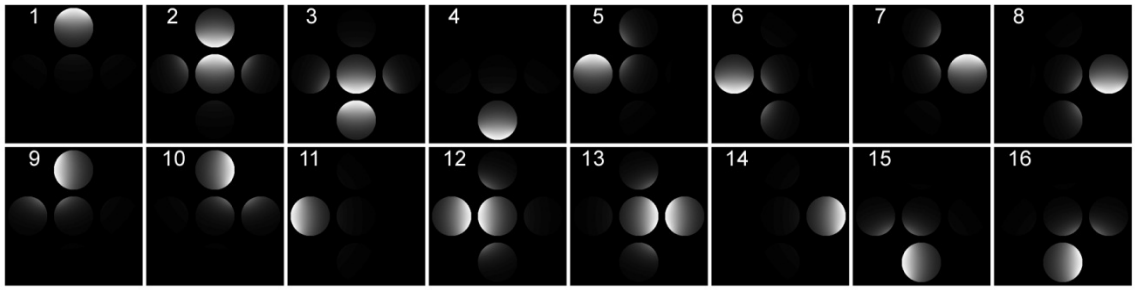

Figure 3-6: Sensitivity coil images from the + geometry

Maps of the SENSE g-factors (39) for the + configuration, were generated for reduction factors $R = 1$ to $R = 12$ (shown in Figure 3-7).

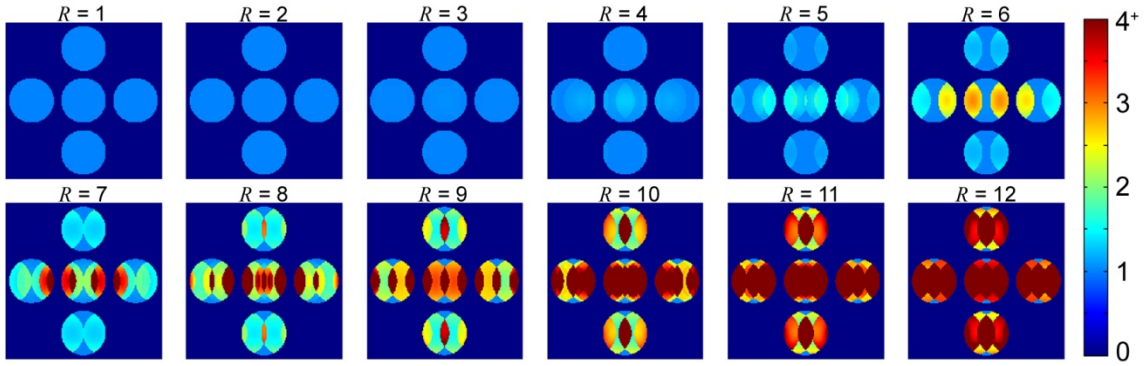

Figure 3-7: *g*-factor maps for the + array with PE in the L-R direction. Values greater than four were set to the maximum intensity level.

Coil sensitivity images from the × geometry are shown in Figure 3-8. Because × involves only a rotation of the + geometry, individual elements are likewise sensitive to up to four mouse volumes.

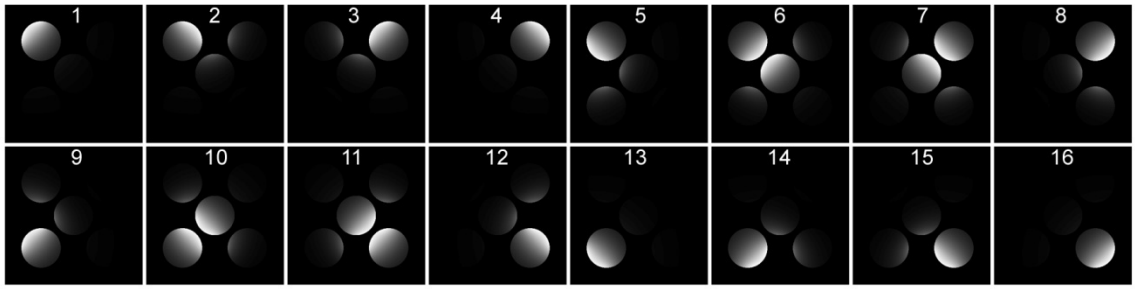

Figure 3-8: Sensitivity coil images from the × array

Resulting *g*-factor maps of the × geometry are shown in Figure 3-9. Note the different distribution of ill-conditioned regions of the *g*-factor maps caused by array rotation.

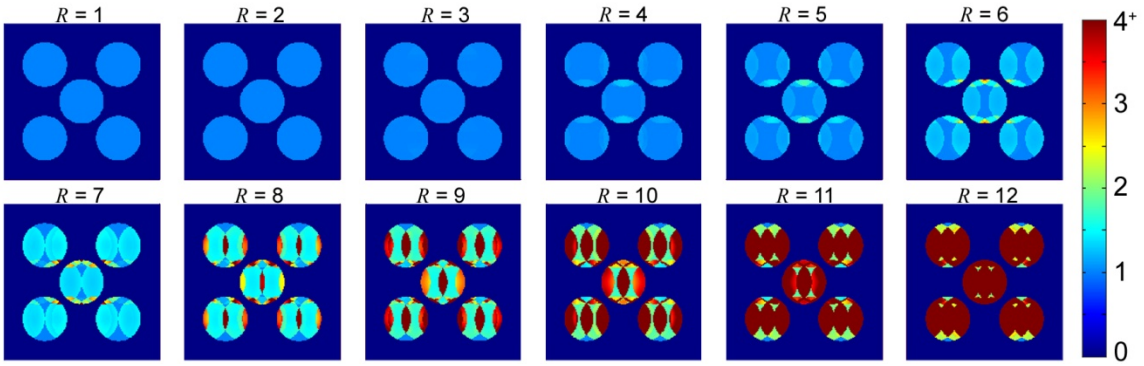

Figure 3-9: *g*-factor maps for the × array with PE in the L-R direction

Finally, coil images from the linear geometry were generated (Figure 3-10). With this geometry, array elements are substantially sensitive to up to three imaging volumes.

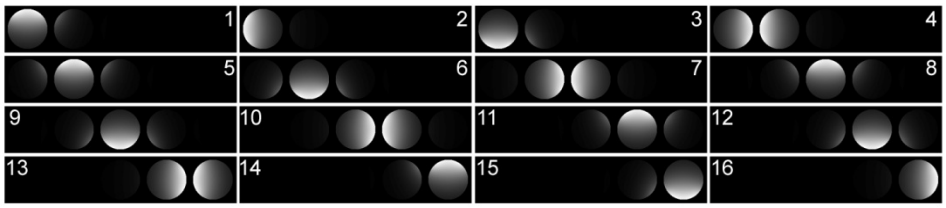

Figure 3-10: Individual coil images from the linear array geometry

Although the PI performance of the + and × geometries is independent of the applied PE direction, the performance of the linear geometry depends on the applied PE direction. Figure 3-11 illustrates *g*-factor maps with PE in the L-R direction, while Figure 3-12 shows maps with PE in the U-D direction.

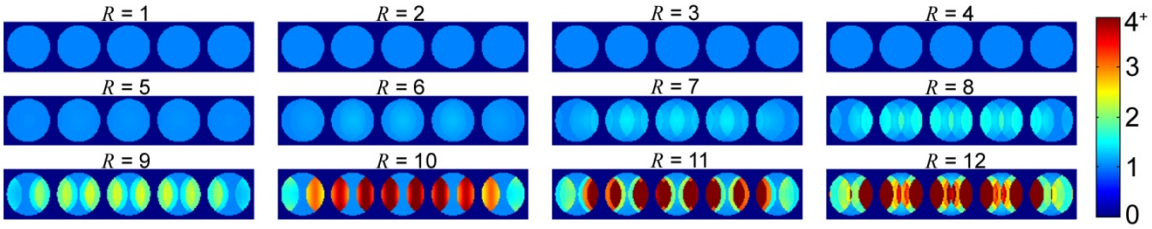

Figure 3-11: Linear array *g*-factor maps with a L-R PE direction

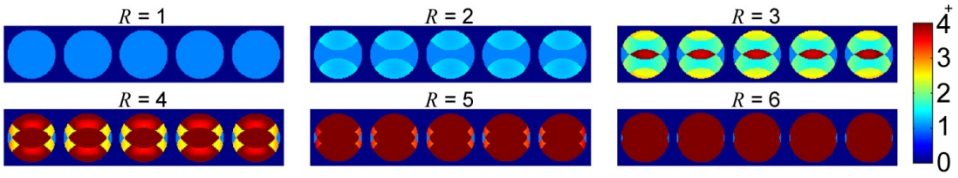

Figure 3-12: Linear array g-factor maps with an U-D PE direction

A maximum g-factor of two was chosen as the threshold, beyond which nonuniform noise amplification is considered too detrimental to image quality. Maximum g-factors as a function of reduction factors are shown in Figure 3-13 for the distributed configurations discussed above. The × and + geometries perform similarly whereas the performance of the linear array is highly dependent on PE direction.

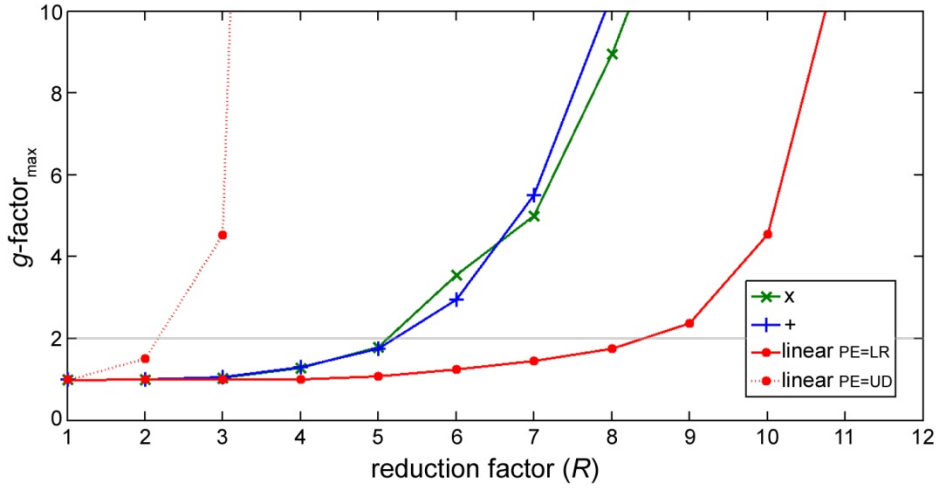

Figure 3-13: PI-performance based on various reduction factors

By applying Equation $3-5$ to the data, the influence of reduction factor and throughput become immediately apparent. The linear geometry with PE in the U-D direction can only achieve a reduction factor of $R=2$ before the $g=2$ threshold is surpassed in Figure $3-13$, whereas the throughput achieved with this configuration is more than 11 before reaching $g=2$ (shown in Figure 3-14).

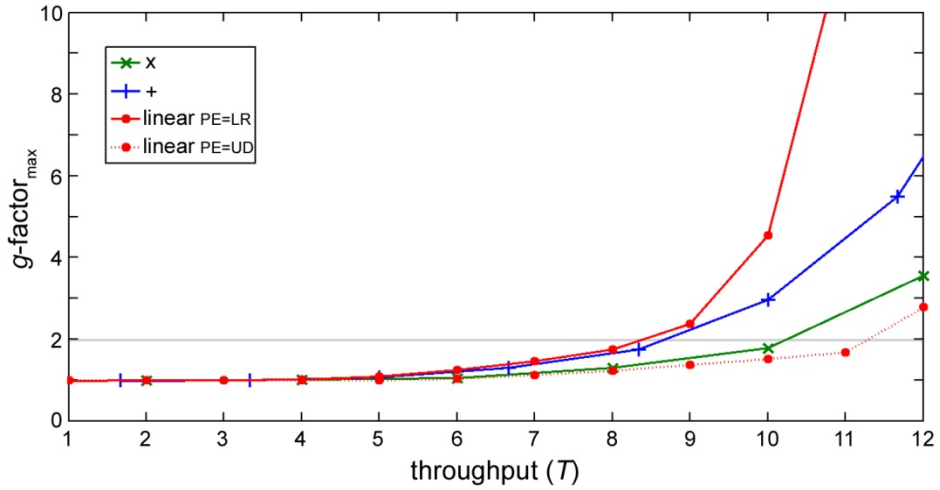

Figure 3-14: PI-performance based on achievable throughput

Table 3.1 illustrates the calculation of throughput based on R, F, and N. As shown, the × geometry and linear geometry with PE in the U-D direction perform similarly, with the linear configuration achieving a slightly higher throughput before $g = 2$ is reached.

Geometry	*R*max (*g*< 2)	*F* factor	*N* mice	Throughput *T*	RO FOV
+	5	3	5	8.33	3×
×	5	2.5	5	10	2.5×
linear PE L-R	8	5	5	8	1×
linear PE U-D	2	1	5	11	5×

Table 3.1: Characteristics of the distributed array configurations

3.3 Multiple Arrays of Receive Coils - MARCs

Thus far, the investigation of distributed arrays has neglected the propagation of motion artifacts between imaging volumes. In this section, decoupling requirements to minimize motion artifact propagation will be established. This is followed by an initial proof of principle study demonstrating the combination of PI and multiple-mouse MRI.

3.3.1 Motion Artifacts and Decoupling Requirements

The majority of multi-animal acquisitions to date have been performed on arrays of shielded volume coils. Shielding minimizes electromagnetic (EM) interactions between coils and VOIs, allowing propagation of motion artifacts from one animal to the others to be largely ignored. When arrays of surface coils are used, the impact of motion artifact propagation cannot necessarily be ignored. Simulations were performed in Matlab to determine the relationship between inter-array decoupling (i.e. decoupling of coils that are dedicated to separate VOIs) and motion artifact propagation.

Retrospectively-gated CMRI, which incorporates navigator signals in the pulse sequence to detect bulk changes in anatomy, allows randomly-ordered cardiac image data to be sorted and reconstructed according to phases of the cardiac cycle. Because this application represents the worst-case for image artifacts to propagate between animals with asynchronous cardiac cycles, it was used to determine multi-animal PI requirements. For example, when image data is reordered according to the cardiac phase of one animal, images of a second animal appear randomly ordered and can produce a motion artifact along the PE direction that can affect all animals.

Image quality and artifacts were analyzed by calculating B-fields for a pair of two-element arrays that were each dedicated to a separate VOI (59). Coil sensitivity maps of the four array elements were generated using a finite element simulation package (Comsol Multiphysics; Comsol AB, Stockholm, Sweden). Numerical phantoms consisted of a time series from two separate signal sources that represented two simultaneously-scanned mice. The central region of the phantoms represented the heart and the peripheral region represented homogeneous tissue. To simulate cardiac gating of one animal, the central region of the left mouse was fixed in diastole while the central

region of the right mouse was varied through 21 phases of a synthetic cardiac cycle by expanding and contracting the circular object into variously shaped ellipses (Figure 3-15).

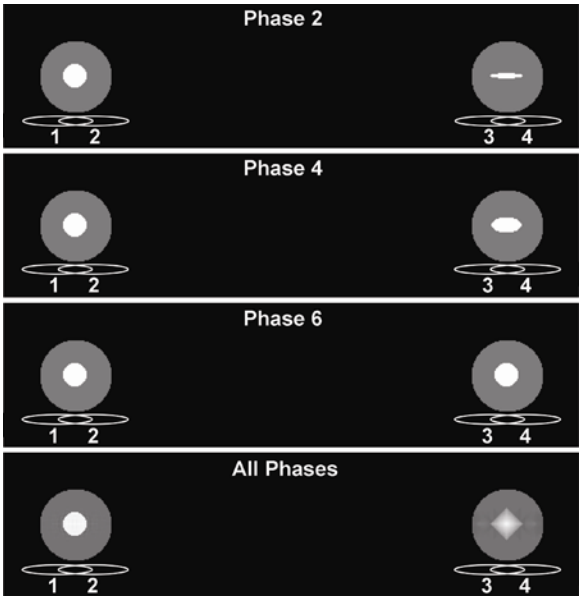

Figure 3-15: CMRI motion simulation with MARCs. The region representing the heart of the ungated animal was varied over 21 phases.

Synthetic *k*-space was generated by Fourier transformation of the 21 cardiac phase images that were each weighted by the four coil sensitivity maps. Intra-array elements were decoupled by 15 dB and coupling between inter-array elements was varied from 0 dB (fully coupled) to -20 dB by adding a fraction of the data from other channels to the channel of interest. Image SNR was varied from 0 to 100 by adding uniform noise to *k*-space data. To generate a synthetic acquisition that incorporated motion from the ungated animal, a new set of *k*-space was generated with each line taken from a random cardiac phase. The data was then downsampled according to a GRAPPA acquisition with $R = 2$. This process was repeated to produce 200 distinct sets of data to allow

characterization of mean artifact levels. A GRAPPA reconstruction was then performed on each repetition and the results were averaged.

An artifact-to-noise ratio (ANR) map was generated by independently calculating the effect of noise and coupled motion artifact. Artifact power within the gated VOI was determined by measuring the root mean square of the difference between a perfectly decoupled image and the image with coupled motion artifact. The simulations indicated that the conspicuity of motion artifact was dependent on image SNR and inter-array coupling. Figure 3-16 illustrates these relationships.

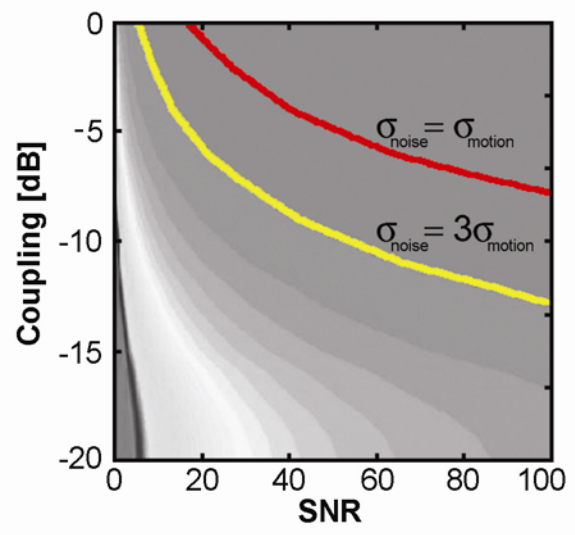

Figure 3-16: Motion artifact-to-noise ratio (ANR) map with two highlighted contours

Higher levels of decoupling are required to suppress the propagation of motion artifacts that are more pronounced as image SNR increases. Contours representing an ANR = 1 (in red) and ANR = 1/3 (in yellow) are indicated in Figure 3-16. Resulting GRAPPA-reconstructed images and error images that were generated by subtracting the reconstructed images from ideal images are shown in Figure 3-17. For an image with an SNR of 80, the motion artifact from coils that were highly coupled is pronounced,

whereas the motion artifact has primarily disappeared into the noise floor when inter-array decoupling was 12 dB. This value can therefore be used as the target decoupling criterion for inter-array decoupling.

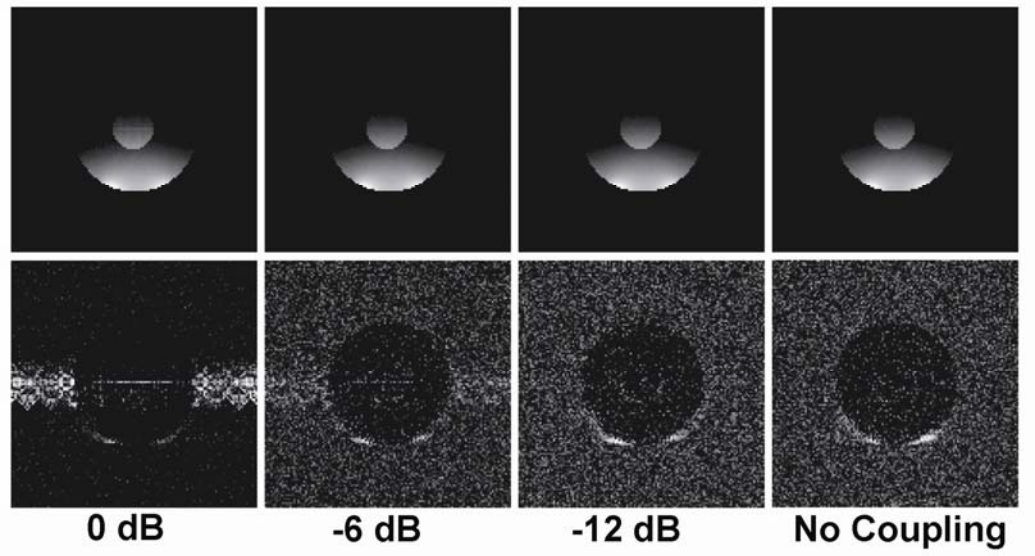

Figure 3-17: Motion artifact propagation based on inter-array coupling. Top: resulting combined image from gated phantom. Bottom: difference image illustrating coupled motion artifact.

The results of Figures 3-16 and 3-17, give powerful insight into the development of multi-animal phased arrays. For instance, the requirement for at least 12 dB of inter-array decoupling to eliminate propagated motion artifacts between mice indicates that distributed arrays are not likely the best solution for multi-animal MRI. For instance, the shared array elements of Section 3.2.2 are sensitive to multiple mice, indicating 100% coupling, or 0 dB of inter-array decoupling, between imaging volumes. This corresponds with the worst possible image degradation due to motion from other animals. Furthermore, minimizing mutual inductive coupling between receive elements, a requirement that will be discussed in Section 4.3.3.1, becomes increasingly complex as

the number of array elements increases. To simplify requirements, MARCs, in which independent subarrays are dedicated to separate imaging volumes and isolated either by physical distance or RF shielding, can be used instead of a distributed array. A feasibility study of parallel imaging with MARCs and a subsequent analysis of potential throughput-optimized MARCs configurations will follow in Sections 3.3.2 and 3.3.3 respectively.

3.3.2 Feasibility of Multiple-Mouse MRI with MARCs

Based on results from the CMRI coupling simulation, a pair of two-element phased arrays (Figure 3-18) was fabricated and used to demonstrate the feasibility of accelerating a multiple-mouse MRI experiment with parallel imaging (59).

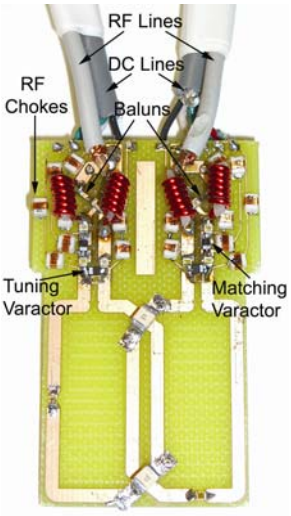

Figure 3-18: Photograph of a representative two-element phased array with labeled circuit components

Retrospectively-gated images of two PI-accelerated mice were simultaneously acquired with varying amounts of acceleration (Figure 3-19). SNR of images with up to a three-fold throughput improvement was not sacrificed compared with that achieved with commercial hardware. This was the result of coil design alone, where the unaccelerated

SNR of the phased array was 60% higher than that available with the standard 35-mm commercial mouse birdcage coil (59).

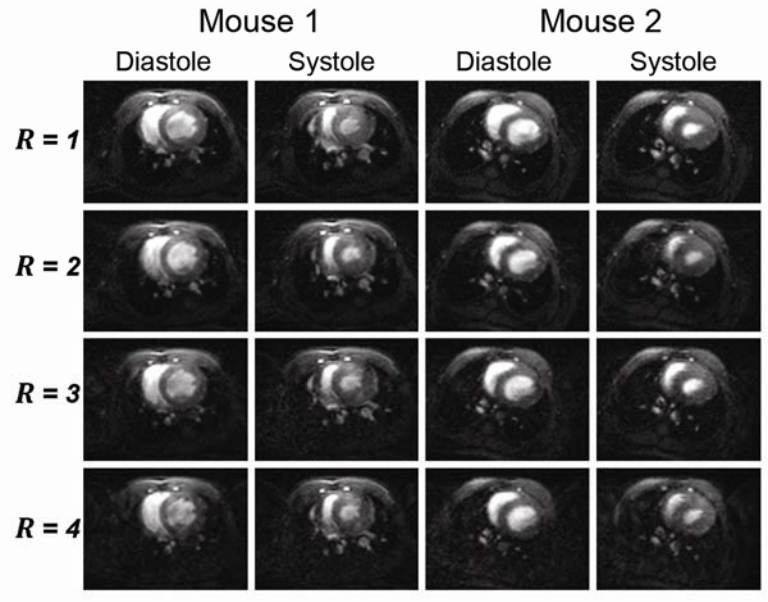

Figure 3-19: Accelerated dual-mouse CMRI with MARCs for $R = 1$ to 4

3.3.3 Selection of Shielded Array

Several configurations of RF-shielded subarrays, that varied the number of mice *N* and the number of proximal subarray elements *C*, were characterized based on parallel imaging and throughput performance. These array candidates were compared against the linear geometry of Section 3.2.2 to determine the throughput-optimized configuration for imaging with a 16-channel system. The green tubes shown in Figure 3-20 represent 28-mm inner diameter (ID) and 30-mm outer diameter (OD) cylindrical fiberglass substrates around which the coil elements would be placed.

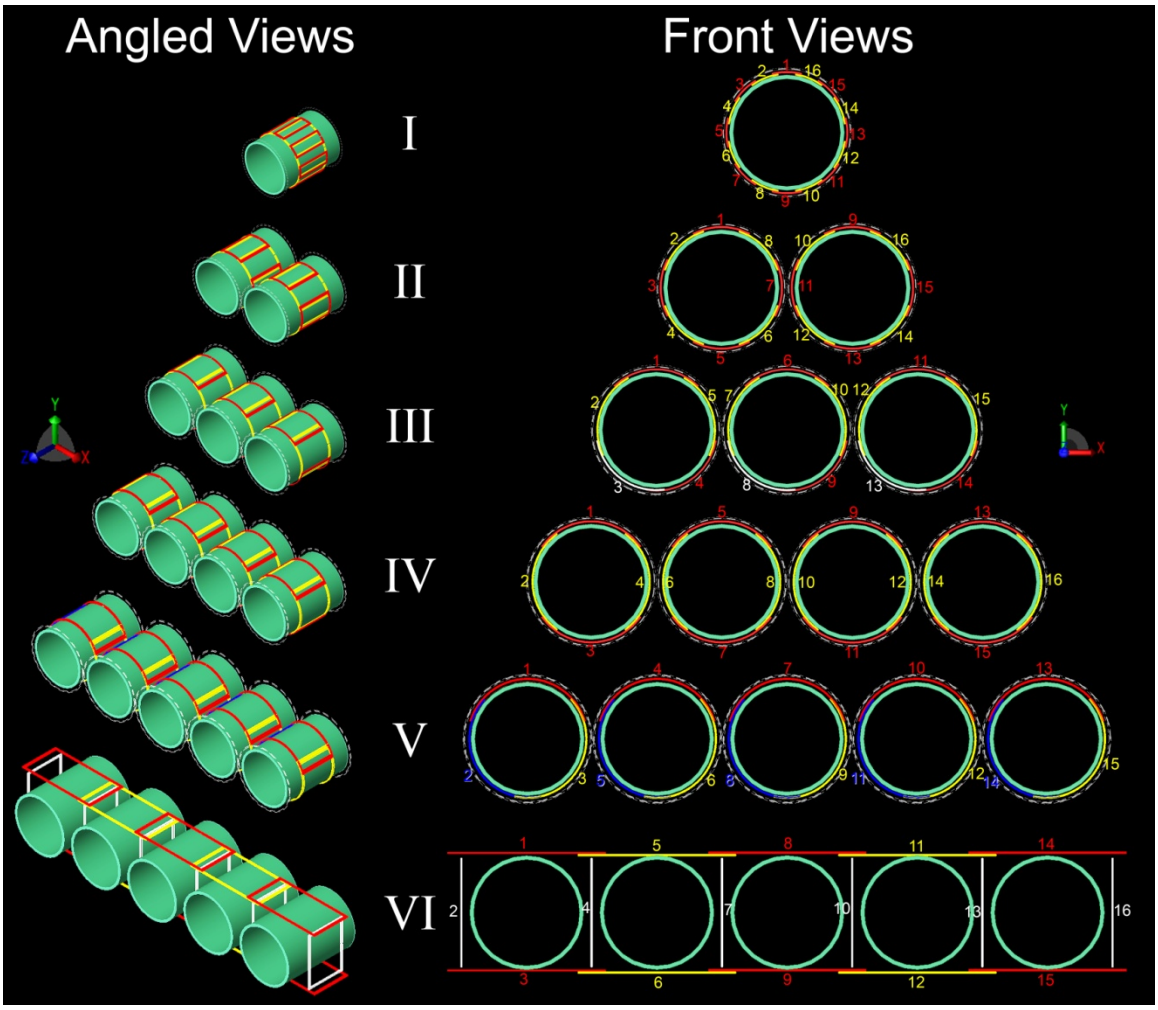

Figure 3-20: Coil configurations considered for imaging up to five mice. The array elements are alternated in yellow, red, white, and blue colors and are numbered to help clarify the physical locations. Dashed lines around subarrays represent RF shielding.

Configurations I to V represent imaging geometries in which individual subarrays are each contained within a shielded transmit coil for imaging $N = 1$ to $N = 5$ mice respectively. All coil elements extended 2.0 cm along the z direction and are overlapped with adjacent neighbors to approximate critical overlap for reducing mutual inductance (details of which are described in Section 4.3.3.1).

The coil configurations were modeled in a 3D EM software package, XFDTD 7.0 (Remcom, State College, PA) that can solve large EM problems in the time domain with excellent efficiency. By dividing 3D space into discrete segments, an iterative algorithm that updates fields at each step can quickly converge to an accurate solution. A source with a 300 MHz ramped sinusoid, corresponding with the proton resonance frequency at 7 T, was used to excite each of the array elements. The use of a GPU-based workstation permitted 30,000 time steps and a convergence of -35 dB in 19 minutes. Steady-state B-fields were collected over a central axial slab and were exported to Matlab, where the x- and y-directed field components were used to generate $\boldsymbol{B}_{\perp}$. These fields were then pointwise multiplied with numerical phantoms (represented by homogeneous cylinders) to generate individual axial coil images that covered the entire multiple-mouse FOV. Elements were assumed to be perfectly decoupled for this simulation. Coil sensitivity maps from the single-animal configuration (I) are shown in Figure 3-21.

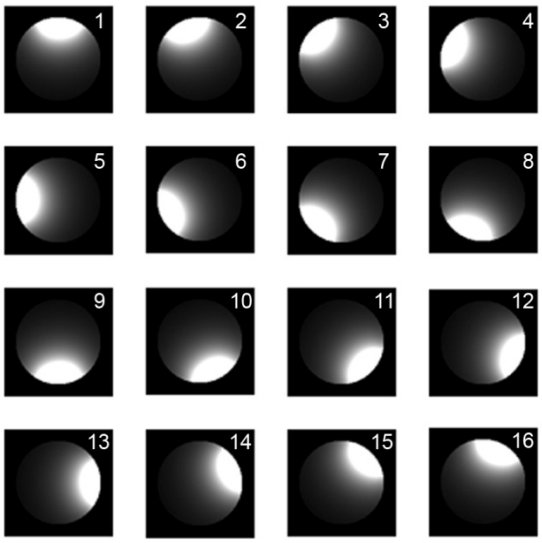

Figure 3-21: Configuration I coil sensitivity images

SENSE *g*-factor maps were calculated for each of the coil configurations and for reduction factors $R = 1$ to $R = 12$, using previously described methods (39). For all shielded configurations, PE was applied along the L-R direction as the RF shielding will largely negate performance differences due to the prescribed PE direction. Maps of resulting *g*-factors for configuration I are shown in Figure 3-22. Maximum *g*-factors remain below two for a reduction factor up to $R = 4$.

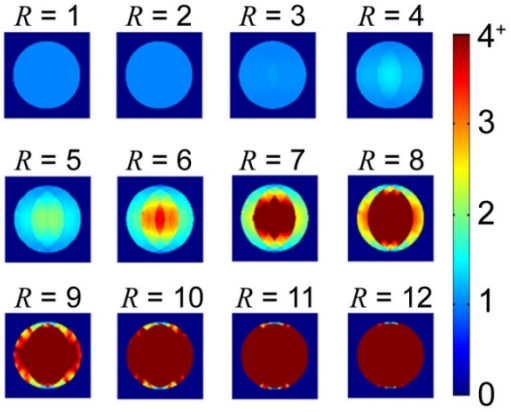

Figure 3-22: *g*-factor maps for configuration I

Coil sensitivity images of configuration II are shown in Figure 3-23. As shown, eight distinct views of each coil volume are achieved. By assuming an RF shield surrounding each subarray, coil sensitivities are limited to only a single mouse volume.

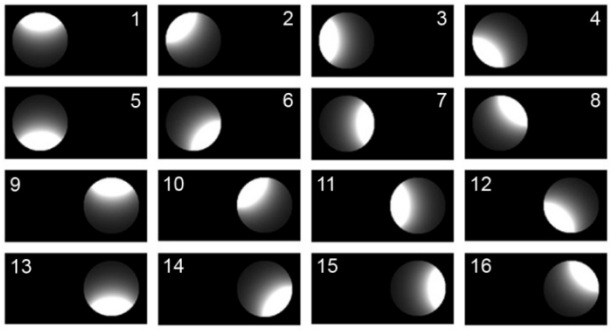

Figure 3-23: Coil sensitivity images of configuration II

The coil sensitivity images were used to generate the g-factor maps shown in Figure 3-24. The g-factor maps over each imaging volume are identical due to the subarray isolation resulting from RF shielding. This is true for all of the MARCs configurations in this section. Throughputs below eight result in $g_{max} < 2$.

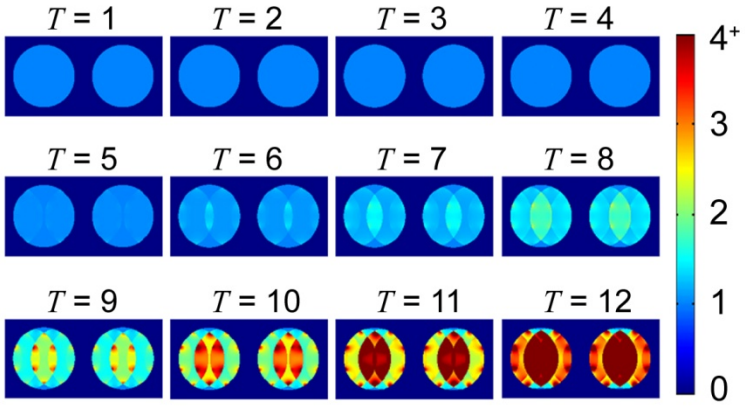

Figure 3-24: Configuration II g-factor maps

Likewise, sensitivity maps for configurations III, IV, V, and VI are shown in Figures 3-25, 3-27, and 3-29, while corresponding g-factor plots are shown in Figures 3-26, 3-28, and 3-30 respectively.

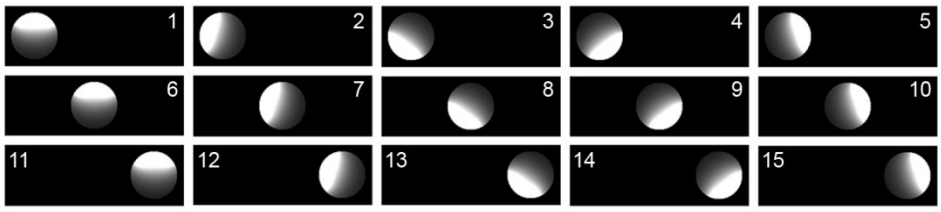

Figure 3-25: Configuration III coil sensitivity images

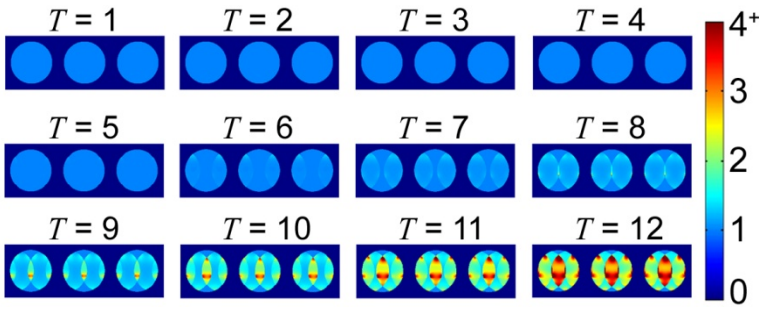

Figure 3-26: g-factor maps from configuration III

For configuarion III, a throughput of up to $T = 7$ results in g-factors below two.

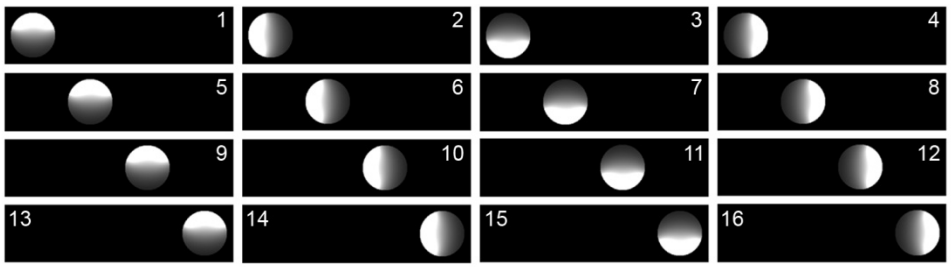

Figure 3-27: Array configuration IV sensitivity images

There is no SNR penalty due to the geometry of configuration IV when applying PI to achieve a throughput up to $T = 5$. Maximum g-factors continually increase up to $R = 10$, beyond which $g_{max} = 2$ is exceeded.

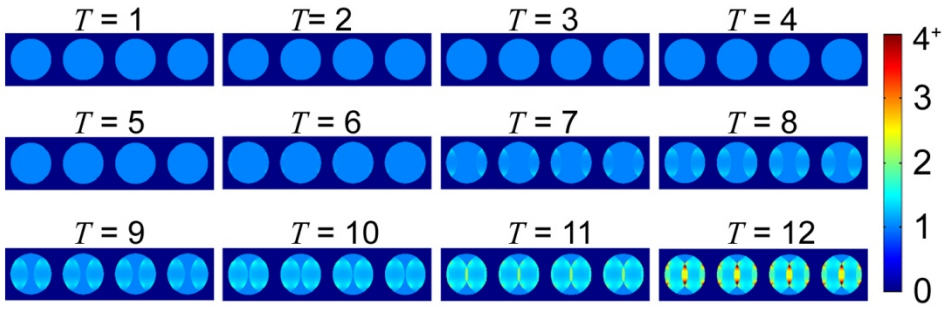

Figure 3-28: g-factor maps from configuration IV

Configuration V consists of C =3-element subarrays for N =5-mouse imaging. This geometry performs well, with g_{max}~1 for $R < 7$ and $g_{max} < 2$ for $R < 12$.

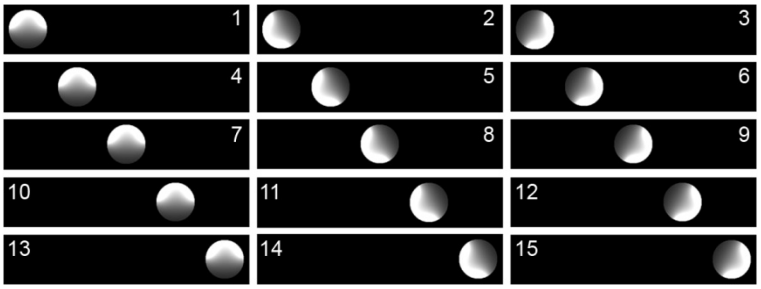

Figure 3-29: Sensitivity images from configuration V

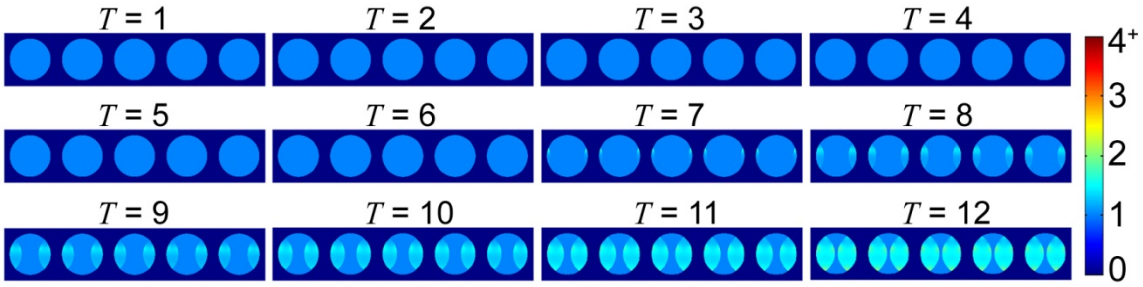

Figure 3-30: SENSE g-factor maps from configuration V

Maximum g-factors exceed two for $R > 8$ for configuration VI.

Equation $3-5$ gives the relationship between throughput T, the reduction factor R, the number of mice scanned at once N, and the matrix extension factor F. The shielded configurations I to V can use $F = 1$ in practice. However, for the simulations shown in this section, $F = N$. For example, the unaccelerated FOV and matrix was extended along the L-R PE direction by N times the single-animal FOV and matrix. Therefore, instead of comparing array configurations by the reduction factor, they can be compared based on achievable throughput T. Figure 3-31 shows combined g-factor maps for configurations I to VI for various levels of throughput.

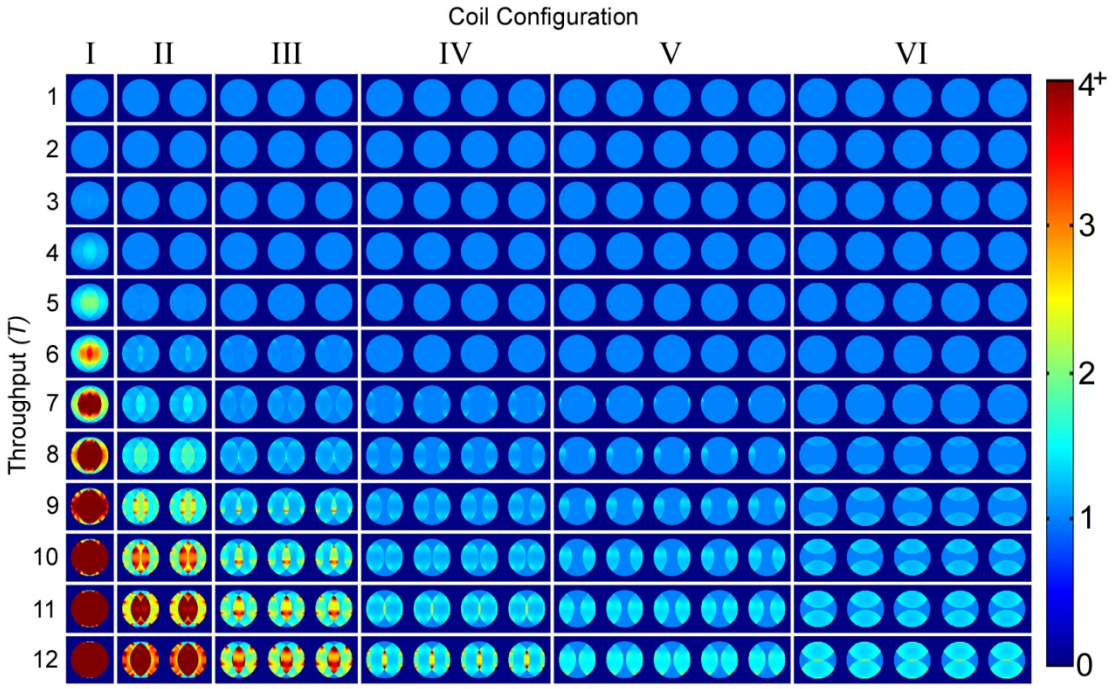

Figure 3-31: g-factor maps for $T = 1$ to $T = 12$ from six coil configurations

Plotting the performance of all candidate shielded configurations against the linear geometry, as done in Figure 3-32, facilitates selection of the throughput-optimized geometry. Configuration I (in which $N = 1$ and $F = 1$) results in rapidly increasing g-factors as T is increased. In contrast, the multi-animal configuration g-factors are largely unchanged from the ideal $g = 1$, until $T = 5$ and dramatic differences are noticed for $T > 5$. Configurations IV, V, and VI perform well, all capable of achieving $T = 10$. Configuration IV, in which $N = 4$ mice are simultaneously scanned, each with a four-element subarray, is a good selection if only gradients with a smaller ID were available or if animal handling and monitoring capabilities limited scanning to only four mice.

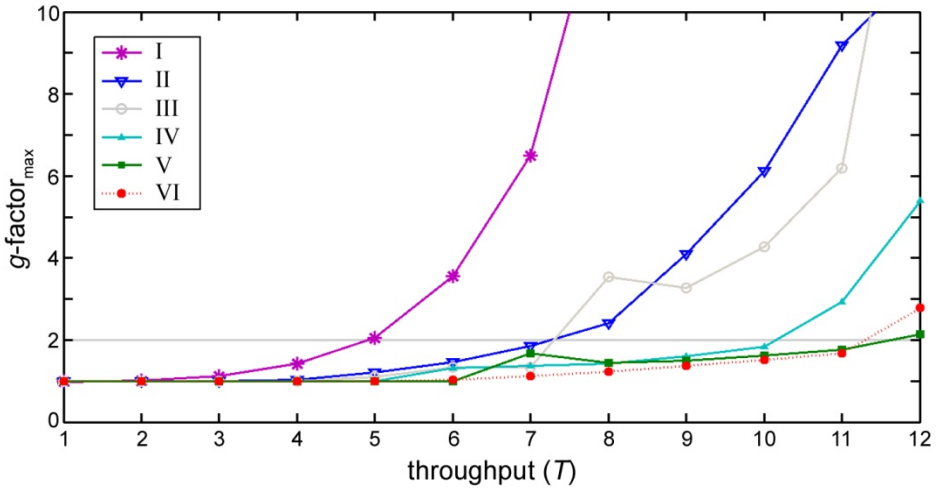

Figure 3-32: Maximum g-factors for various configurations and throughputs

Performance of the linear array is on par with configuration V, but requires complex decoupling procedures and will result in the propagation of artifacts between different animals. Because configuration V achieves $g < 2$ at a higher level of throughput than all other configurations, and because elements of each subarray can be intrinsically decoupled by geometric overlap alone, it was selected as the throughput-optimized array configuration.

Chapter 4: Hardware Design, Fabrication, and Evaluation

With the throughput-optimized coil configuration selected, implementation of the complex RF coil system and ancillary hardware can proceed. *The second specific aim of this work is to design, manufacture, and test the array system for optimized imaging performance*. In particular, design for maximum SNR, coil fabrication, decoupling strategies, bench-based validation, and assessment of unaccelerated and accelerated imaging performance will be described.

4.1 TRANSMIT COILS

Using an RF-shielded transmit coil to limit the receive coil sensitivities can improve PI performance, reduce the propagation of motion artifacts between animals, and simplify the strategy for mutual inductive decoupling. In this section, the design and fabrication of five volume coils to homogeneously excite the imaging volume are described.

4.1.1 Design and Fabrication of Transmit Coils

To maintain a simple, well-established design for the transmit coils; linear eight-rung high-pass birdcage coils were selected. To isolate the transmit coils and to limit each of the receive coil sensitivities to a single mouse, RF shielding was incorporated. Requirements to fit five coil modules within a 20-cm bore space and to maximize the distance between receive and transmit coils, required careful planning of the coil geometry. As shown in Figure 4.1, two sets of fiberglass tube formers with a 50.7-mm OD and a 63.6 OD were chosen to support the birdcage circuitry and the RF shield respectively. Based on these dimensions, the Birdcage Builder application (81) was used to estimate capacitor values for tuning the coil to the homogeneous mode at 300.3 MHz

(corresponding with the proton resonance frequency at 7 T). Although the software predicted use of 13.9 pF capacitors, 16 pF capacitors were ultimately selected after several bench-based tuning iterations. Figure 4-2 shows the birdcage coil schematic.

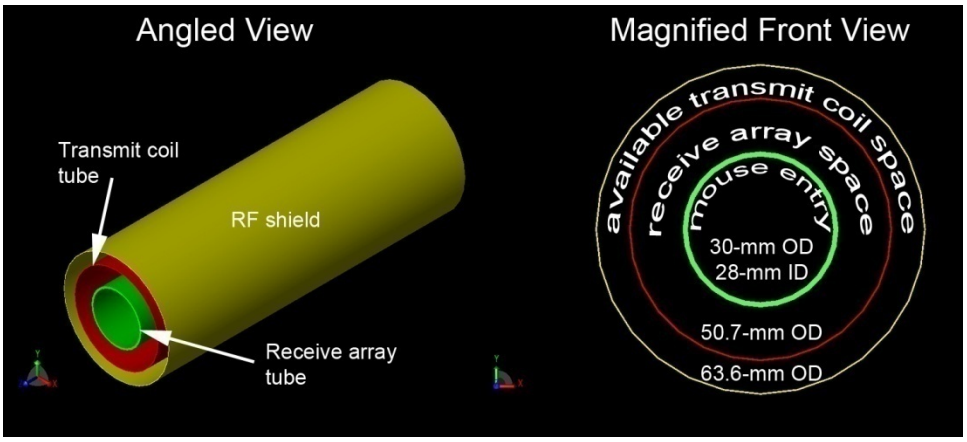

Figure 4-1: Diagram and dimensions of fiberglass coil formers illustrate the limited space for RF circuitry

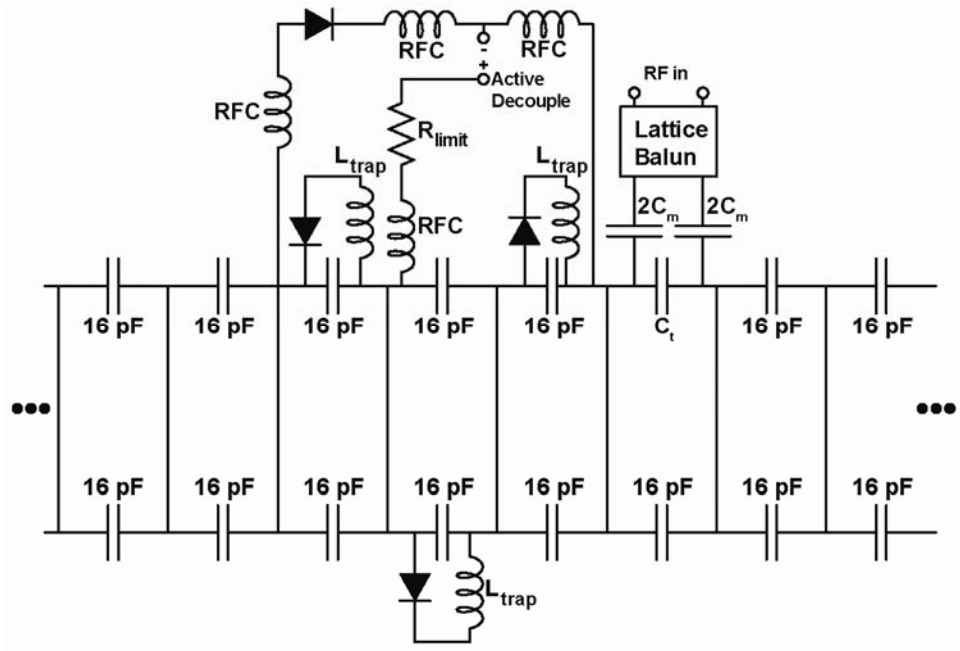

Figure 4-2: Circuit schematic of linear, high-pass birdcage coils with decoupling circuitry

The birdcage rungs were made 6 cm long so that the excitation volume would be large enough to cover the entire mouse body and 6 mm wide to reduce the coil resistance R_c. Lattice baluns reduced RF interactions between adjacent RF cables. A photograph of the five unshielded birdcage coils is shown in Figure 4-3.

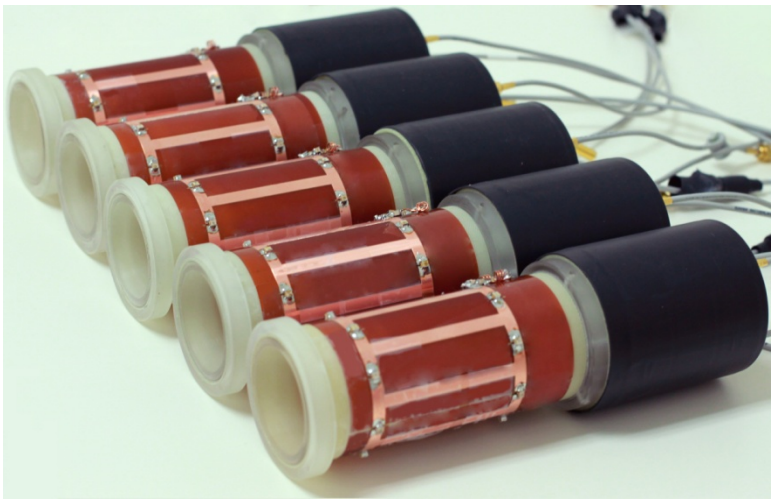

Figure 4-3: Photograph of transmit birdcage coils with RF shields removed

4.1.2 Driving Multiple Transmit Coils

Only one transmit channel is available on the 7-T MRI system. To simultaneously drive the five birdcage coils required development of a five-way power splitter/combiner. Commercially available dividers are rarely capable of operating at high power levels and are typically suited for wideband operation. For this application, low insertion loss is critical for achieving adequate distribution of power with relatively low transmit pulse durations. Therefore, a Wilkinson power divider, rather than a resistive divider, was implemented for operation at 300 MHz (69). Wilkinson dividers are typically implemented with quarter wavelength cables of characteristic impedances that depend on the system characteristic impedance (here, $Z_0 = 50$) and the number of channels. For a five-way divider, a cable with a characteristic impedance of $\sqrt{5}Z_0 =$

111.8 Ω would be required. To avoid difficulties associated with finding a rare cable, the divider was realized with π networks to create discrete equivalents of quarter wavelength lines. A schematic and photograph of the resulting divider is shown in Figure 4-4.

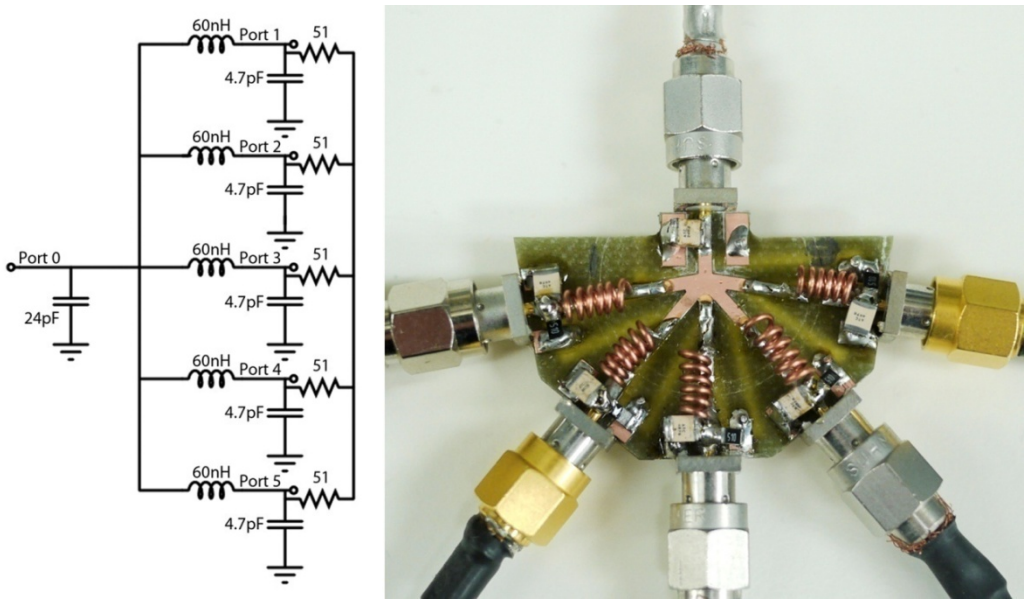

Figure 4-4: The circuit schematic (left) and photograph (right) of the 5-wayWilkinson power divider/combiner.

S-parameters, theory of which is described in Appendix A, are shown in Table 4.1.

transmit from port *y* \ receive from port *x*	**0**	**1**	**2**	**3**	**4**	**5**
0	-	-6.7	-7.7	-7.8	-7.9	-7.9
1	-	-	-27.0	-26.3	-21.7	-19.0
2	-	-	-	-18.3	-25.1	-23.3
3	-	-	-	-	-17.9	-25.5
4	-	-	-	-	-	-21.8
5	-	-	-	-	-	-

Table 4.1: Attenuation *S*-parameters for Wilkinson power divider

Insertions losses S_{10} to S_{50} are all below 8.0 dB, and the average value of 7.6 dB is only slightly above the ideal theoretical value of 7 dB. This is critical for efficiently splitting RF transmit power. S_{10} has the lowest insertion loss (6.7 dB) compared with the highest (7.9 dB) from S_{40} and S_{50}. Variable attenuators can be used to equalize transmission coefficients to achieve identical excitation power. The worst-case divider cross coupling is S_{43} = -17.9 dB and the average cross coupling is -22.59 dB.

4.2 RECEIVE ARRAYS

As discussed in Section 2.3, receive arrays of surface coils offer improved SNR compared with volume coils, and if properly designed, also offer the ability to trade excess SNR for imaging speed by reduced signal averaging or with PI. Details of the design and fabrication of the three-element receive subarrays of coil configuration V will now be discussed.

4.2.1 Coil and Sample Losses

In an effort to minimize losses from the array coils, the impact of the coil loop structure was analyzed. Wiggins *et al* have recently claimed that coil conductors made from wire with a circular cross section may be preferred over wider conductors for large coil arrays (71). For developing multi-animal arrays in this work, two copper loop structures were compared based on Q measurements and image-based SNR performance. A pair of surface coils, sized according to the configuration V simulation of Section 3.3.3, was made from a circular 18-AWG copper wire and a 1.5-mm milled copper trace as shown in Figure 4-5.

Figure 4-5: Coils made from a 1.5-mm copper trace and an 18-AWG wire were compared

Five phantoms filled with 50% saline, 50% water, and doped with 0.01% Magnevist were created from 30 mL syringes to approximate the loading characteristics of a 30 g mouse. Two independent loop probes were loosely coupled to each of the coils in turn, with and without the same loading phantom in place, to determine if the dominant source of loss was due to the coil R_c or the sample R_s. Q, theory of which is described in Section 2.3.3, was estimated according to:

$$Q_{est} = \frac{f_0}{\Delta f_{-3dB}}, \qquad (4-1)$$

where f_0 is the resonance frequency and Δf_{-3dB} is the -3 dB bandwidth of the resonant peak.

The coil made from the 18-AWG copper alloy wire had a Q_U/Q_L = 189/124 = 1.53 and the coil made with a 1.5-mm copper trace had a Q_U/Q_L = 194/121 = 1.60. For both cases, R_s/R_c is less than one, which implies that the coils are operating in a coil-loss dominated mode. For the coil made from a 1.5-mm trace, the coil makes up 63% of the

loss while the sample makes up 37% of the loss. Alternatively, the coil made from 18-AWG has 65% of its loss due to the coil and 35% due to the sample.

To validate these bench-based measurements, the coils were also compared through imaging experiments. The same loading phantom was sequentially scanned with each of the surface coils and a commercially available preamplifier (Advanced Receiver Research, Burlington, CT) with a spin echo pulse sequence (TE/TR = 14.5/1000 ms, FOV = 3 × 3 cm, matrix = 256 × 256, slice thickness = 1.0 mm, and 100 repetitions). The imaging experiment was also repeated with the Bruker 1P 8102 birdcage coil and preamp, which is the standard configuration used for mouse imaging at our institution. Resulting images and SNR maps, as calculated from the mean and standard deviation of each pixel along the temporal series, are shown in Figure 4-6.

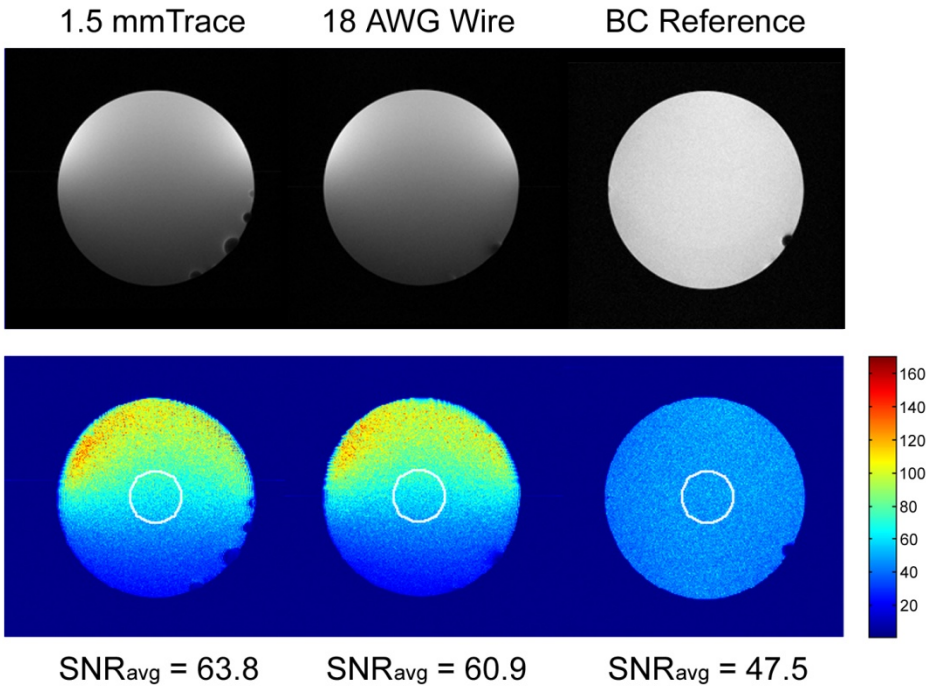

Figure 4-6: Images and SNR maps from different coil conductor shapes

It is evident that both surface coils produce a substantial SNR improvement in the center of the phantom, and much higher SNR in the phantom periphery near the coil conductors, compared with the birdcage coil. For array coils, images from several surface coils are combined to produce a composite image with SNR properties related to the individual coil images. Thus, the results achieved here indicate that a three-element subarray made from replicates of this coil structure can achieve dramatically higher image quality than that of the standard hardware; affording its use for improving imaging acceleration and ultimately data throughput.

The coil made from a milled 1.5-mm copper trace achieved slightly higher SNR in the central portion of the phantom than did the coil made from copper wire (63.8 vs. 60.9 respectively). These results are consistent with bench-based Q measurements. The effective cross sectional area, taking into account the RF skin depth, was 0.0122 mm^2 for the 18-AWG wire and 0.0115 mm^2 for the 1.5-mm trace, indicates a slight inconsistency. Although the cross sectional areas and SNR measurements were both within 5% for the two configurations, the modest SNR benefit of the 1.5-mm trace is counter intuitive. A possible explanation of this discrepancy could be explained by imperfect solder joints where capacitors were added to the coils. Nonetheless, the use of a 1.5-mm milled copper trace is significantly preferred for ease of manufacture and for achieving repeatable coil characteristics.

4.2.2 Fabrication of Receive Coils

Based on results learned from a single surface coil, five individual three-element subarrays were fabricated. The inner coil structure was made from G-10 tubing with a 28-mm ID and 30-mm OD as shown in Figure 4-1. Spacer rings that support the outer transmit coil structure and shield were milled from acrylic, and cable guide holes were

drilled to allow coaxial cables to connect from the coils to the preamplifiers. Additionally, a tapered entry into the receive coil was added to facilitate guiding of mice into the subarrays. Due to spatial constraints of gradients and the multiple imaging volumes, limited space was available for components of the receive coils.

Coil pairs with varying overlap were milled from a flexible copper substrate. All coils extended 2.0 cm along the *z*-axis and ranged from 3.0 to 3.5 cm along the angular/circumferential direction in 0.5-mm increments. Each loop pair was sequentially tested for overlap decoupling (details of which are described in Section 4.3.3.1). Once the critical overlap was determined, the subarray layouts were designed and milled. A schematic of a receive array element is shown in Figure 4-7. Balance was achieved by maintaining a virtual ground through symmetry of components (i.e. capacitors C and C_t) on each coil element. Cable lengths that transformed the low input impedance of the preamplifiers to a high impedance at the coil, to minimize currents and coupling as discussed in Section 4.3.3.2, were systematically determined. A photograph of the resulting subarrays and preamplifiers is shown in Figure 4-8.

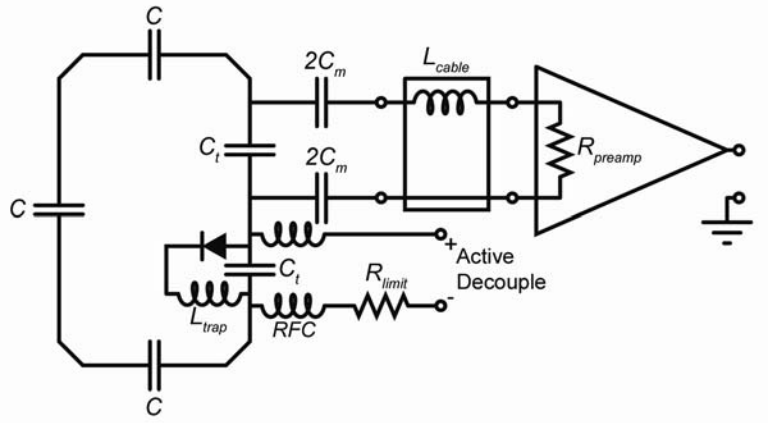

Figure 4-7: Circuit schematic of a representative receive element

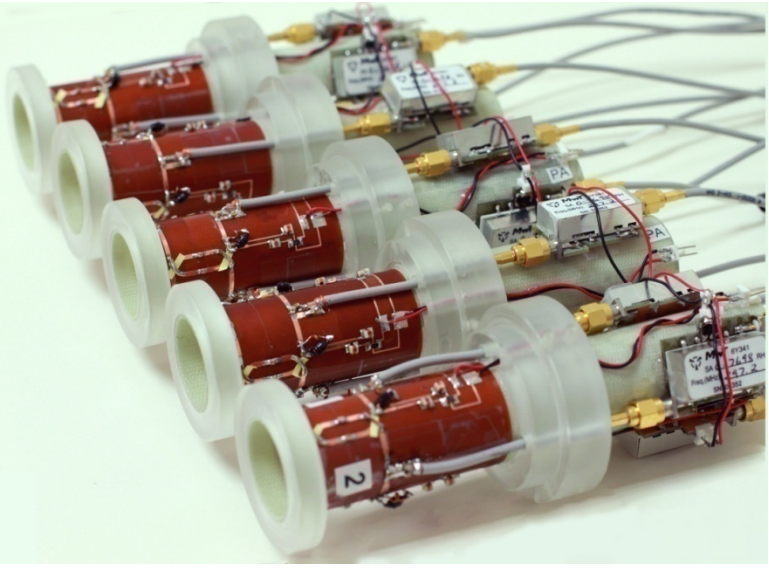

Figure 4-8: Photograph of the five three-element receive subarrays and associated low-noise, low input-impedance preamplifiers

4.3 ARRAY SYSTEM

After fabricating the transmit and receive coils, the subarray modules were combined into a 20-coil array system. Details of the assembly and characterization of the array system are described in this section.

4.3.1 Coil Assembly

A coil holder was designed and subsequently manufactured with acrylic material to fit snugly into the BGA20 gradient coil. Cable guide holes were included to reduce interactions of the coaxial cables that extend from the preamplifier output to the rearmost connector panel. To further reduce coupling between cables, coaxial baluns were manufactured by forming flexible coaxial cable into a solenoid and placing a tuning capacitor across the outermost turns, creating a high impedance on the outer shield at the operational frequency.

Because of the tight 20-cm gradient bore space and the coil OD, the five coil modules were staggered as shown in Figure 4-9. As described in Section 4.3.4, the spatial offset can be accounted for by offsetting the frequencies of receive channels that correspond to the mouse position along the RO direction. Thus all imaging VOIs can be encoded with a FOV that covers one smaller volume (41), and the g-factor maps calculated for configuration V in Section 3.3.3 are still valid.

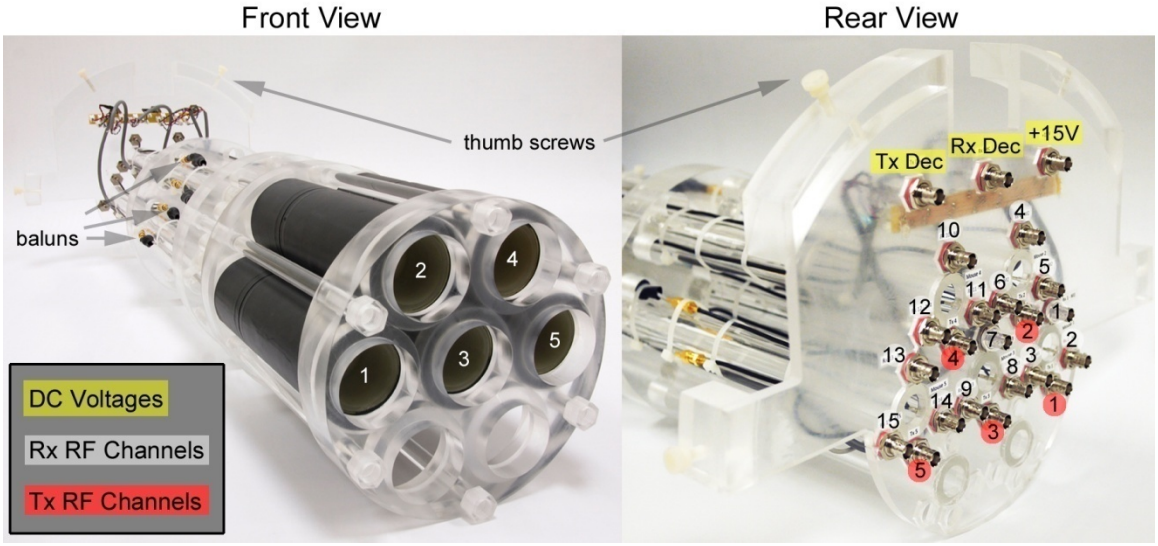

Figure 4-9: Multi-coil holder assembly illustrates staggered geometry and the ports for RF and DC signals

4.3.2 Tuning and Matching

As discussed in Section 2.3, all coils must be matched to 50 Ω at 300.3 MHz for low-noise operation. Therefore, loading phantoms were placed within each coil and C_t and C_m were varied to tune and match each of the receive and transmit coils. Network analyzer-based S_{11} measurements were first captured for each of the 15 receive elements as shown in Figure 4-10. Although fixed rather than variable capacitors were used, tuning and matching for all receive coils is excellent.

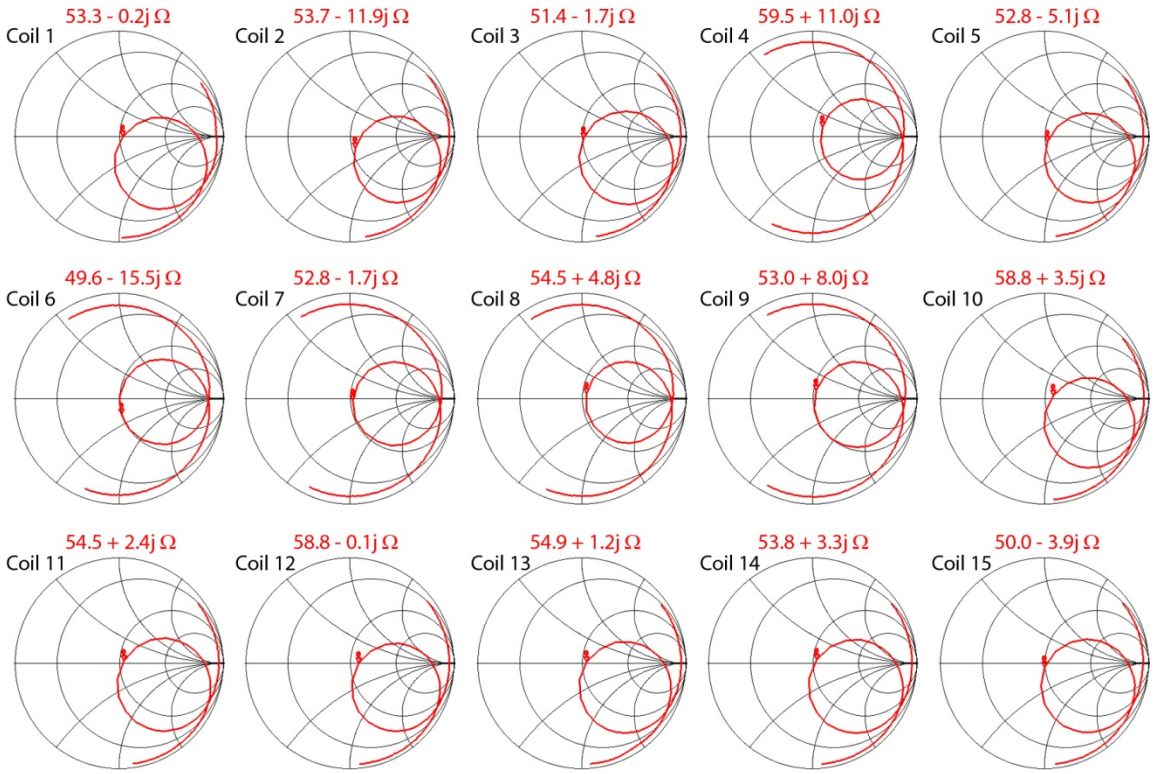

Figure 4-10: Receive element S_{11} measurements for evaluating tuning and matching

To tune and match the transmit coils, the receive coils were actively decoupled (as described in 4.3.3.3) and the tuning and matching capacitors (C_t and C_m as shown in Figure 4-2) were iteratively varied while monitoring the output on a network analyzer. Resulting S_{11} values covering a 50 MHz span are plotted on the Smith Charts in Figure 4-11 with and without the receive coils actively decoupled. With receive coils actively decoupled, transmit coils were tuned to approximately 50 Ω . When active decoupling was disabled, two resonances due to split peaks are evident (shown in the bottom row of Figure 4-11). Tuning and matching of the transmit coils was also performed with the array system inserted into the MRI scanner. As indicated in Figure 4-12, results are

highly consistent between coils. The minor shift in optimal match can be easily compensated by a slight increase in applied transmit power.

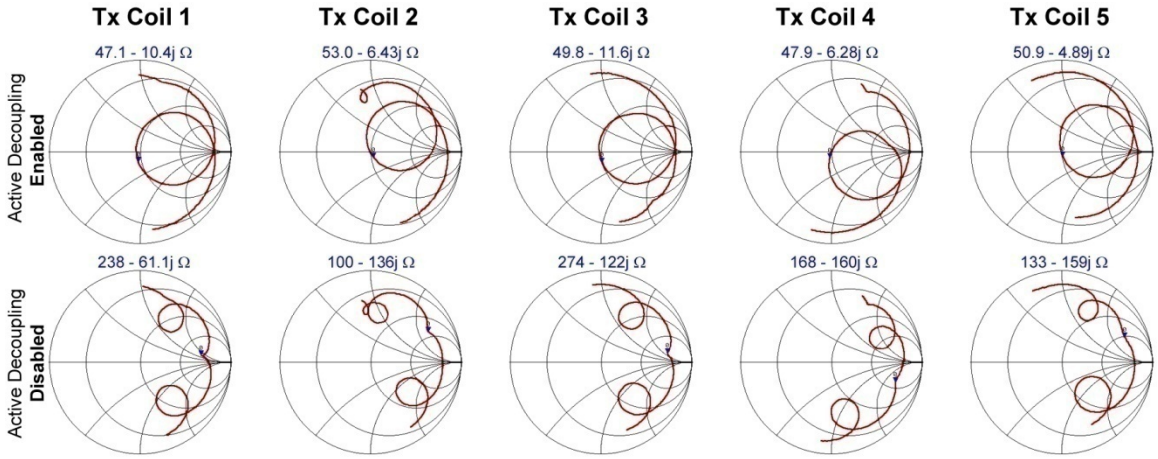

Figure 4-11: Transmit coil S_{11} bench measurements with (top row) and without (bottom row) receive coils actively decoupled

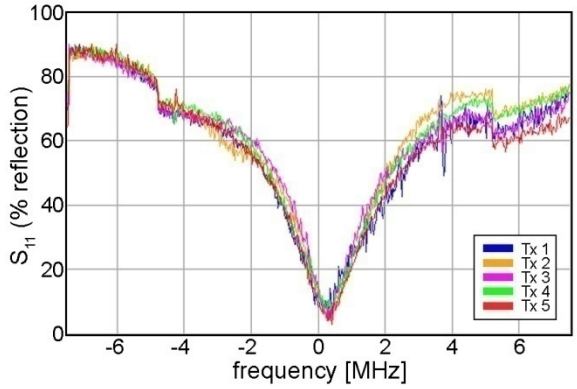

Figure 4-12: Tuning performance of the five transmit coils at the MRI scanner

4.3.3 Decoupling

4.3.3.1 Inductive Decoupling

When multiple surface coils are combined into an array, mutual inductive coupling of the coil elements (see Section 2.3.2) will reduce the uniqueness of the coil sensitivities to degrade SNR and PI performance (i.e. will increase g-factors). Fortunately, there are several methods to reduce coil coupling. A first strategy is to reduce the mutual inductance by geometric placement of the coils. That is, to design coils such that $M_{21} = 0$. A crude solution is to separate the two coils by a large distance. Likewise, two coil elements can be placed orthogonal to each other so that flux from the primary coil goes equally into and out of the secondary coil. Unfortunately, the placement of array elements is typically dictated by the geometry of the patient/sample, only making this method practical for a limited number of applications.

Overlap decoupling is a special case of mutual decoupling where the flux Φ_{21} is cancelled with coils in close proximity to each other. As shown in Figure 4-13, the current induced in the primary loop i_1 generates a flux Φ_{21} that travels both into and out of the secondary coil. If the two coils are precisely overlapped, the flux into the secondary coil (shown with + symbols) will destructively add with flux out of the secondary coil (with o symbols) and M_{21} of the coils will be minimized.

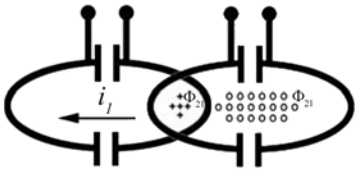

Figure 4-13: Overlap decoupling to cancel mutual inductance

Capacitive networks can also be used to cancel mutual inductance (82). Although this method has successfully canceled mutual inductance (83,84), the network becomes prohibitively complex as the number of elements in the array increases. Inductive decoupling, where physical inductors rather than capacitors are adjusted between coils, can also be used in cases where decoupling capacitor values are impractically small (83). However, inductors typically introduce substantially more loss than do capacitors, resulting in reduction of coil Q (85). For sample-loss dominated coils, the coil loss due to the inductors may be negligible compared with sample losses, and inductive decoupling is a suitable method. For small-animal imaging where coil-losses often dominate sample losses, inductive decoupling is typically not desirable.

To investigate inductive coupling between receive elements, S-parameters were made by removing preamplifiers and transmitting into coil y and receiving through coil x. The full complement of measurements in shown in Table 4.2.

S_{xy}[dB]	port *x*														
port *y*	*1*	*2*	*3*	*4*	*5*	*6*	*7*	*8*	*9*	*10*	*11*	*12*	*13*	*14*	*15*
1	**0**	**-17.6**	**-16.0**	-53.3	-58.6	-65.1	-58.9	-58.9	-65.3	-54.4	-53.1	-60.5	-56.4	-56.0	-75.1
2	**-17.4**	**0**	**-19.8**	-44.2	-48.9	-48.7	-60.0	-56.0	-65.3	-58.9	-64.2	-70.5	-70.2	-62.9	-70.4
3	**-16.0**	**-19.7**	**0**	-44.5	-47.4	-53.3	-67.8	-65.9	-69.9	-58.7	-55.1	-71.3	-61.1	-69.6	-71.2
4	-30.7	-43.6	-44.2	**0**	**-18.1**	**-15.6**	-46.1	-50.9	-58.8	-36.7	-42.6	-52.1	-54.6	-51.3	-53.7
5	-47.3	-49.3	-48.7	**-18.6**	**0**	**-23.9**	-47.1	-52.9	-64.0	-35.3	-38.3	-48.4	-57.2	-58.0	-65.8
6	-35.0	-45.9	-41.3	**-15.5**	**-24.1**	**0**	-46.4	-54.8	-62.6	-41.2	-41.6	-52.8	-56.3	-60.3	-61.2
7	-48.6	-58.6	-55.2	-67.6	-51.6	-58.2	**0**	**-22.0**	**-21.3**	-56.2	-51.0	-60.5	-52.0	-44.9	-51.8
8	-48.5	-55.6	-60.0	-46.5	-48.9	-52.9	**-21.0**	**0**	**-22.6**	-47.0	-44.5	-51.0	-54.6	-49.4	-49.8
9	-52.1	-65.7	-62.8	-57.6	-59.5	-58.1	**-20.9**	**-22.9**	**0**	-50.3	-43.5	-53.3	-57.0	-54.4	-58.0
10	-56.8	-50.6	-61.8	-51.3	-64.2	-57.5	-56.6	-50.9	-66.2	**0**	**-20.9**	**-21.4**	-60.5	-68.1	-75.5
11	-46.7	-57.0	-51.4	-48.3	-53.1	-54.6	-50.8	-42.3	-64.2	**-21.6**	**0**	**-24.2**	-49.2	-59.1	-56.8
12	-62.1	-60.2	-67.2	-56.8	-56.3	-55.1	-52.3	-59.1	-60.7	**-21.1**	**-24.4**	**0**	-51.2	-48.8	-48.9
13	-57.5	-65.4	-70.0	-63.6	-58.6	-70.1	-38.9	-37.9	-63.8	-58.6	-44.7	-65.0	**0**	**-23.6**	**-18.2**
14	-59.8	-63.1	-73.7	-60.6	-60.1	-62.3	-41.1	-38.7	-59.5	-61.0	-47.2	-49.2	**-23.8**	**0**	**-17.2**
15	-63.7	-68.3	-59.5	-68.7	-61.4	-63.2	-52.0	-49.1	-61.3	-59.0	-55.6	-62.5	**-18.4**	**-17.2**	**0**

Table 4.2: Inductive coupling matrix without preamplifier decoupling. Intra-array coupling is filled with yellow and inter-array coupling is shown in white.

Intra-array inductive decoupling is on average 17.8 dB, 19.3 dB, 21.8 dB, 22.3 dB, and 19.7 dB for subarrays 1 to 5, respectively. Inter-array inductive decoupling was 55.6 dB on average. Although these results are excellent and should be sufficient for PI performance, low input impedance preamplifiers offered additional levels of decoupling.

4.3.3.2 Preamplifier Decoupling

As discussed in Section 2.3.2, both mutual inductance and the nonzero current flow on the primary coil contribute to coil coupling. Therefore, reducing the flow of current in the primary loop is a means to reduce coil coupling. Consider the ideal configuration in which a coil loop is connected to an amplifier with infinite input impedance (Figure 4-14). With this ideal configuration, current is unable to flow around the loop even though an emf is present and faithfully amplified by the preamplifier (40).

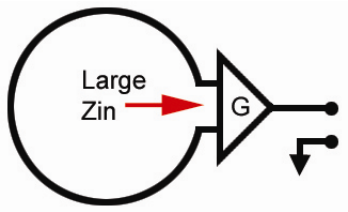

Figure 4-14: Ideal decoupling by current minimization permits an emf to be amplified without current flow

Amplifiers with high or low input impedance and a low noise figure can be designed and fabricated at MR frequencies. Using low-noise, low-input impedance preamplifiers for phased-array decoupling was first introduced by Roemer (40) using a matching network with a single degree of freedom and was later generalized by Reykowski to realize alternate matching networks if the required component values were impractical (86). The fundamental approach to preamplifier decoupling is shown in Figure 4-15.

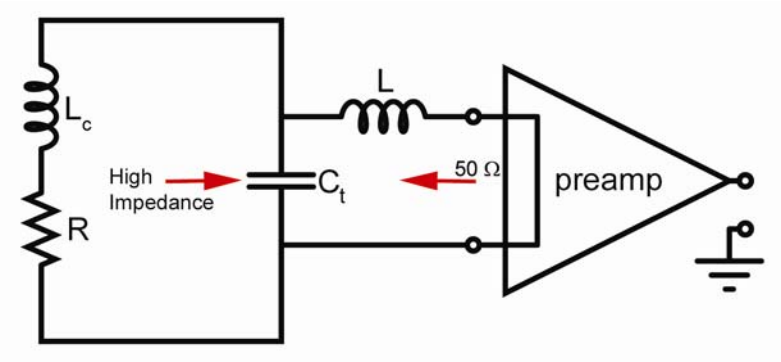

Figure 4-15: Low input impedance preamp decoupling reduces current flow around the coil

By optimal selection of L_c and L (which can be effective inductances that include a combination of reactive components) a 50 Ω match from the preamplifier perspective and current minimization from the coil loop perspective can be simultaneously achieved. The current minimization is a result of the high impedance produced by the parallel tank circuit made of C_t and L. This method is commonly used for decoupling non-adjacent elements of coil arrays. It is important to note that a coaxial cable transformation can also be used to rotate the preamplifier input impedance around the Smith Chart to synthetically generate L.

As concluded in Section 3.3.3, the ability to intrinsically decouple all three elements of the subarrays by overlap alone was a benefit of configuration V. However, to correct for imperfect overlaps and to improve SNR by placing the preamp in close proximity to the coil elements, preamp decoupling was also employed. Commercial low-input impedance preamplifiers (Microwave Technology Inc., Fremont, CA), that were modified to be unconditionally stable, were purchased for this project. The 15 modified preamplifiers had an input impedance Z_{in}= (4.6 ± 0.2) + (0.4 ± 0.2)j , a noise figure of 0.4 ± 0.03 dB, a gain G = 25.9 ± 0.6 dB, and an output match of -21.4 ± 2.2 dB.

To quantify preamplifier decoupling, S_{21} current profiles were alternatively measured with coils terminated to 50 Ω and terminated to preamplifiers. The minimum amount of current reduction was 11.6 dB for coil 5 and the maximum reduction was 15.9 dB for coil 7 (Figure 4-16). Average decoupling for all 15 preamplifiers was 13.5 dB.

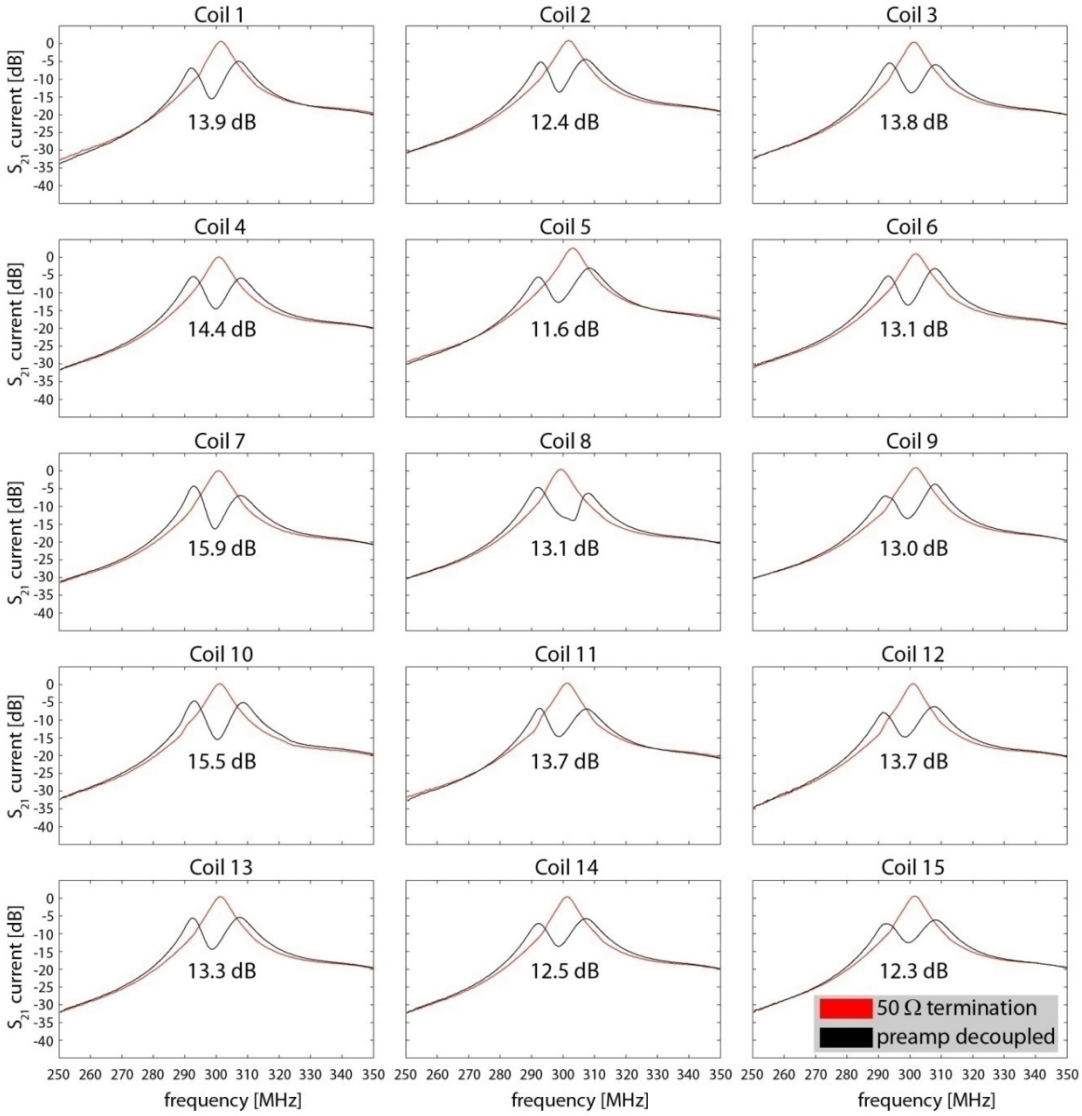

Figure 4-16: Preamplifier decoupling performance on 15 receive elements. Differences between the current profiles at 300 MHz determine the level of decoupling.

By incorporating preamp decoupling results with the inductive decoupling measurements of Table 4.2, total decoupling performance was estimated in Table 4.3. Because decoupling is dependent on current reduction from the primary coil, corresponding current decoupling was applied according to preamplifier results associated with the excitation port *y*.

S_{xy}[dB]	port *x*														
port *y*	*1*	*2*	*3*	*4*	*5*	*6*	*7*	*8*	*9*	*10*	*11*	*12*	*13*	*14*	*15*
1	**0**	**-31.5**	**-29.9**	-67.2	-72.5	-79.0	-72.8	-72.8	-79.2	-68.3	-67.0	-74.4	-70.3	-69.9	-89.0
2	**-29.8**	**0**	**-32.2**	-56.6	-61.3	-61.1	-72.4	-68.4	-77.7	-71.3	-76.6	-82.9	-82.6	-75.3	-82.8
3	**-29.8**	**-33.5**	**0**	-58.3	-61.2	-67.1	-81.6	-79.7	-83.7	-72.5	-68.9	-85.1	-74.9	-83.4	-85.0
4	-45.1	-58.0	-58.6	**0**	**-32.5**	**-30.0**	-60.5	-65.3	-73.2	-51.1	-57.0	-66.5	-69.0	-65.7	-68.1
5	-58.9	-60.9	-60.3	**-30.2**	**0**	**-35.5**	-58.7	-64.5	-75.6	-46.9	-49.9	-60.0	-68.8	-69.6	-77.4
6	-48.1	-59.0	-54.4	**-28.6**	**-37.2**	**0**	-59.5	-67.9	-75.7	-54.3	-54.7	-65.9	-69.4	-73.4	-74.3
7	-64.5	-74.5	-71.1	-83.5	-67.5	-74.1	**0**	**-37.9**	**-37.2**	-72.1	-66.9	-76.4	-67.9	-60.8	-67.7
8	-61.6	-68.7	-73.1	-59.6	-62.0	-66.0	**-34.1**	**0**	**-35.7**	-60.1	-57.6	-64.1	-67.7	-62.5	-62.9
9	-65.1	-78.7	-75.8	-70.6	-72.5	-71.1	**-33.9**	**-35.9**	**0**	-63.3	-56.5	-66.3	-70.0	-67.4	-71.0
10	-72.3	-66.1	-77.3	-66.8	-79.7	-73.0	-72.1	-66.4	-81.7	**0**	**-36.4**	**-36.9**	-76.0	-83.6	-91.0
11	-60.4	-70.7	-65.1	-62.0	-66.8	-68.3	-64.5	-56.0	-77.9	**-35.3**	**0**	**-37.9**	-62.9	-72.8	-70.5
12	-75.8	-73.9	-80.9	-70.5	-70.0	-68.8	-66.0	-72.8	-74.4	**-34.8**	**-38.1**	**0**	-64.9	-62.5	-62.6
13	-70.8	-78.7	-83.3	-76.9	-71.9	-83.4	-52.2	-51.2	-77.1	-71.9	-58.0	-78.3	**0**	**-36.9**	**-31.5**
14	-72.3	-75.6	-86.2	-73.1	-72.6	-74.8	-53.6	-51.2	-72.0	-73.5	-59.7	-61.7	**-36.3**	**0**	**-29.7**
15	-76.0	-80.6	-71.8	-81.0	-73.7	-75.5	-64.3	-61.4	-73.6	-71.3	-67.9	-74.8	**-30.7**	**-29.5**	**0**

Table 4.3: Inductive coupling matrix with preamplifier decoupling

From this data, decoupling performance as a function of average subarray performance for inter-array and intra-array decoupling are presented (Table 4.4).

S_{ij}[dB]	subarray *i*				
subarray *j*	*1*	*2*	*3*	*4*	*5*
1	**-31.1**	-64.9	-76.5	-74.1	-79.2
2	-55.9	**-32.3**	-66.8	-56.3	-70.6
3	-70.3	-69.7	**-35.8**	-64.8	-66.4
4	-71.4	-69.5	-70.2	**-36.6**	-71.9
5	-77.3	-74.4	-61.8	-68.6	**-32.4**

Table 4.4: Inductive decoupling for inter- and intra-subarray elements

Average intra-array decoupling is 33.6 dB, which is achieved through a combination of overlap and preamplifier decoupling. Average inter-array decoupling is 69.0 dB and indicates the benefit of using separate shielded volumes for multi-animal imaging along with low-input impedance preamplifiers.

Electric coupling was also investigated by calculating noise correlations (87). A spin echo acquisition (matrix = 642 × 340, bandwidth = 50 kHz) was acquired through all combinations of receive elements with the transmit power switched off. The noise covariance matrix **Ψ** was calculated by:

$$\Psi_{i,j} = cov(x_i, x_j) \equiv \langle (x_i - \mu_i)(x_j - \mu_j) \rangle \qquad (4-2)$$

and used to determine the noise correlation matrix as shown in Figure 4-17:

$$\Psi_{i,j}^{corr} = \frac{\Psi_{i,j}}{\sqrt{\Psi_{i,i} + \Psi_{j,j}}}. \qquad (4-3)$$

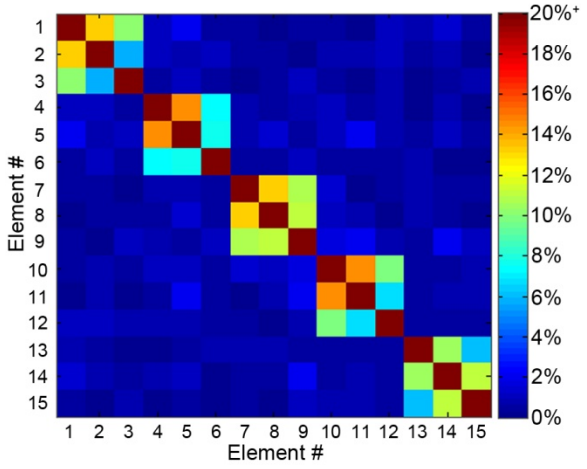

Figure 4-17: Noise correlation matrix between the 15 receive elements

Average noise correlation between intra-array elements was 10.2% while average inter-array element correlation was 0.68%.

4.3.3.3 Active Decoupling

So far, only strategies for decoupling receive array elements have been described. During the transmit phase of the acquisition, it necessary to detune receive coils to provide sufficient isolation from transmit coils for ensuring B_1^+ uniformity and protection of receive circuitry. Several strategies to accomplish this have been discussed in the literature (88,89). Passive decoupling involves placing crossed diodes on the receive coil that will be forward biased when a large transmit voltage is detected (90). This changes the distribution of tuning capacitance around the loop, and shifts the coil resonance away from the Larmor frequency. Passive decoupling is most easily tested on the MR scanner because of the transmit power requirements.

Actively decoupling coils, with PIN diode switches that are synchronized with the pulse sequence, is a common technique that is robust and easily analyzed in the laboratory. Therefore, active decoupling was employed for this multi-animal imaging system; however the placement diode traps was compared as shown in Figure 4-18.

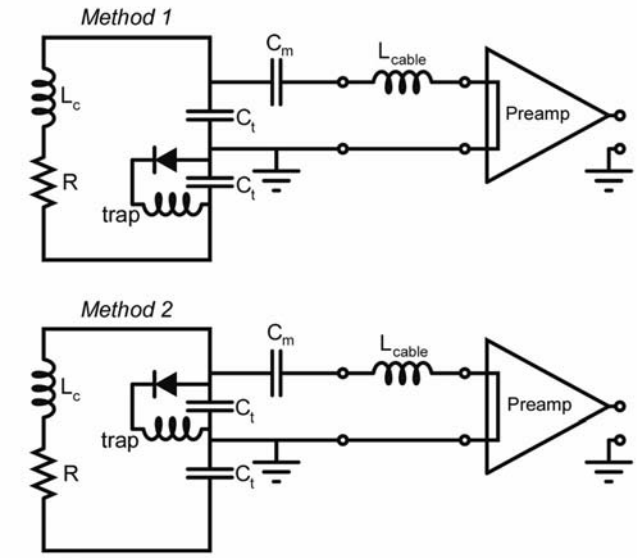

Figure 4-18: Receive coil active decoupling strategies with varying diode trap placement

In method 1 (Figure 4-18, top), the PIN diode trap was placed around a capacitor away from the tuning and matching circuitry. With method 2 (Figure 4-18, bottom), the PIN diode trap was placed across the tuning capacitor and in the signal path to the preamplifier. Surface coils with each of these active decoupling strategies were fabricated and tested. Current profiles were measured through independent probes with each of the PIN diodes in the reversed and forward biased states. As Figure 4-19 illustrates, an active trap placed around a capacitor placed on the loop, rather than along the signal path, resulted in superior decoupling performance of more than 45 dB compared to only about 20 dB. This was in part due to the ability to combine preamp and active PIN diode decoupling for method 1. With method 2, even though the parallel combination of the tuning capacitor and the actively-shorted diode trap form an open circuit, coupling to the resonance in the preamp decoupling circuit leads to additional modes that reduce the effectiveness of this approach. Based on these results, method 1 was selected and implemented on the multi-animal array system.

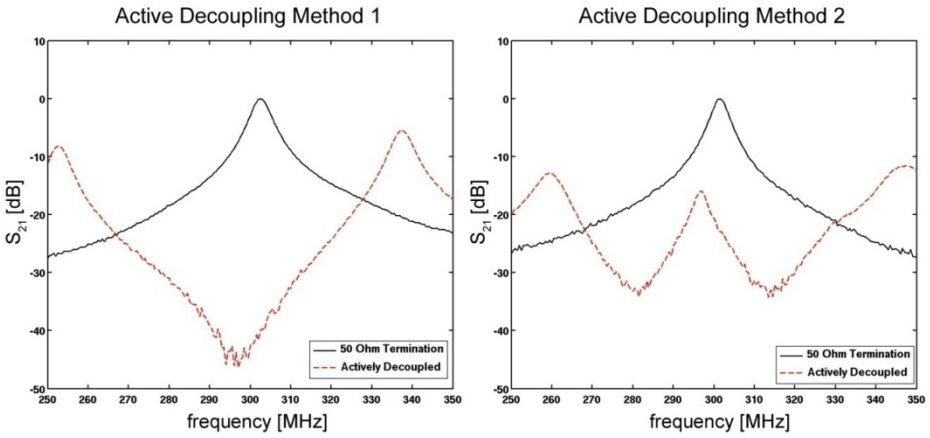

Figure 4-19: Current profiles comparing active decoupling strategies of the receive coils during the transmit phase

During the receive phase of the acquisition, the transmit coils must be detuned so that the sensitivities of the receive coils (the B_1^- fields) are unaffected by the transmit coils. The Bruker system provides an active decoupling signal capable of forward biasing PIN diodes during transmit and opening the diodes (by reverse biasing) during the receive phase. This strategy makes it easy to incorporate decoupling diodes into the transmit birdcage rungs (89). When forward biased, the rungs can conduct, and when reverse biased, the rungs are open and the coil does not resonate at the Larmor frequency. Unfortunately, such a strategy leads to higher coil losses. To instead forward bias diodes during receive and to reverse bias diodes during transmit; supplementary diode driving circuitry was developed.

The transmit driver included three stages. The first stage was a voltage divider to reduce the amplitude of the decoupling signal that is intended to drive a diode rather than act as a digital control signal. The second stage inverted the signal to digital levels of -15 V or +5 V minus the collector-emitter voltage. The final stage consisted of a push-pull transistor pair whose output follows the input received from the inversion stage, but with high current driving capability. This was required because the standard Bruker hardware was not designed to source the current required for driving many coils simultaneously.

The receive driver was almost identical to the transmit driver. However, receive does not require an inverted signal. Therefore, the inversion stage was replaced with two inversion stages that were cascaded to produce a digital buffer. Ground loops were minimized by isolating connections on the board so that the filter panel provided a single reference ground. A circuit schematic of the diode driving hardware with associated diode loads for the five coil assemblies is shown in Figure 4-20 and a photograph of the hardware is shown in Figure 4-21.

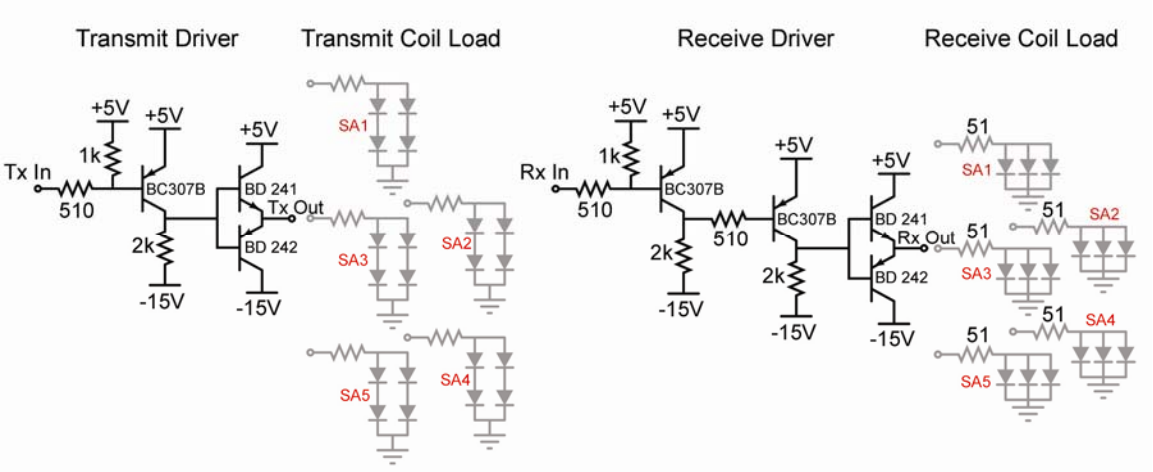

Figure 4-20: Schematic of diode driving circuitry and associated diode loads

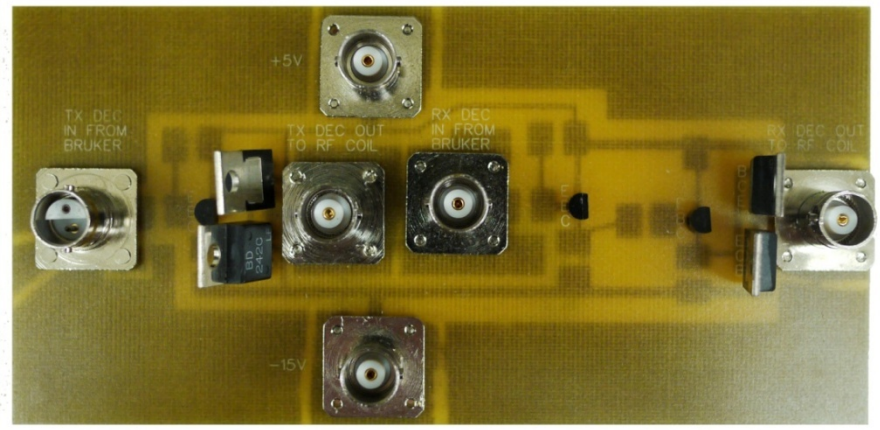

Figure 4-21: Photograph of a top view of the diode driving hardware

During the transmit phase, the diodes in the transmit coil decoupling circuit shown in Figure 4-2 are reverse-biased. Therefore, the impedance produced by the series combination of L_{trap} and the reversed biased diode is equivalent to an open circuit and has no effect on the coil Q. During the receive phase, active decoupling is accomplished with a +4.6 V signal which forward biases the transmit coil diodes. Three of these diodes within each transmit coil are contained in diode traps (Figure 4-2). The short circuit

produced by the diode creates a parallel resonance (with the 16 pF capacitor and L_{trap}) in three end ring segments. This alters the resonance of the homogeneous birdcage mode (Figure 4-22) and allows the receive subarrays to operate uncoupled from the transmit coils.

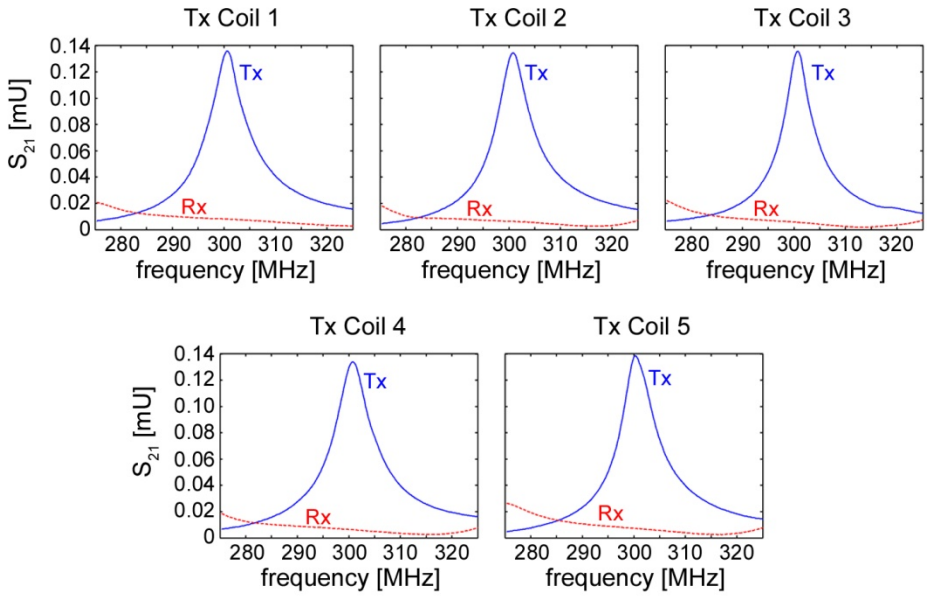

Figure 4-22: Active decoupling of transmit coils as measured through decoupled loop probes in the receive (red) and transmit phase (blue) of the acquisition. During the transmit phase, the birdcage resonators are faithfully resonating near the Larmor frequency. The resonance mode is eliminated when the active decoupling circuitry senses the receive phase of the sequence.

Active decoupling performance during the transmit phase was evaluated (Figure 4-23). PIN diode traps permitted dramatic current reductions for all receive array elements. Decoupling ranged from 36.6 dB to 41.0 dB, with an average value of 38.8 dB. As such, it is expected that transmit coils will be largely unaffected by the presence of the receive subarrays.

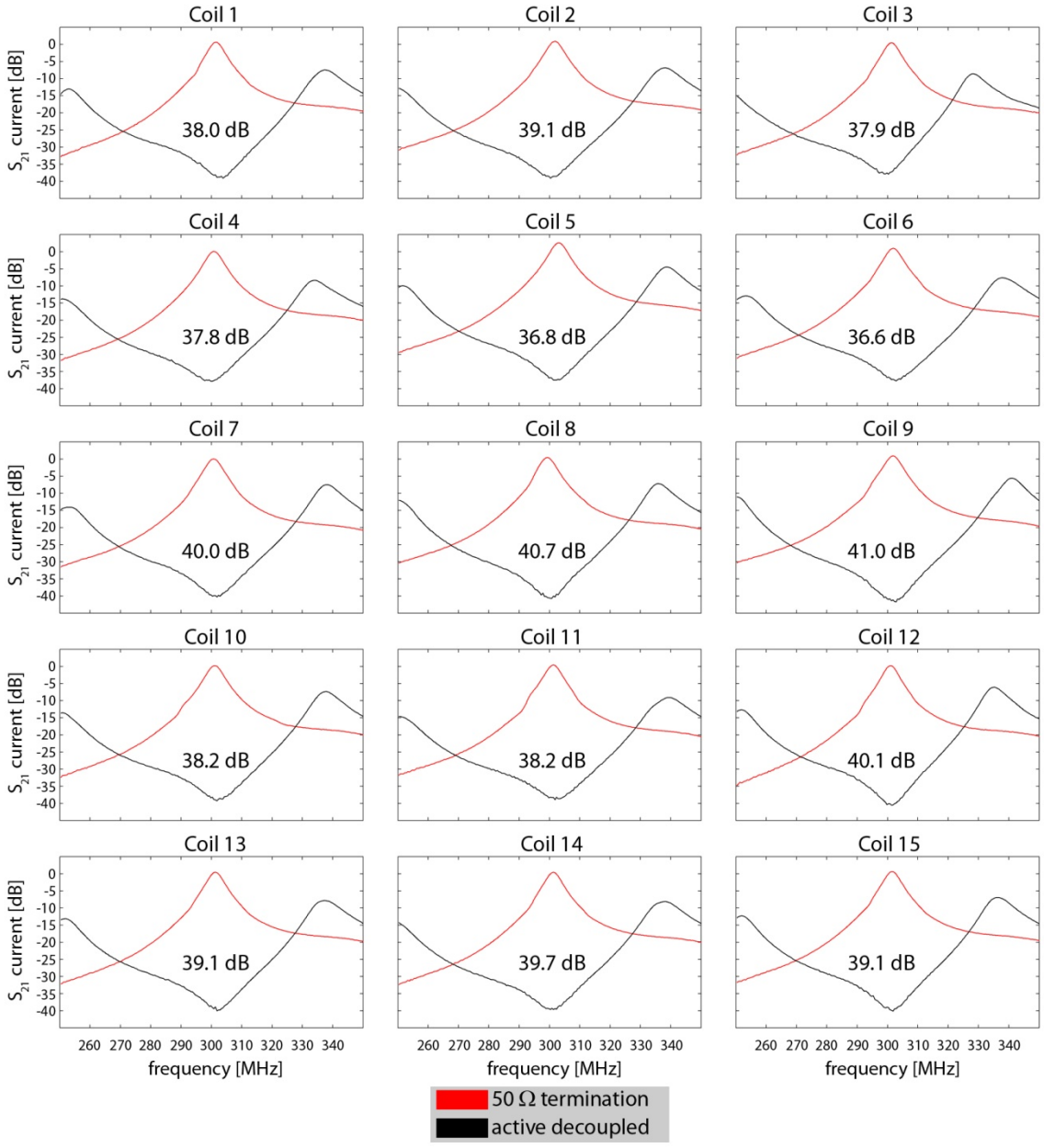

Figure 4-23: Active decoupling of receive elements during the transmit phase as measured by S_{21} current differences

4.3.4 Multi-Animal Encoding Scheme

To account for the staggered imaging volumes imposed by gradient space limitations, a multi-animal encoding strategy that changes the RO frequency of the receive channel with respect to the position of the associated imaging volume along the RO direction, was employed. The encoding scheme is more readily understood with the aid of Figure 4-24. Instead of applying PI-acceleration to a large multi-mouse FOV with $F = 5$ (Figure 4-24 left), all mice can be simultaneously encoded with a FOV appropriate for a single mouse with $F = 1$ (Figure 4-24 right). The prescribed axial FOV, with PE along the L-R direction, will encode mice 1 and 5 by aliasing since they have the same position along the RO direction. FOV replicates where mice 2 and 4 would be without space limitations can be frequency-shifted along RO to account for the spatial offset.

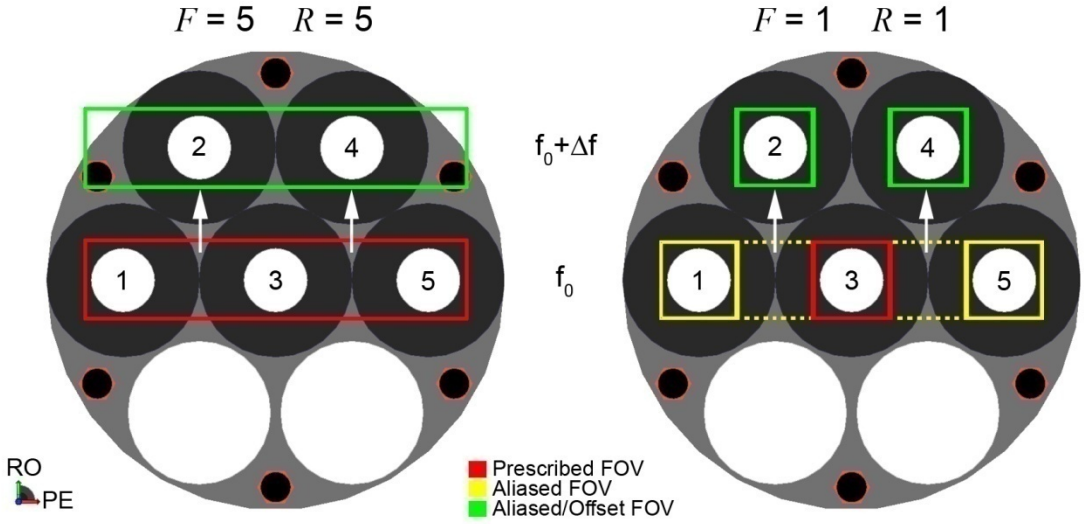

Figure 4-24: Efficient 2D multi-animal acquisition strategies can either be with a large multi-animal FOV (left) or a single-animal FOV (right)

Unaccelerated acquisition time (with $R = 1$ and $F = 1$) will be proportional to the number of PE steps required to encode a single mouse and independent of the number of mice

scanned at once. PI encoding (with $R > 1$) can be prescribed according to one mouse and will accelerate all simultaneously-encoded mice to dramatically improve throughput.

4.3.5 Imaging Performance

To evaluate imaging performance without the influence of coil position, each subarray module was sequentially placed in the center of the multicoil holder (position 3 in Figure 4-9) and axial spin echo images (FOV = 3.0 × 3.0 cm, matrix = 128 × 128, TE/TR = 15/500 ms, 18 1-mm slices) of a common loading phantom were acquired. The acquisitions were repeated with the transmitter turned off to acquire noise-only images that were used to perform optimally-combined image reconstructions (40). Resulting individual coil and combined images are shown in Figure 4-25.

The SNR of all image pixels was calculated as (91):

$$SNR = \sqrt{\frac{\boldsymbol{w}^H \boldsymbol{b}\boldsymbol{b}^H \boldsymbol{w}}{0.5\boldsymbol{w}^H \boldsymbol{\Psi} \boldsymbol{w}}}\ , \qquad (4-4)$$

where $\boldsymbol{\Psi}$ is the noise covariance matrix, $\boldsymbol{b}$ is a matrix of complex coil sensitivities, and $\boldsymbol{w}$ contains the coil weighting coefficients given by:

$$\boldsymbol{w} = \frac{\boldsymbol{\Psi}^{-1}\boldsymbol{b}}{\boldsymbol{b}^T \boldsymbol{\Psi}^{-1} \boldsymbol{b}^*}\ . \qquad (4-5)$$

When an individual coil rather than a coil-array is used for imaging, this formulation simplifies SNR to the mean pixel values divided by the standard deviation of pixels in the noise only image. SNR of individual coil images was calculated and plotted in Figure 4-26. SNR is relatively consistent between corresponding elements of the various subarrays. Additionally, the SNR maps indicate three unique sensitivity profiles for each subarray, confirming that there is minimal intra-array coupling. SNR-weighted image reconstructions (91) were performed to compare SNR performance between subarrays.

Results, as shown in Figure 4-27, indicate that the central SNR of each subarray is within 6% of all other subarrays. Thus, high-throughput image SNR will be consistent between all mouse imaging positions.

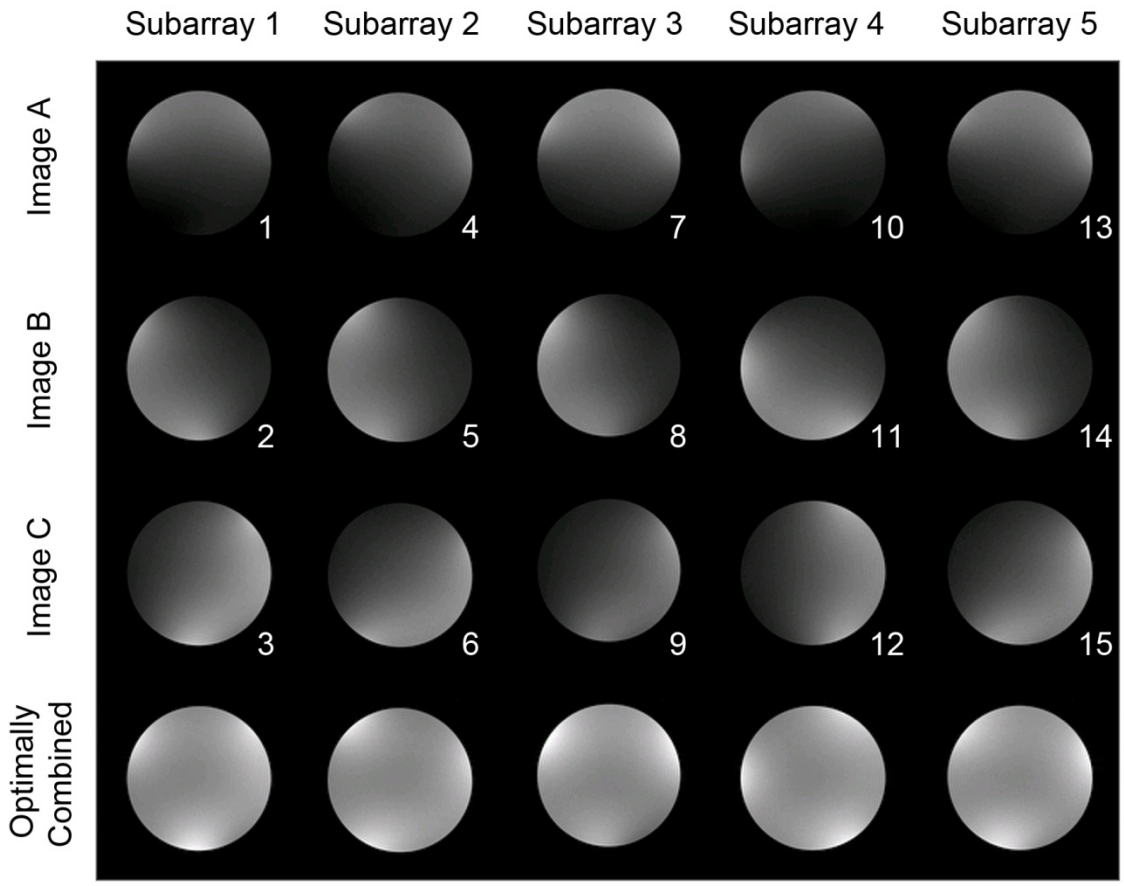

Figure 4-25: Individual coil (top three rows) and optimally-combined subarray images (bottom row)

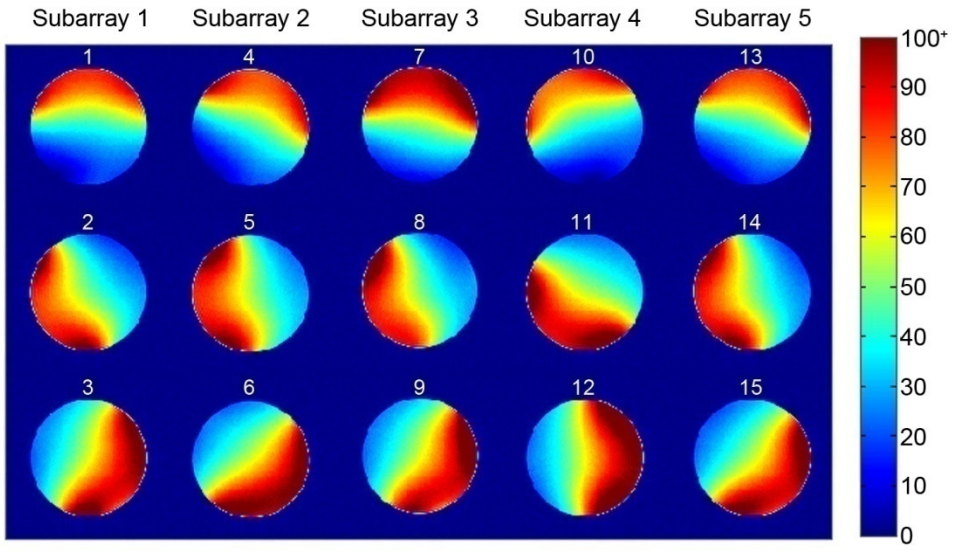

Figure 4-26: SNR maps of individual coil elements

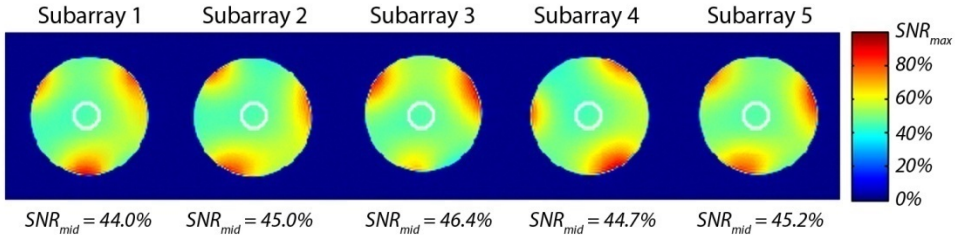

Figure 4-27: SNR maps for all five subarrays. The maps are normalize with respect to the highest SNR achieved over any phantom volume.

The SNR performance of a representative three-element subarray (placed in position 3) was compared against the standard 1P 8102 mouse birdcage coil. Spin echo phantom and noise images (FOV = 3.4 × 3.4 cm, $\text{matrix}_{\text{full}}$ = 256 × 256, TE_{eff}/TR = 15/500 ms, three 1.0-mm slices) were acquired through the two imaging configurations. For the subarray, both unaccelerated and PI-accelerated data sets were acquired, and a multiline, multicolumn GRAPPA algorithm (92) was used to reconstruct the accelerated data. A SENSE g-factor map (39) for $R = 2$ was generated from the fully-encoded array

data (Figure 4-28). The *g*-factor map is in close agreement with *g*-factor maps predicted by simulations of configuration V and $T = 9$, as shown in Figure 3-30. SNR maps were calculated using Equations $4-4$ and $4-5$ and are shown in Figure 4-29.

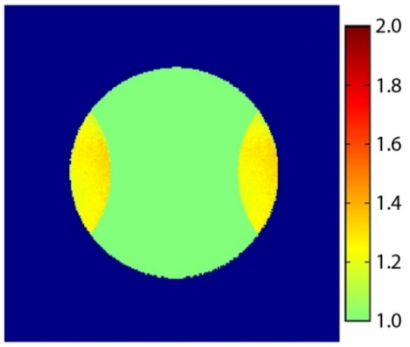

Figure 4-28: SENSE *g*-factor map for $R = 2$ as calculated from MSME data

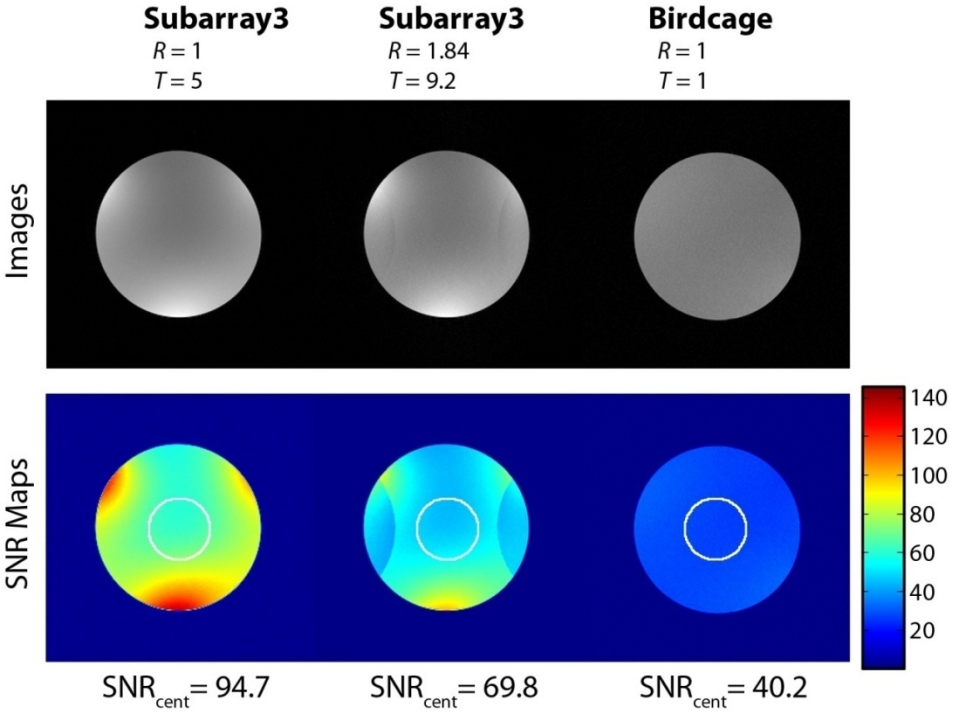

Figure 4-29: Images and SNR maps for various throughputs with the two coil configurations

Multi-animal-accelerated subarray acquisitions without PI (T = 5, R = 1, N = 5, F = 1) result in more than 2.3 times the SNR achieved with the birdcage coil (T = 1, R = 1, N = 1, F = 1) in the coil center (94.7 vs. 40.2) and even higher SNR in the coil periphery (Figure 4-29). The spatially dependent SNR loss from Figure 4-28 was applied to the unaccelerated subarray SNR map to calculate SNR expected from multianimal imaging with PI acceleration (T = 9.2, R_{eff} = 1.84, N = 5, F = 1) according to Equation $2-62$. Results shown in Figure 4-29 indicate that parallel imaging with the subarray maintains a central SNR improvement of 1.7 times compared to the mouse birdcage coil (69.8 vs. 40.2). Therefore, T = 5 can be used when highest SNR is desired or T = 9.2 can be used if the application permits trading SNR for improved imaging speed.

To investigate the impact of imaging in the gradient periphery, each of the five subarrays was placed in their final location within the multi-coil holder. Unaccelerated spin echo phantom images (FOV = 3.4 × 3.4 cm, matrix = 256 × 256, TE_{eff}/TR = 57/1000 ms, 1.0-mm slice) were acquired and combined using a root sum of squares approach (Figure 4-30). Geometric distortions over each phantom were calculated with respect to the height and width of the phantom when placed in the center coil holder position (h_{V3} and w_{V3}) according to the following equations:

$$distortion_{h,i} = \left|\frac{h_i - h_{V3}}{h_{V3}}\right| \times 100\% \qquad (4-6)$$

$$distortion_{w,i} = \left|\frac{w_i - w_{V3}}{w_{V3}}\right| \times 100\%, \qquad (4-7)$$

where i indexes the subarray number and $V3$ represents the central multi-coil holder position. Measurements were made to the nearest pixel that contained single, so partial volume effects were ignored.

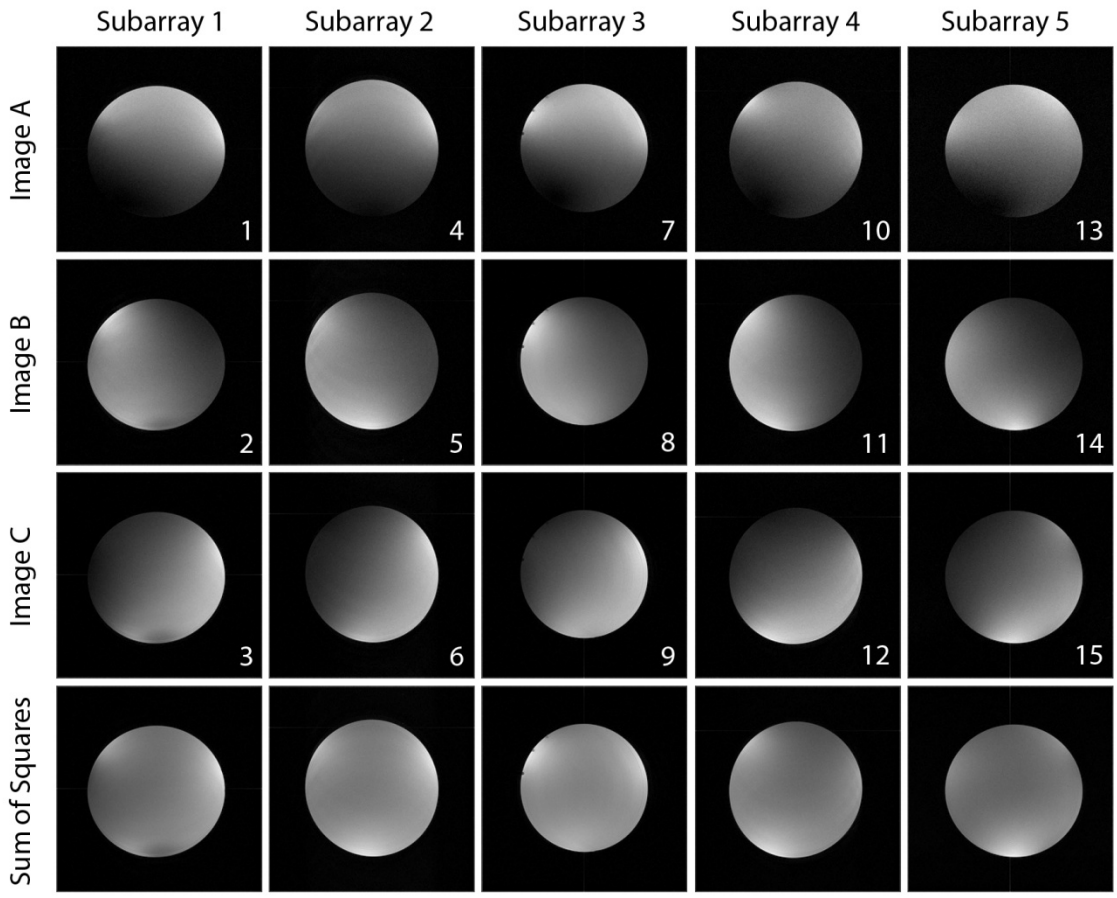

Figure 4-30: Individual coil images and sum of squares reconstructions from coils in the multi-coil holder

Phantom images acquired in the gradient periphery (i.e. subarrays 1, 2, 4, and 5) suffered from minor geometric distortions. Subarrays 1 to 5 had $distortion_h$ = 2%, 6%, 0%, 6%, and 3% and $distortion_w$ = 8%, 4%, 0%, 4%, and 8% respectively, indicating nearly symmetric gradient distortions about the *y* axis. The minor image distortions can be corrected prior to data analysis when accurate geometrical measurements, such as tumor volume calculations, are desired.

Chapter 5 - Multiple-Mouse DCE-MRI with MARCs

With the phased-array system in place and the performance validated on phantoms, *the final aim of this work is to develop a multi-mouse DCE-MRI protocol to test and evaluate the accelerated acquisition of mouse images and determine the throughput improvement compared to the conventional single-mouse approach with standard imaging hardware.*

5.1 Overview of DCE-MRI Protocol

A complete DCE-MRI protocol may consist of 8 total acquisitions (as listed in Table 5.1), allowing multiple views of anatomy along with acquisitions for quantitative functional imaging. Scans 1, 2, and 3 are used to ensure proper mouse positioning, setup adjustments, and reference views for subsequent slice placement. Scans 4, 5, and 8 offer T_2- and T_1-weighted anatomical views of the target anatomy. Scan 6 is used for determining the spatial distribution of tumor T_1 values, and scan 7 is a 10 minute DCE-MRI acquisition that is analyzed using one of several kinetic models. During this scan, a blood pool agent (BPA) is injected after two minutes of baseline acquisition, and a low-molecular weight interstitial agent (IA) is injected four minutes after the BPA.

Scan Description	Scan 1 Position 2D		Scan 2 TriPilot		Scan 3 Scout		Scan 4 Precontrast T2		Scan 5 Precontrast T1		Scan 6 T1 Map		Scan 7 Dynamic		Scan 8 Postcontrast T1	
Configuration	Single	Multi	Single	Multi	Single	Multi	Single	Multi	Single	Multi	Single	Multi	Single	Multi	Single	Multi
Slice Orientation	Coronal		Ax/Sag/Cor	Ax/Cor/Cor	Coronal		Axial		Axial		Axial		Axial		Axial	
Image Weighting	Proton Density		Proton Density		T2-Weighted		T2-Weighted		T1-Weighted		T1-Weighted		T1-Weighted		T1-Weighted	
Pulse Sequence	FLASH		FLASH		RARE (factor = 8)		RARE		MSME		RAREVTR		FSPGR		MSME	
TE	4 ms		3 ms		42.4 ms		42.4 ms		15 ms		44 ms		2.5 ms	2.5 ms	15 ms	
TR	25 ms		100 ms		3500 ms		3500 ms		1000 ms		6250 ms to 500 ms		40 ms	160 ms	1000 ms	
FOV [cm]	10 × 3.5	20 × 10	4.5 × 4.5	18 × 18	3.42 × 3.42		3.42 × 3.42		3.42 × 3.42		3.42 × 3.42		3.42 × 3.42		3.42 × 3.42	
Matrix	128 × 64	256 × 128	64 × 64	256 × 256	256 × 256		256 × 256		256 × 256		128 × 128		128 × 128		256 × 256	
Slices	1× 3.5-cm	1× 10-cm	3× 2-mm		18× 1-mm		18× 1-mm		18× 1-mm		1× 1-mm		7× 1-mm		18× 1-mm	
Flip Angle	30°		30°		90° - 180°		90° - 180°		90° - 180°		90° - 180°		33°	60°	90° - 180°	
Bandwidth	80 kHz		64 kHz		80 kHz		80 kHz		50 kHz		80 kHz		80 kHz		50 kHz	
Acceleration Factor	R = 1		R = 1		R = 1	R = 2	R = 1	R = 2	R = 1	R = 2	R = 1	R = 2	R = 1	R = 2	R = 1	R = 2
Scan Time	1.6 s	3.2 s	6.4 s	25.6 s	1 min 52 s	59.5 s	1 min 52 s	59.5 s	4 min 16 s	2 min 19 s	3 min 24 s	1 min 42 s	9 min 54 s		4 min 16 s	2 min 19 s
Image Repetitions	1		1		1		1		1		1		116/5.12 s	53/11.2 s	1	
Gradient Duty Cycle [%]	2.5	8.0	3.9	22.2	13.4	96.6	13.5	99.0	8.3	58.7	4.9	27.0	18.9	98.2	8.3	58.7

Table 5.1: Acquisition parameters of the single- and multi-animal DCE-MRI protocols

5.2 PROTOCOL DEVELOPMENT

The selection of protocol scan parameters was influenced by matching the image contrast and resolution of the single-animal protocol, while being constrained by gradient limitations. A detailed description of the single- and multi-animal scans that formed the DCE-MRI protocols is given. For reference, all sequence parameters are listed in Table 5.1.

5.2.1 Scan 1: Position 2D

The first scan provides feedback for optimally positioning the target mouse anatomy within the RF coil. Because very rapid imaging is required, proton density-weighted fast low angle shot (FLASH) acquisitions were acquired, and the coronal slices were made thick enough to project the whole animal volumes onto a single slice. The very rapid acquisition times (< 4 s) eliminated the need to accelerate acquisitions with PI. As an initial procedure, scans 1 and 2 of the multi-animal acquisition were acquired with all birdcage coils operated in transmit-receive mode and combined with the Wilkinson power combiner, with the receive arrays detuned.

5.2.2 Scan 2: TriPilot

The TriPilot is a three-plane FLASH sequence used to localize the image volumes. The spatial resolution of the multi-animal acquisition is matched to that for single-animal imaging, which requires an increase in the imaging FOV, matrix size, and scan time. However, because scan time was < 13 s, PI was not used to accelerate the acquisition. Unlike the slice prescription for single-animal imaging, an axial and two coronal slices were prescribed to enable viewing of all five imaging volumes (Figure 5-1).

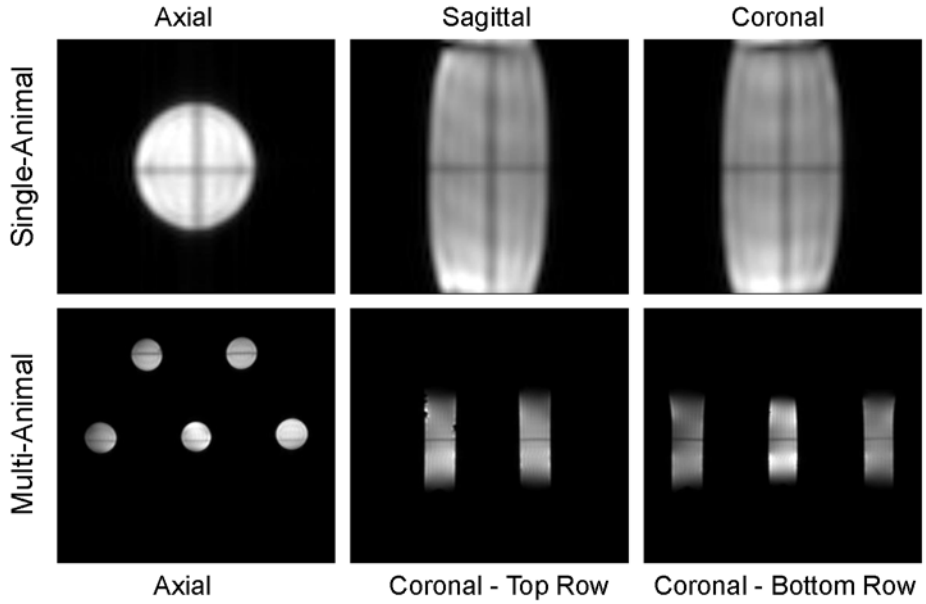

Figure 5-1: Single- and multi-animal TriPilot phantom images illustrate the different views for subsequent slice positioning

Just prior to the TriPilot acquisition, automatic setup routines that include multi-animal shimming, center frequency adjustment, transmit power calibration, and setup of the digitizer gain are executed. These setup routines are described in greater detail in Section 5.4.

5.2.3 Scan 3: T_2-Weighted Coronal Scout Imaging

For the remaining acquisitions, the single-animal and multi-animal slice prescription geometries are identical. The remaining multi-animal scans are acquired by transmitting through the birdcage volume coils and receiving through the subarrays. Parameters of the T_2-weighted coronal acquisitions are given in Table 5.1. The single-animal acquisition through the birdcage coil does not permit PI and requires a 1 min 52 s scan time. The multi-animal acquisition permits PI with $R = 2$ and eight additional ACS lines and results in a scan time of 59.5 s. The soft-tissue contrast offered by the T_2-

weighted scout images allows calculation of the required position adjustment to center the target imaging region (i.e. the tumor) along the *z*-axis. Representative phantom images acquired through both imaging configurations are shown in Figure 5-2. Note the inhomogeneous weighting by the multi-animal coil sensitivities, which leads to a reduced volume coverage and higher local SNR than the traditional single-animal birdcage coil.

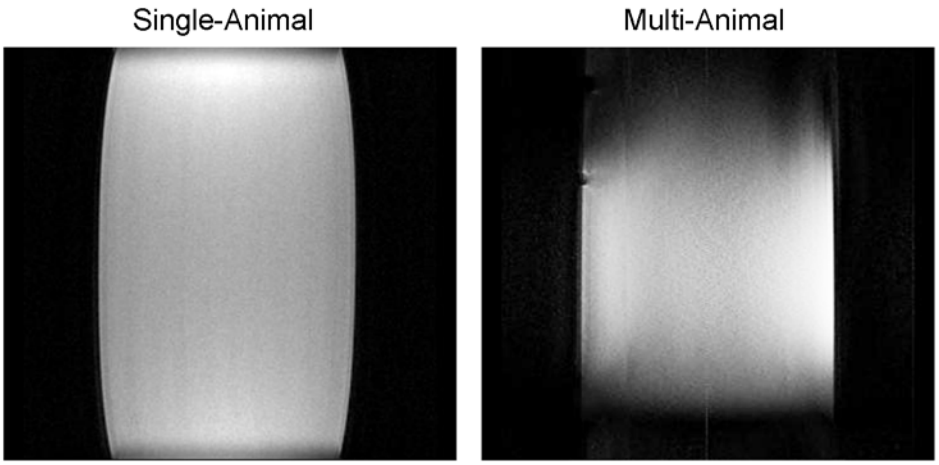

Figure 5-2: Single and multi-animal coronal scout images

5.2.4 Scan 4: Pre-Contrast T_2-Weighted Anatomical Imaging

The first anatomical axial images are T_2-weighted. Acquisition parameters of scan 4 (listed in Table 5.1) are identical to those for scan 3, with a change only in slice direction. A fixed set of 18 axial slices, that extends more than 2-cm along *z*, covers the entire sensitive region of the receive arrays. The single-animal acquisition takes 1 min 52 s and the multi-animal acquisition requires only 59.5 s to perform. Figure 5-3 shows representative images acquired through the single and multi-animal configurations.

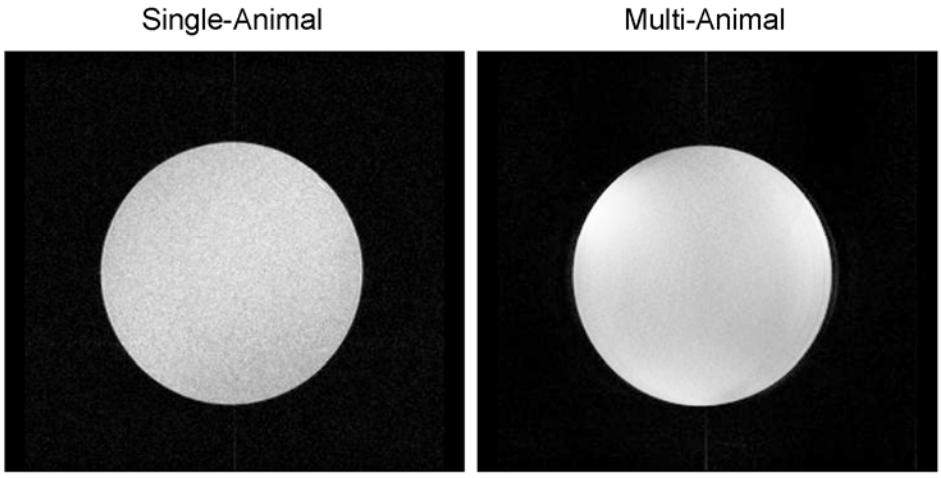

Figure 5-3: Single- and multi-animal T_2-weighted axial images

5.2.5 Scan 5: Pre-Contrast T_1-Weighted Imaging

The same axial slice geometry is then used to acquire T_1-weighted images prior to the injection of a T_1-reducing CA. A spin-echo acquisition (Table 5.1) was used for both imaging protocols. Unaccelerated single-animal scans took 4 min 16 s, while PI-accelerated (R = 2, 8 ACS lines) multi-animal scans took 2 min 19 s to acquire. Representative single and multi-animal phantom images are shown in Figure 5-4.

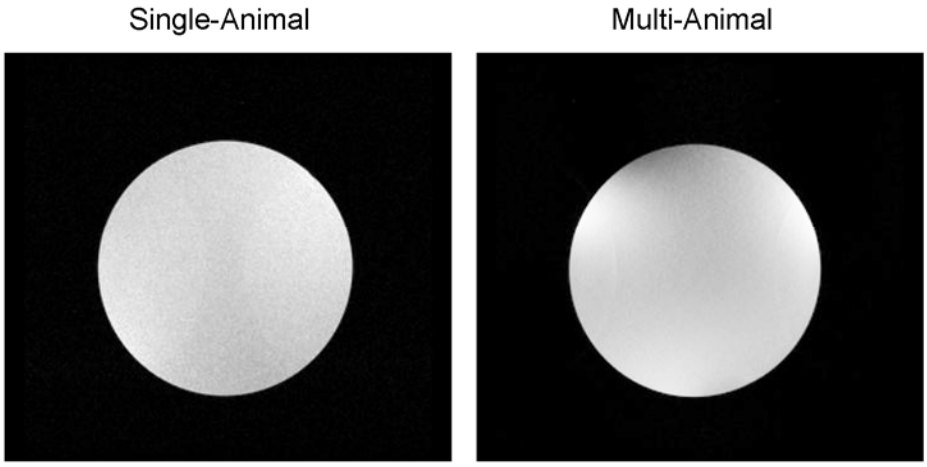

Figure 5-4: Single- and multi-animal T_1-weighted axial images

5.2.6 Scan 6: T_1 Mapping

A single slice saturation-recovery T_1-mapping sequence that uses a multi-echo rapid acquisition with refocused echoes (RARE) acquisition scheme and multiple TRs (TR = 6250 ms, 2462 ms, 1627 ms, 1130 ms, 776 ms, and 500 ms and other acquisition parameters in Table 5.1) is acquired for measuring the T_1 values of tumor tissue for subsequent PK analysis. Unaccelerated single-animal acquisitions take approximately 3 min 24 s, while PI-accelerated multi-animal acquisitions, with R = 2 and 8 ACS lines, take 1 min 42 s. Example single- and multi-animal acquisition phantom images are shown in Figure 5-5, where T_1 values were measured to be 387 ms ± 4 ms when using the birdcage coil and 381 ms ± 1 ms when using the multi-animal subarray. These measurements illustrate good agreement with less than a 2% difference between each configuration.

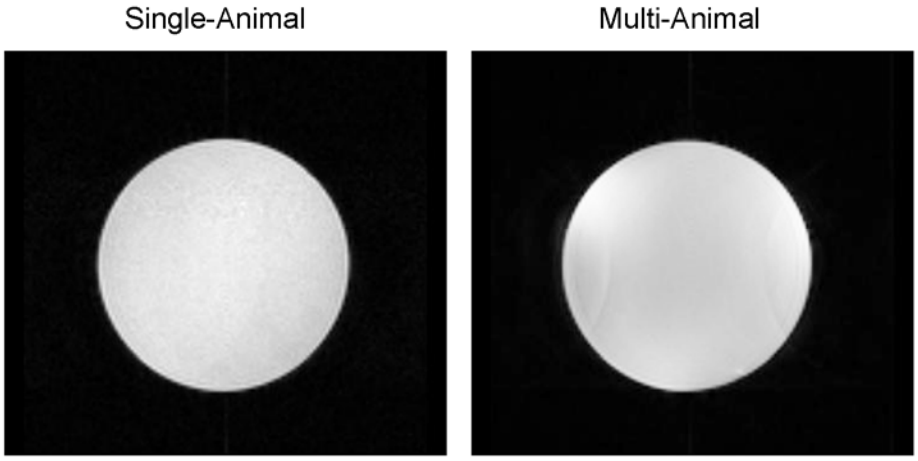

Figure 5-5: Single-and multi-animal RAREVTR images for T_1 calculation

5.2.7 Scan 7: Dynamic Contrast-Enhanced Acquisition

In this section, a dynamic acquisition that is fundamental to the DCE-MRI experiment is described. Before jumping into the acquisition parameters, it is important

to describe gradient constraints and management of the constraints related to this acquisition.

5.2.7.1 Gradient Limitations with Multi-Animal Imaging

A drawback of multi-animal imaging is that gradients large enough to accommodate several mice and the associated RF coils are used to encode a FOV and resolution appropriate for single-mouse imaging. Previous multi-animal imaging endeavors have relied on monitoring and managing the heat accumulated in the gradients during fast multi-animal acquisitions (52,61). Although protection interlocks were rarely tripped and no damage to the gradient coils was detected, the manufacturer now recommends operation at a specific duty cycle, with a safety margin that is conservative compared to existing interlocks. The latest release of console software (Paravision 5.1) offers a macro that simulates the pulse sequence and estimates the gradient duty cycle resulting from user-defined sequence parameters. The gradient duty cycle is then compared with the maximum gradient duty cycle that is suggested by the manufacturer ($duty\ cycle_{100\%}$).

The duty cycle, or gradient on-fraction f, is defined as the RMS power of the scan divided by the maximum continuous power that can be produced by the gradient amplifier:

$$f = \frac{power_{RMS,scan}}{power_{max,amp}} = \frac{{I_{RMS,scan}}^2 R_{grad\ coil}}{{I_{max,amp}}^2 R_{grad\ coil}} = \frac{{I_{RMS,scan}}^2}{{I_{max,amp}}^2}, \qquad (5-1)$$

where $R_{grad\ coil}$ is the resistance of the gradient coil. Because the BGA20 gradient coil allows a maximum continuous current of 45 A per channel and the gradient amplifier (Copley 265P) is capable of delivering 200 A per channel, $duty\ cycle_{100\%}$ corresponds

with a true gradient duty cycle of 5% if gradients are continuously-driven at maximum strength:

$$duty\ cycle_{100\%} = f_{max} = \frac{(45\ A)^2}{(200\ A)^2} = 0.05\ . \qquad (5-2)$$

Therefore, to keep the gradient load below that recommended by the manufacturer,

$$f_{scan} = \frac{{I_{RMS,scan}}^2}{(200\ A)^2} < duty\ cycle_{100\%} = 0.05 \qquad (5-3)$$

and

$$I_{RMS,scan} < \sqrt{0.05(200\ A)^2} = 45\ A \qquad (5-4)$$

per channel.

5.2.7.2 Protocol Optimization

The multi-animal scan optimization goal was to match the single-animal protocol as closely as possible, while ensuring that gradients were driven at less than $duty\ cycle_{100\%}$. To further verify the extent of gradient heating, a PTC100 temperature display was integrated into the system electronics and monitored during the acquisitions.

The dynamic fast spoiled gradient echo (FSPGR) acquisition requires enough slice coverage to allow visualization of the entire tumor with high spatial and temporal resolution, resulting in scan parameters that push the limits of the BGA20 gradient coil. Potential solutions to the gradient limitations include rapid imaging strategies such as PI, keyhole imaging (93,94), encoding reduction by spatiotemporal correlations (95), and adaptive sensitivity encoding (96,97). For this work, the gradient duty cycle was decreased and SNR increased by lengthening TR, and PI was employed to compensate for the dramatic reduction in temporal resolution.

The duty cycle macro was used for protocol optimization. Figure 5-6 plots the percentage of the recommended duty cycle as a function of the dynamic image update period, as calculated by the number of PE lines required for an image update multiplied by the TR. For seven axial slices and no PI, to keep the duty cycle below 100% $TR = 160$ ms and the image update time increases to 20.5 s. By incorporating PI-acceleration into the acquisition, an image update time of 11.2 s is achieved. A compromise in slices from seven to six only provided a reduction in image update period by ~1 s, so a seven-slice coverage was maintained.

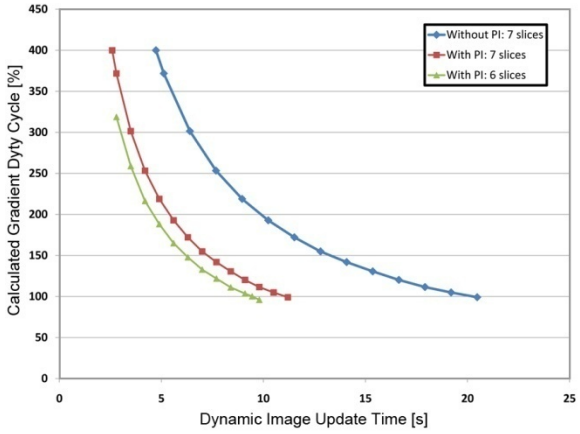

Figure 5-6: Dynamic FSPGR duty cycle calculations with and without parallel imaging

Figure 5-7 illustrates the output of the duty cycle macro for three repetitions, where the largest calculated duty cycle is just lower than $duty\ cycle_{100\%}$. The highest duty cycle occurs when encoding the edges of *k*-space. As suggested in Equation $2 - 47$, higher spatial frequencies in *k*-space require the most gradient strength.

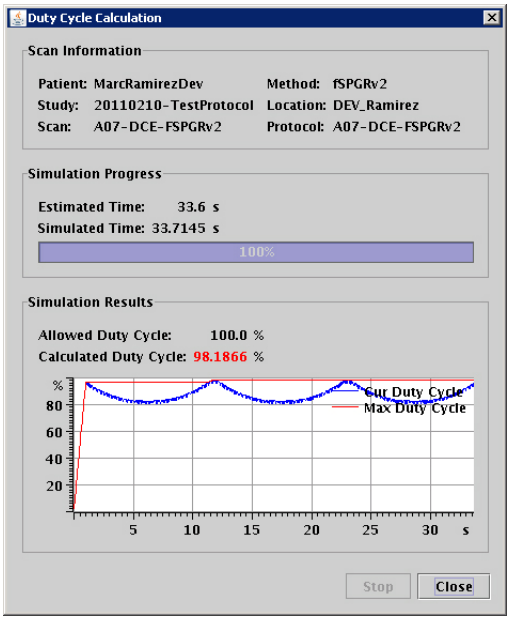

Figure 5-7: Screenshot of the duty cycle calculation for the multi-animal FSPGR scan

The single-animal dynamic acquisition with the birdcage coil allows use of a mouse-optimized gradient coil (BGA60) with a 60-mm ID. FSPGR acquisition parameters for both imaging configurations are listed in Table 5.1. The single-animal acquisition had a TE/TR = 2.5/40 ms, a 33° flip angle, 116 image repetitions, and a temporal resolution of 5.12 s, while the multi-animal acquisition had a TE/TR = 2.5/160 ms, a 60° flip angle, 53 image repetitions, and utilized PI (with $R = 2$ and 8 ACS lines) to achieve an 11.2 s temporal resolution. Representative phantom images are shown in Figure 5-8 from single and multi-animal acquisitions.

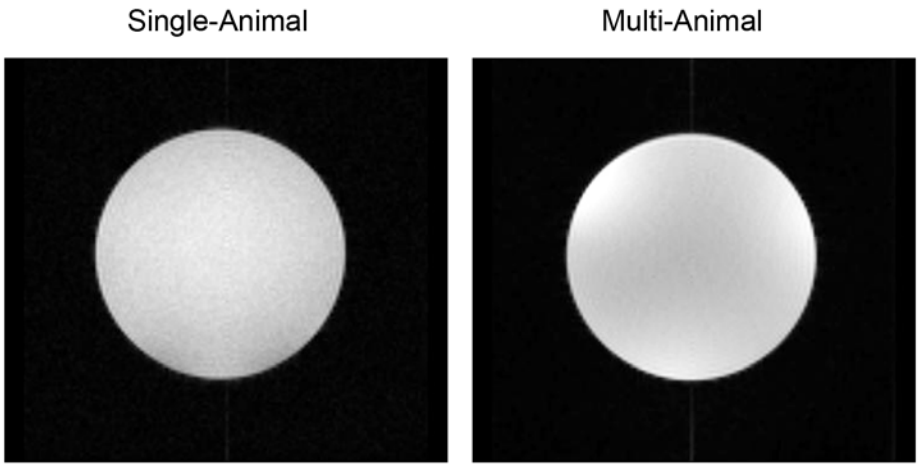

Figure 5-8: Single- and multi-animal dynamic FSPGR images

5.2.7.3 SNR of Single- vs. Multi-Animal DCE-MRI

The different TRs, flip angles, and encoding schemes between the single- and multi-animal FSPGR acquisitions all affect overall SNR. First, the effect of increasing the TR and flip angle α was tested. Ignoring T_2* effects, the steady-state signal equation, is given by (65):

$$S = \frac{\left(1 - e^{-\frac{TR}{T_1}}\right)\sin\alpha}{1 - \cos\alpha\ e^{-\frac{TR}{T_1}}}. \qquad (5-5)$$

Because all parameters related to noise are constant between these two measurements, SNR is proportional to S. Substituting the two sets of acquisition parameters into Equation $5-5$ predicts a two-fold SNR improvement for the multi-animal acquisition over the single-animal acquisition due to the sequence. To test this theory, the two FSPGR scans were sequentially-acquired on a common loading phantom and SNR maps were calculated according to Equations $4-4$ and $4-5$. Results indicate a SNR improvement of 1.94 times (Figure 5-9), which is in close agreement with theoretical predictions.

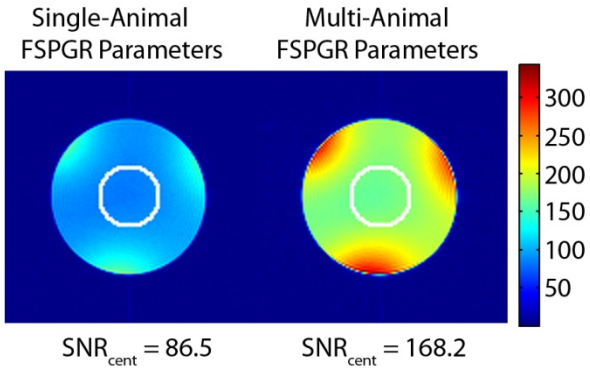

Figure 5-9: Effect of single- and multi-animal scan parameters on SNR

To test the effect of SNR due to the imaging configurations, scans with the multi-animal FSPGR acquisition parameters were acquired through both the birdcage coil and a representative subarray placed in the center (position 3). To quantify the achieved SNR, phantom and noise-only images were acquired and SNR maps were generated from Equations $4-4$ and $4-5$. Results indicate a two-fold SNR improvement by using the subarray rather than the birdcage coil (Figure 5-10).

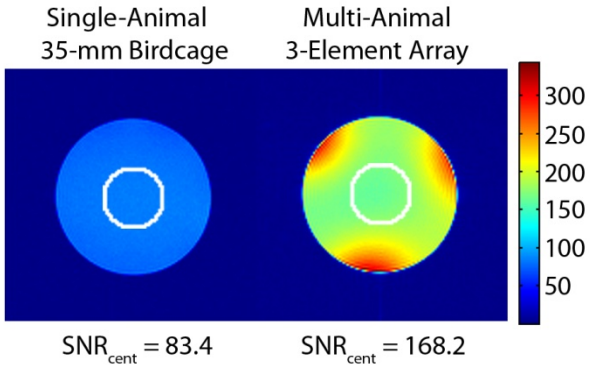

Figure 5-10: Influence of coil configuration on SNR

To estimate the SNR of the multi-animal DCE-MRI acquisition with parallel imaging, a SENSE *g*-factor map was calculated from the FSPGR acquisition (39). The

fully-encoded SNR map was then divided by the g-factor map and by $\sqrt{R_{eff} = 1.84}$ to compensate for reduction of acquisition time (Figure 5-11). In the phantom center, the overall reduction in SNR due to parallel imaging was 1.4 times.

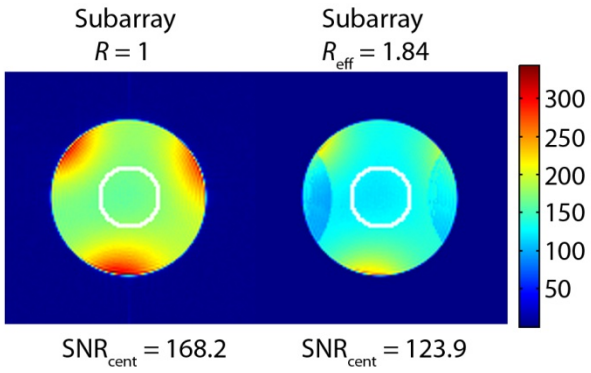

Figure 5-11: Effect of parallel imaging on the SNR of Scan 7

Neglecting effects due to sequence parameters, an SNR of 1.5 was gained, achieving the goal of high throughput without sacrificing image quality. Combining all SNR influences, an overall improvement of 2.9 is achieved with the multi-animal acquisitions compared to single-animal acquisitions, at the expense of temporal resolution.

5.2.8 Scan 8: Post-Contrast T_1-Weighted Imaging

A clone of the T_1-weighted axial scan, as described in Section 5.2.5, is the final acquisition of the image protocol. This gives a high-resolution visualization of the accumulation of CA in tissue which will appear brighter because of the T_1-reducing properties of the CA.

5.3 IMAGE RECONSTRUCTION

The choice between an image-based or a *k*-space-based approach to PI reconstruction is typically determined by a number of factors including patient/coil motion, the ability to accurately determine coil sensitivity maps via a low-resolution prescan, and the required acceleration or SNR. To avoid the complication of calculating sensitivity maps in regions lacking substantial signal, such as the lungs, GRAPPA was chosen. A multicolumn multiline GRAPPA reconstruction (92) was implemented in Matlab (code available in Appendix B) and incorporated into a Paravision macro (code available in Appendix C) for online PI reconstruction. For all but the dynamic images, GRAPPA coefficients are calculated on an image-by-image basis. To avoid potential intensity changes due to variation in the GRAPPA kernel coefficients rather than true CA intensity changes, a set of average coefficients was calculated based on the entire image series, and subsequently used to reconstruct the dynamic images.

5.4 PRESCAN SYSTEM ADJUSTMENTS

Commercial scanners have been optimized for single-animal imaging. Prior to imaging, a set of automatic adjustments are performed. In this section, the impact of multi-volume imaging on prescan system adjustments is investigated.

5.4.1 Transmit Power Calibration

For single-animal transmit calibration, the transmit power is iteratively adjusted and the signal is continuously-acquired until the transmit power level to produce a 90° flip angle is determined. All subsequent acquisition transmit levels are set with respect to the determined reference power level. With the multi-animal imaging system, the power from a single transmit channel is split between the five transmit volume coils. A one-time calibration is required to estimate the difference between insertion losses from the

Wilkinson power divider and the unequal tuning and loading. Discrepancies can be compensated for by adjusting RF attenuators in-line with each transmit coil. After calibration, transmit power can be automatically adjusted through a single transmit coil.

5.4.2 Receiver Gain

The receiver gain is an acquisition parameter that adjusts the dynamic range of the analog-to-digital converters (ADCs) that convert the output signal from the preamplifier into the digital domain for storage and processing. In the current release of Paravision, only one receiver gain can be set regardless of acquisition channels. However, to speed up acquisitions, the receiver gain can be predetermined based on the scan parameters and the coil configuration used. It is important to be conservative in setting the receiver gain as setting it too high (i.e. in an effort to maximize dynamic range) will clip the signal and cause saturation artifacts in the reconstruction.

5.4.3 Shimming and Center Frequency Adjustment

Multi-animal shimming and center frequency adjustment are not as straightforward and deserve substantial investigation. The B_0 field is unavoidably inhomogeneous due to magnet imperfections, the nearby presence of magnetic objects, or tissue interface boundaries. To correct for these inhomogeneities, shimming must be performed. For spectroscopy and spectroscopic imaging, shimming improves the ability to resolve concentrations of distinct molecular species. For imaging, shimming also improves image resolution and minimizes geometric warping artifacts caused by B_0 inhomogeneities and shading due to off-resonance effects. Passive shimming requires inserting and adjusting the position of steel shims to correct B-field inhomogeneities.

Due to the complexity involved, passive shimming is usually only performed during the installation of the MRI system.

Although global shimming is systematically performed on each individual animal for single-animal acquisitions, optimal shimming over multiple separate volumes remains an unresolved problem. The goal for multi-animal shimming is to reduce the variance in spin frequency distributions over each animal volume individually and over the entire multianimal volume. Good shimming performance over one mouse is of little benefit if it requires compromises for imaging other mice. To compare our ability to shim over five VOIs, linewidth measurements resulting from a point resolved spectroscopy (PRESS) acquisition that allow selective excitation over a user-defined VOI were performed. To achieve a large homogeneous sensitivity, birdcage coils were used in transceive mode with the receive subarrays actively decoupled.

One-cm^3 PRESS voxels were placed over each loading phantom in the location central to the receive subarray (Figure 5-12). A baseline gradient coil shim was initially loaded and three iterations of the Paravision global shim routine were sequentially executed on each of the five imaging volumes. This yielded results that represented the optimized single-volume shims. Next, all five birdcage coils were combined with the Wilkinson power combiner and the iterative shimming routine was repeated to produce a global shim from the combined signals. Finally, an average shim was calculated from the optimized individual shims (56). PRESS spectra were then sequentially acquired through each birdcage coil with the shims set to each of the five coil-optimized shims, the combined shim, and the average shim. Linewidths at 50% height (i.e. full width at half maximum or FWHM) of the magnitude spectra were used to compare shimming

performance, and the frequencies corresponding to the peak signal from each subvolume (using a weighted mean) were used to determine frequency differences.

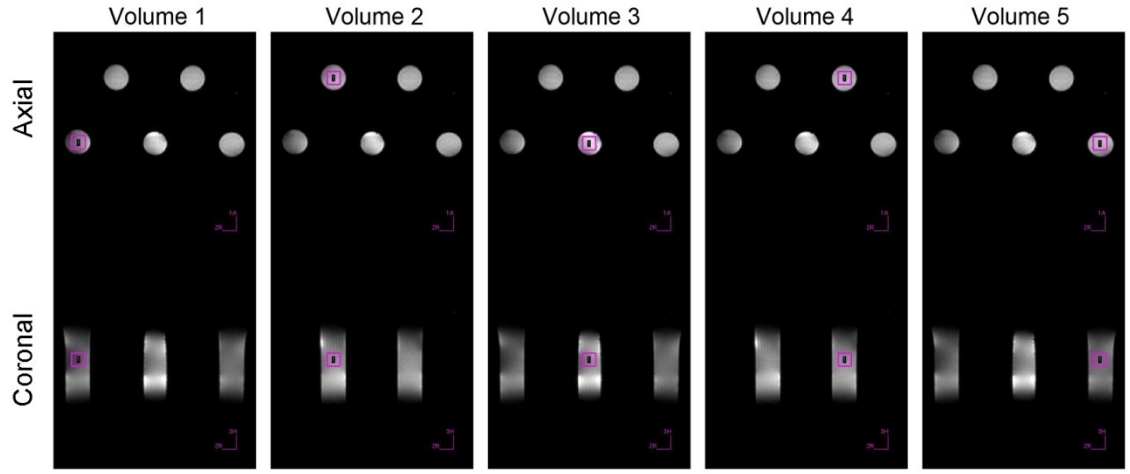

Figure 5-12: PRESS volumes prescribed over receive coil sensitivities used to investigate shimming methods

Figure 5-13 illustrates the resulting magnitude spectra acquired through each of the five volume resonators using these three methods. The resulting linewidth measurements correspond with the individual subarray B_0 homogeneity, and the maximum frequency spread between all volumes (Δf_{max}) corresponds with inter-array field homogeneity. Results listed in Table 5.1 (in blue) show that the best linewidths are achieved over the volume that the shims were optimized over. The best two results for each category shown in the three rightmost columns are highlighted in red. Although the average shim is not the best performer for any category, it is the second best for all categories, offering a reasonably balanced approach to optimization of linewidths and frequency distribution. Subject linewidths are all below 137 Hz and Δf_{max} = 168 Hz, both of which are lower than the lowest pixel bandwidth (195 Hz/pixel for scans 5 and 8) from all of the scans in this protocol. Thus, we do not expect a major compromise in

image resolution or geometric distortion due to B_0 inhomogeneity. The performance of the average shim is consistent with prior results using an alternate array geometry for scanning four animals at once using a 4.7T scanner (56). Ideally, the center frequency should be set to the average frequency of all imaging volumes. This can be calculated from a quick calibration scan prior to imaging on a particular day.

	Subject 1	Subject 2	Subject 3	Subject 4	Subject 5	Multi-subject		
	[Hz]	[Hz]	[Hz]	[Hz]	[Hz]	Avg [Hz]	Max [Hz]	Δf_{max} [Hz]
Volume 1 Shim	**29.4**	127.2	86.1	174.2	146.8	112.7	174.2	1,046.1
Volume 2 Shim	107.7	**35.2**	74.4	135.1	119.4	94.3	135.1	505.4
Volume 3 Shim	152.7	137.0	**33.3**	166.4	82.2	114.3	166.4	107.5
Volume 4 Shim	180.1	115.5	99.8	**33.3**	58.7	97.5	180.1	704.5
Volume 5 Shim	193.8	160.5	74.4	160.5	**29.4**	123.7	193.8	559.8
Combined Shim	119.4	88.1	50.9	162.5	115.5	107.3	162.5	363.0
Average Shim	137.0	80.3	43.1	129.2	92.0	96.3	137.0	167.9

Table 5.2: FWHM shim linewidths and peak frequency spread

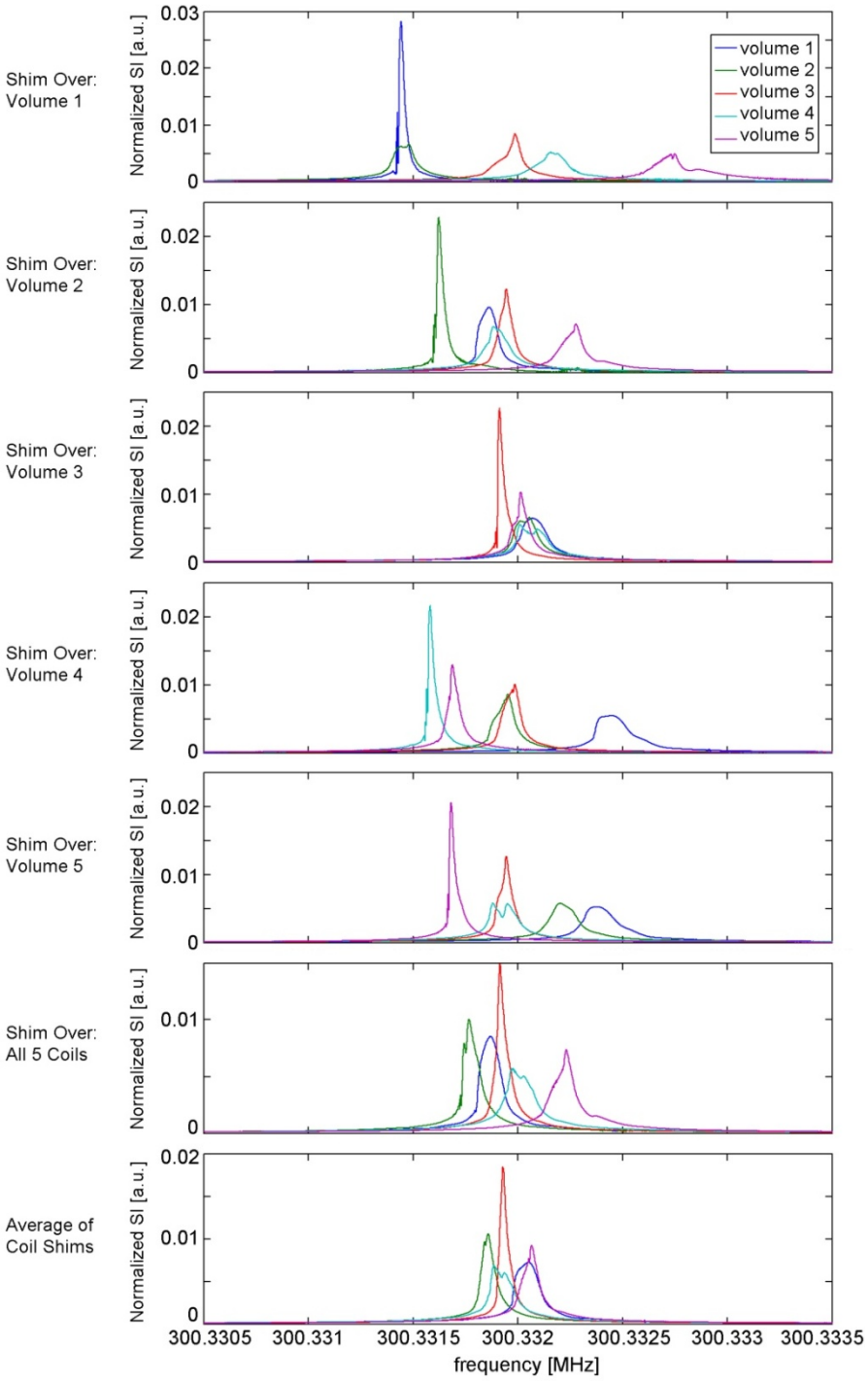

Figure 5-13: PRESS spectra acquired through the five volume coils. The spectra were normalized to all have an equal area under the curve.

5.5 MACROS FOR IMPROVED WORKFLOW

The manufacturer's software environment allows the use of macros, or short computer programs that are used to automate routine commands that can be time-consuming when manually executed by the user, to substantially improve protocol efficiency. For performing custom PI acquisitions, acquisition and reconstruction parameters must be set before each scan is initialized. Thus, macros for configuring these parameters, initializing PI acquisitions, calling Matlab reconstructions, and sending data to the display window were created for the anatomical and dynamic PI-accelerated acquisitions (Appendix C). These macros helped speed up the overall workflow for multi-animal acquisitions.

5.6 ANIMAL HARDWARE

As important as the multi-animal array system and protocol optimization are, *in vivo* animal imaging cannot take place without robust animal preparation, positioning, and maintenance hardware. Central to this requirement was the development of a five-mouse imaging sled that mated with the multi-animal array system. The sled incorporated channels for circulating warm water beneath all animals to maintain body temperature and channels for distributing anesthesia gas. Furthermore, the sled is compatible with the global rail positioning system that is on the scanner and allows for individual fine tuning of mouse positions along the main field axis. A photograph of the five-mouse sled is shown in Figure 5-14.

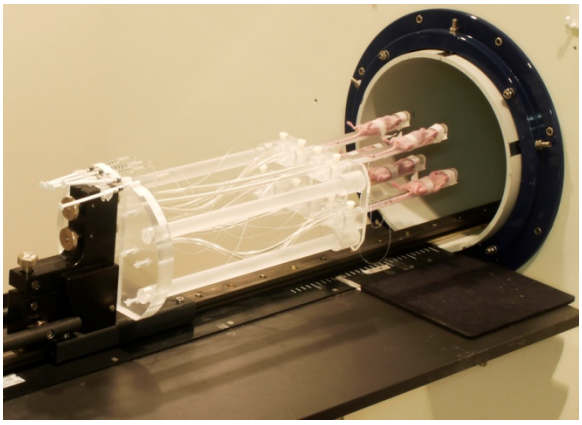

Figure 5-14: Five-mouse imaging sled

5.7 MOUSE IMAGING

Development of the imaging sled and the single- and multi-animal protocols on phantoms facilitated a smooth transition to *in vivo* mouse imaging. To compare single- and multi-animal imaging protocols, mice bearing human papillary thyroid tumors were scanned with the protocols described in Section 5.2. All animal procedures were approved by our Institutional Animal Care and Use Committee, which is accredited by the Association for the Assessment and Accreditation of Laboratory Animal Care International.

Three weeks prior to imaging, the right thyroid glands of 20 male athymic NCR-Nu/Nu nude mice were orthotopically injected with 5×10^5 BCPAP human papillary thyroid tumors cells (98). To investigate the effect of Vandetanib (ZD6474), a tyrosine kinase inhibitor that is an antagonist of the vascular endothelial growth factor receptor (VEGFR) and the epidermal growth factor receptor (EGFR) (99), half of the mice were treated with a combination ZD6474 and radiation therapy (XRT) either four, six, or eight days prior to MR imaging. Over the course of three imaging days, the mice were anesthetized and placed supine on either the multi-mouse sled or a single-mouse sled

distributing 2% isoflurane (IsoSol; VEDCO, St. Joseph, MO) in oxygen through nose cones. Respiratory bellows were placed on the abdomen of each mouse to monitor vital signs as an indicator or anesthetization status. The global position of all mice was adjusted along the *z*-axis and individually, more finely positioned after the T_2-weighted coronal images were acquired. Following the brief Position 2D and TriPilot acquisitions, the scans described in Sections 5.2.3 to 5.2.8 were acquired. The images shown in Figure 5-15 (bottom) were acquired with PI to accelerate the multi-animal protocol. For comparison, unaccelerated scans of a single animal were also acquired to give an indication of the image quality possible without using PI (Figure 5-15, top). Although the image quality is slightly reduced with PI, images are of high quality and consistent with results from phantom acquisitions that indicate higher SNR than can be achieved with the standard single-animal imaging hardware.

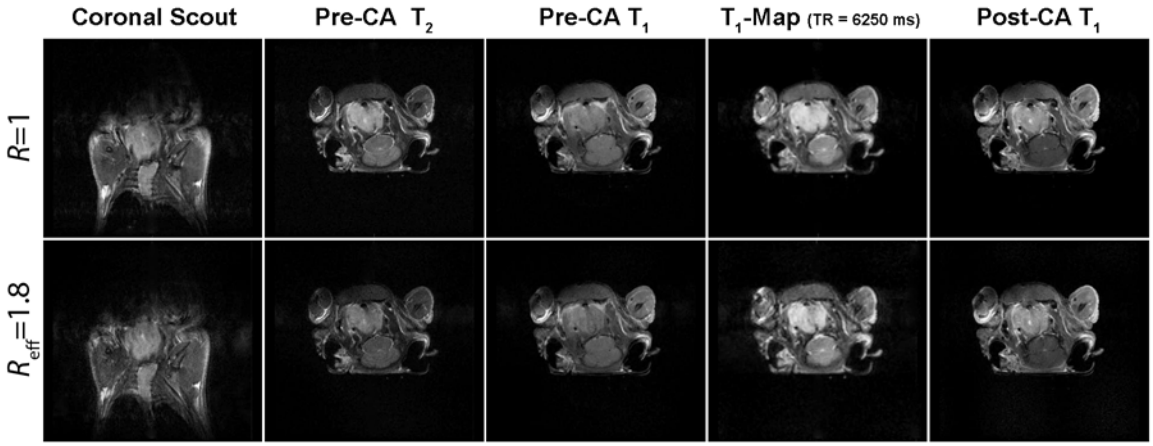

Figure 5-15: Comparison of unaccelerated (top row) and PI-accelerated (bottom row) anatomical mouse images from the DCE-MRI protocol

Although the hardware and protocol are ready for accelerated multi-animal imaging, only four receiver channels were available at the time of data collection. This required several imaging sessions to imitate data that can be simultaneously acquired

when 15 receive channels become available. Representative data from the two imaging configurations is displayed in Figure 5-16. Images from the multi-animal acquisitions show slightly less background noise than the single animal acquisitions. The mice scanned with the multi-mouse hardware were positioned with their arms extended above their head whereas the arms were kept by the animals' side for the single-animal acquisitions. This resulted in slightly different appearance between single- and multi-animal images.

Figure 5-16: Representative mages from multi- (left five columns) and a single-animal (right-most column) protocols

5.8 PHARMACOKINETIC ANALYSIS

Tofts' two-compartment model (22), derived from Kety's earlier work (100), has become the most predominantly used quantitative PK model. However, this method requires accurate estimation of the AIF. Even very rapid AIF sampling with traditional encoding schemes is often insufficient to sample the rapid kinetics of a mouse with a small blood volume and rapid cardiovascular cycle (101). Therefore, a dual-tracer approach, that eliminates the requirement for AIF estimation, has been employed for this and other multi-mouse DCE-MRI investigations (18,102). The first tracer is a vascular agent that cannot escape into the EES during the acquisition. This blood pool agent or BPA is typically composed of large molecular weight (> 500 kDa) particles and is injected after a series of baseline scans are acquired. The BPA relaxes the vascular component of the voxel signal (i.e. reduces the T_1 of the blood) so that signal changes after the injection of a lower molecular weight agent (< 1 kDa) are only due to the extravasation and accumulation of the agent in the EES due to vascular permeability. Semi-quantitative parameters correlating with the extravascular (v_e) and vascular (v_b) volumes can be calculated based on changes in signal intensities. Furthermore, parameters correlating with vascular permeability (and K^{Trans}) can be estimated from the maximum slope of signal intensities after injection of the low molecular weight agent (102). The dual-tracer DCE-MRI approach is summarized in Figure 5-17.

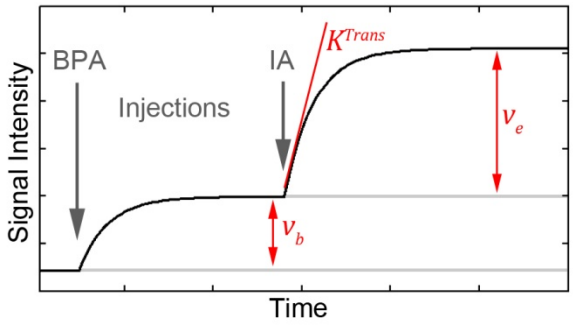

Figure 5-17: Analysis of dual-tracer DCE-MRI where signal intensity differences give an estimate of volume fractions and the slope fives an estimate of permeability

Although PK analysis in not an aim of this work, for the sake of completeness, example relative volume fraction and permeability maps were generated from five dynamic data sets that were acquired through each of the subarrays. Representative pixel uptake curves are plotted in Figure 5-18 along with baseline and exponential fits.

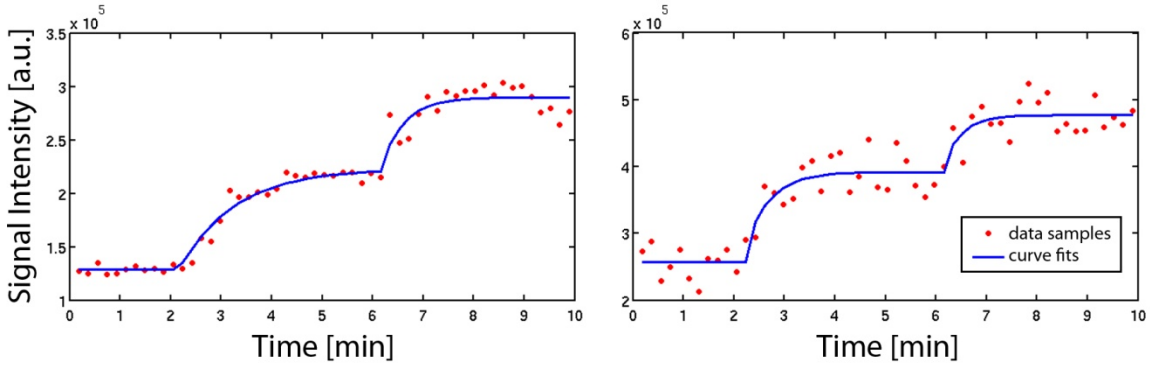

Figure 5-18: Representative measured uptake curves and associated fits

To allow relative parameter map comparison between different experiments, signal intensity curves were normalized to initial baseline values. Relative vascular and interstitial volume fractions (here denoted as rv_b and rv_e respectively), based on SI changes before and after BPA and IA injections (102) for the central tumor slice, are shown in shown in Figure 5-19 and Figure 5-20.

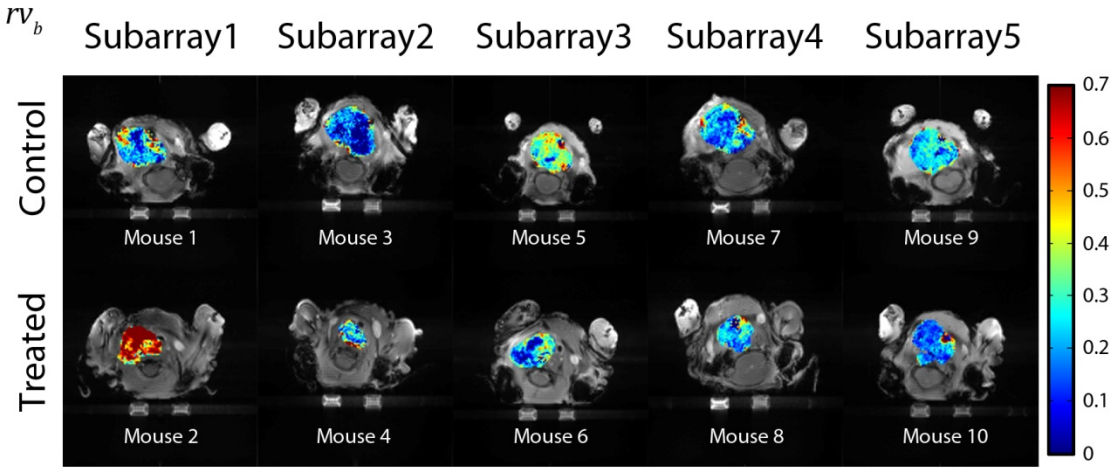

Figure 5-19: Relative blood volume tumor maps (rv_b) from treated and control groups that were acquired through all multi-animal subarray volumes.

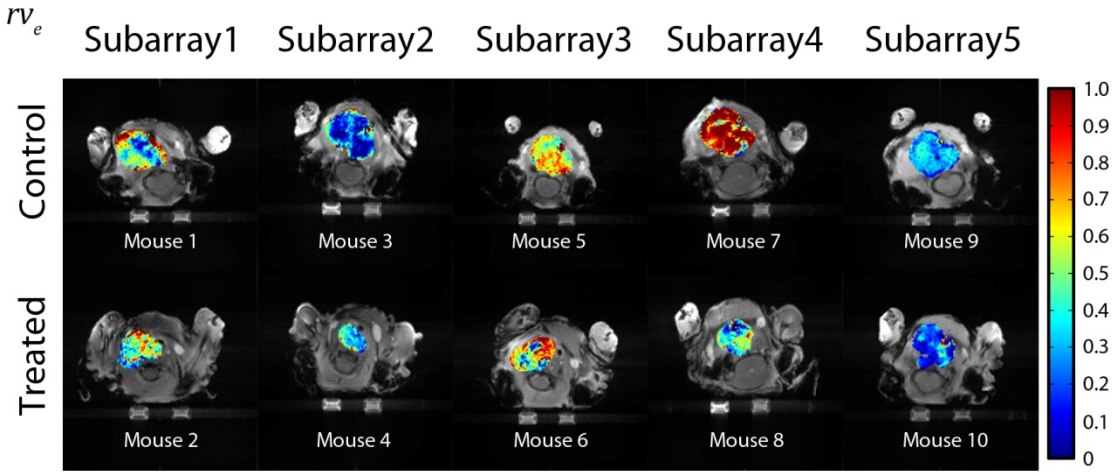

Figure 5-20: Maps of relative EES volume (rv_e)

Similarly, maps of relative estimates of permeability (rP) are shown in Figure 5-21.

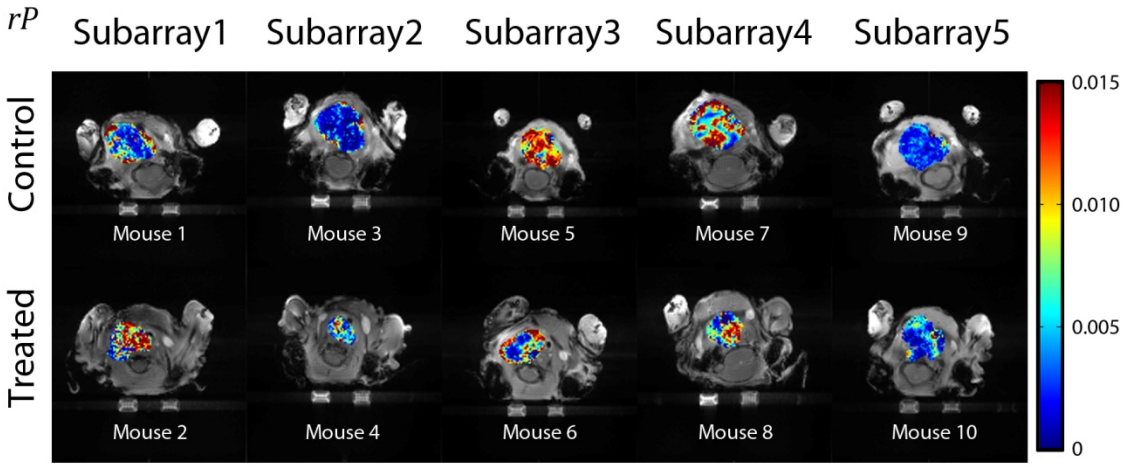

Figure 5-21: Maps of relative permeability (rP)

To test for a statistically significant difference between the resulting pharmacokinetic parameters between control and treated groups, the average values over the central tumor slice (excluding pixels containing necrotic tissue as identified by lack of signal enhancement) were analyzed. Data is plotted in Figure 5-22. Two-sided t-tests were performed to accept or reject the null hypothesis that the means of the two groups were the same. For all cases, the null hypothesis was accepted with p values of 0.39, 0.44, and 0.99 for rv_b, rv_e, and rP respectively. A previous investigation on the treatment of an anaplastic tyroid xenograft tumor showed a statistical difference in vascular volume fractions and vessel permeability (99). Although no statistically significant difference between groups was detected here, including more than five animals per group in future studies will increase statistical power.

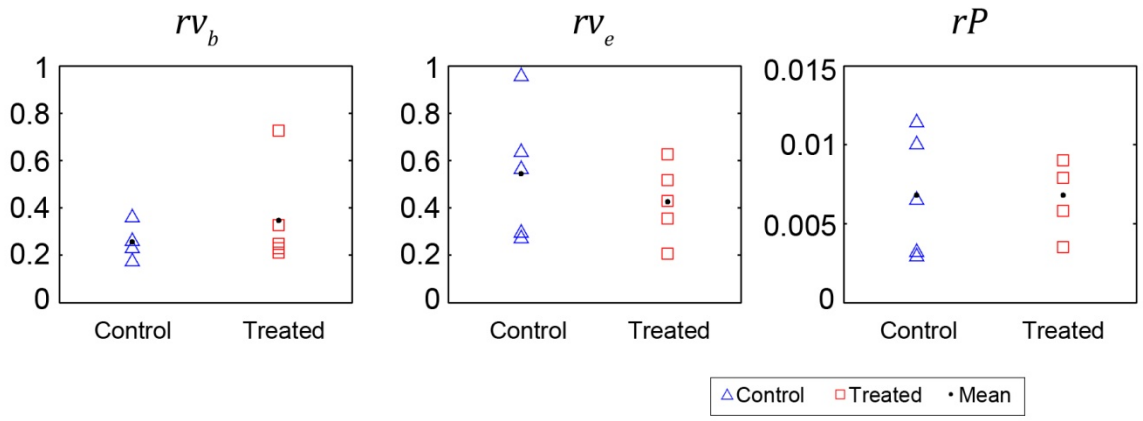

Figure 5-22: Mean PK results from two five-animal groups

5.9 THROUGHPUT ANALYSIS

Three multi-animal imaging protocols were executed through each of the subarrays and three single-animal imaging protocols were run through the standard mouse hardware. A single slice from each of the acquisitions is shown in Figure 5-23.

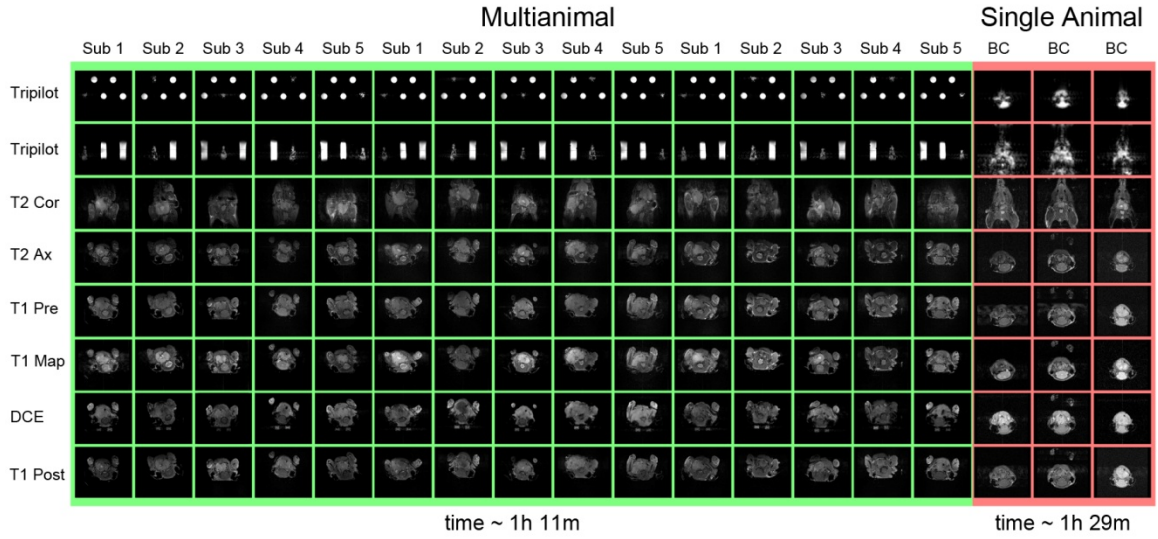

Figure 5-23: An image from each of the DCE-MRI protocol acquisitions

To quantify throughput improvement, each of the acquired imaging protocols was timed with a stop watch. The timing commenced with the execution of the first Position 2D scan and terminated when the post-contrast T_1-weighted acquisition was completed. Single-animal acquisitions through the birdcage coil took 29 min 27 s, 29 min 47 s, and 29 min 40 s. Multi-animal acquisitions took 24 min 46 s, 23 min 35 s, 23 min 43 s, 23 min 39 s, 23 min 30 s, 23 min 18 s, and 23 min 39 s (Table 5.3). On average, single-animal acquisitions took $\bar{x}_1$ = 29.63 min with sample variance ${s_1}^2$ = 0.03, while multi-animal acquisitions took $\bar{x}_2$ = 23.73 min with sample variance ${s_2}^2$ = 0.22.

A central hypothesis of this work was that a multi-mouse DCE-MRI protocol could improve throughput by more than N times (here N = 5) that of a single-animal protocol with conventional hardware. A throughput improvement greater than N can be expressed mathematically as:

$$\frac{Throughput_{multi}}{Throughput_{single}} > N = 5, \qquad (5-6)$$

where the throughputs is defined as:

$$Throughput_{multi} = \frac{N_{multi}}{time_{multi}} = \frac{5}{time_{multi}} \qquad (5-7)$$

$$Throughput_{single} = \frac{N_{single}}{time_{single}} = \frac{1}{time_{single}}\,. \qquad (5-8)$$

By algebra, the hypothesis can be expressed as:

$$5 \times time_{single} > 5 \times time_{multiple}\,, \qquad (5-9)$$

or simply:

$$time_{single} > time_{multiple}\,. \qquad (5-10)$$

The average timing measurements indicate a throughput improvement of 6.25 times, which is greater than *N*. However, to test for statistical significance ($p \leq 0.05$ considered significant), a two-sample *t* test for independent samples is required. An *F* test must first be performed to determine if the two populations have equal or unequal variance. The null hypothesis $H_0: {\sigma_1}^2 = {\sigma_2}^2$ is tested against the alternative hypothesis $H_1: {\sigma_1}^2 \neq {\sigma_2}^2$, where σ^2 represents the population variance. The test statistic was computed as:

$$F = \frac{{s_1}^2}{{s_2}^2} = 0.13, \qquad (5-11)$$

where the sample variances were determined directly from the timing measurements. Since $F < F_{2,6,0.975} = 7.26$, the null hypothesis cannot be rejected, so the variances are treated as equal.

For a two-sample *t* test for independent samples with equal variances, the null hypothesis $H_0: \mu_1 = \mu_2$ should be tested where:

$$H_0: time_{single} = time_{multiple} \ . \qquad (5-12)$$

Thus, the mean values can simply represent the single- or multi-animal protocol execution times. The test statistic was computed by:

$$t = \frac{\bar{x}_1 - \bar{x}_2}{s\sqrt{\frac{1}{n_1}+\frac{1}{n_2}}} = 20.40, \qquad (5-13)$$

where the sample standard deviation s:

$$s = \sqrt{[(n_1-1){s_1}^2 + (n_2-1){s_2}^2]/(n_1+n_2-2)} = 0.42\,. \qquad (5-14)$$

$t > t_{8,0.975}$, so as expected, the null hypothesis can be rejected (p = 6.7e-9) and results are statically significant. This work demonstrates, for the first time, an entire study

accelerated by more than the number of animals simultaneously scanned, and confirms the central hypothesis of this work.

Animal preparation times were also measured by our veterinary staff on two separate imaging days and the results are indicated in Table 5.4. An average time of 4 min is required to prepare one animal, so preparing five animals should roughly scale to 21 min or less since animals can be sedated in parallel. This leaves adequate time allowance for increases in the complexity to situate the five mice on the multi-animal sled. Based on preparation time and the accelerated imaging protocol, scanning five mice at a time on a 16-channel MRI system with the developed hardware, provides high imaging efficiency for a preclincal DCE-MRI protocol. For example, by preparing a set of five mice on one sled while another set is being scanned on another sled, minimal scanner down time will result. Imaging more than five mice simultaneously will likely result in dominance by animal preparation time rather than the imaging protocol time.

	Protocol Scans								Timing			Result	
	1	**2**	**3**	**4**	**5**	**6**	**7**	**8**	**Scan**	**Setup**	**True**	***N***	***T***
Single	00:01.6	00:03.2	01:52.0	01:52.0	04:16.0	03:24.0	09:54.0	04:16.0	25:38.8	04:00.0	29:38.0	1	1.00
Multiple	00:03.2	00:12.8	00:59.5	00:59.5	02:19.0	01:42.0	09:54.0	02:19.0	18:26.0	05:18.0	23:44.0	5	6.24

Table 5.3: Protocol timing and throughput estimates for the scans

Mouse	231	235	234	233	235	232	231	234	218	211	219
Start Time	11:27	13:17	13:41	14:11	9:15	9:40	10:14	10:38	11:14	11:38	14:00
End Time	11:32	13:21	13:45	14:15	9:19	9:44	10:18	10:43	11:18	11:42	14:04
Prep [min]	5	4	4	4	4	4	4	5	4	4	4

Table 5.4: Mouse preparation time from initial anesthetization to catheterization

Chapter 6: Contributions and Future Work

6.1 Summary of Contributions

DCE-MRI permits efficient preclinical evaluation of experimental cancer therapies in small animal models such as mice. Unfortunately, the lengthy protocol limits scanning to only a few animals per day with conventional imaging techniques. This throughput limitation can be prohibitive to investigators, particularly because of the substantial cost for imaging and inability to scan all mice near a common longitudinal time point. The primary goal of this work was to develop and evaluate a multi-animal imaging system for demonstrating throughput-optimized improvement of a preclinical DCE-MRI protocol. The hypothesis that throughput could be improved by more than the number of animals scanned at once, compared to traditional single-animal imaging methods, was tested and confirmed in three specific aims.

The first aim was to simulate a variety of multi-animal coil configurations to determine a throughput-optimized imaging system with up to 16 independent receive elements. By evaluating throughput capabilities based on parallel imaging performance, an array system for simultaneously scanning five mice was selected. The MARCs system included five independent coil assemblies that each consisted of a single transmit volume coil and a three-element receive subarray. RF shielding of individual transmit volume coils provided a means to limit coil sensitivities to individual VOIs and reduced the impact of artifacts and aliasing caused by PI that would take place in a more highly coupled array structure. Based on the maximum g-factor as a function of imaging throughput, configuration V was selected for its ability to maintain low g-factors for throughputs that exceeded the number of animals scanned at once.

The second aim of this study was to carefully design and manufacture the array system and to test imaging performance of the multi-animal array against conventional mouse imaging hardware. Methods to maximize coil SNR and minimize coupling were evaluated and implemented. Ancillary PIN diode switching drivers and a Wilkinson power divider, required for integration with the 7-T Biospec system that has only one transmitter, were designed and manufactured. Each of the coil subassemblies was placed within a dedicated coil holder that distributed DC power and active decoupling signals. The combination of overlap and preamplifier decoupling provided at least 29 dB of intra-array isolation. By including RF shielding in conjunction with overlap and preamplifier decoupling, inter-array decoupling was more than 45 dB. Imaging performance was tested *in situ* on phantoms using unaccelerated and PI-accelerated acquisition schemes. The resulting SNR was compared with that from a conventional mouse imaging coil with significant improvements realized when using the multi-mouse array system. In particular, a SNR that is more than twice that from the reference birdcage coil can be achieved with a throughput improvement of five. For applications where it is appropriate to trade SNR for imaging speed with parallel imaging, throughput can be improved by more than nine-fold while maintaining image quality comparable or exceeding that of the standard birdcage coil.

The third and final aim was to develop a multi-animal DCE-MRI protocol and to determine the actual protocol throughput achieved by using the array system. All but the first two acquisitions of the multi-animal protocol utilized PI for efficient scanning. For the T_1-weighted, T_2-weighted, and T_1-mapping acquisitions, PI permitted reduced acquisition times by nearly a factor of two. PI was used to improve temporal resolution of the DCE-MRI acquisition while relaxing the gradient duty cycle to avoid gradient

heating. The multi-animal DCE-MRI acquisition balanced temporal resolution with gradient compliance, but resulted in an increase in image SNR compared with the single-animal protocol. A dual-tracer method was employed (102) to demonstrate parallel multi-animal DCE-MRI. Based on protocol execution times, this study proves that data from routine DCE-MRI studies can be acquired at a substantially increased rate ($T > N$) without sacrificing SNR. For other imaging protocols that do not have a long fixed-duration acquisition, higher throughput improvements are possible.

The imaging system and techniques developed in this work have laid the foundation for advanced preclinical imaging without the typical hindrances of MRI, including low throughput and high costs. By improving overall efficiency, preclinical MRI becomes a viable tool for solving a new class of biological problems: ones that can benefit from MRI technology but have not included imaging in the past due to cost or complexity of scheduling large cohorts of animals. The impact of this work also has clinical implications since reducing the time for preclinical drug assessment ultimately results in faster deployment into the clinic.

6.2 Limitations and Future Work

Although careful attention was placed on the simulation, design, testing, and animal experiments in this work, there are some potential limitations and room for future improvements that must be noted. The MRI system the multi-animal array was designed for only has a single transmitter, which requires splitting the transmit power among the five channels at the expense of maximum available transmit power. Fortunately, the RF pulses of the standard single-animal protocol require relatively low power, reducing impact on this work. Additionally, unequal loading of the fix-tuned transmit coils and non-ideal performance of the Wilkinson power splitter inherently result in an unequal

distribution of transmit power and true flip angle values because only one level of transmit power can be applied for any given scan. By including variable attenuators in line with the transmit RF ports, RF pulse flip angles could be more carefully controlled. An ideal system architecture would include multi-channel transmit capability, which would enable independent transmit calibration for each animal and restore the 7-dB loss due to power splitting.

To reduce the gradient heating that is introduced when encoding a mouse-sized FOV with a gradient designed for larger subjects, PI was employed in the fixed-duration dynamic acquisition. PI was not used in the conventional sense to speed up the acquisition because a fixed-duration is required to monitor contrast uptake in tumor tissue. Instead, the gradient duty cycle was reduced by requiring fewer phase encoding steps to accurately reconstruct each image. Further improvements that exploit the ability to undersample the spatiotemporal data are also possible and will be investigated in future work.

In this work, the respiratory motion of the mice was monitored to determine the stability of the animals and to influence the adjustment of anesthesia gas that was delivered to each animal. However, it is also well known that anesthesia will reduce body temperature. We integrated circulating heated water into the multi-animal sled to increase the mouse body temperature, but did not incorporate temperature feedback measurements in this initial proof of concept study. Others have shown that changes in subject temperature can alter the perfusion as measured by DCE-MRI (103,104). Therefore, a robust measurement of PK parameters will require a more rigorous multi-animal vital sign monitoring system.

DCE-MRI analysis based on single-tracer injections is highly dependent on accurate estimation of the AIF (27). With traditional estimation methods, such as manual identification of voxels in the location of blood vessels, accurate AIF measurement in mice is complex. For instance, mice have a low blood volume and rapid cardiovascular cycle, which contribute to low SNR, partial volume effects, and flow artifacts. For these reasons, a dual-tracer approach was implemented, however the cost of the BPA is high and it is not currently translatable to the clinic. Therefore, optimized single-tracer methods would be preferred.

Instead of using a conventional AIF sampling technique, a new approach that utilizes a constrained reconstruction to estimate the AIF at a higher sampling rate can be used (101). Such a scheme aims to sample the AIF in the heart, a region where many confounding artifacts can be controlled. Unfortunately, the subarray coils of the current system have been designed to be sensitive to a single tumor or organ and would not support this technique except in a limited number of animal models. However, the volume coils in this work have also been designed to operate in transmit-receive mode, providing opportunities to alternate sampling between the tumor tissue with the receive array and the heart with the volume coil. For example, seven slices can be prescribed over the tumor and a single slice prescribed through the heart for AIF measurement. Such functionality will require additional ancillary hardware to control active decoupling as a function of both slice number and the transmit/receive state of the acquisition.

Filling gradient coils with multiple VOIs can lead to nonlinear gradient fields and distortions that are not equal between all mice. The central mouse has a better gradient linearity than ones in the periphery. For functional studies such as DCE-MRI where the analysis takes place over a temporal series, slight nonlinearities are not a major cause for

concern. However if the target application shifted to something such as tumor volume measurement, gradient linearity could easily be corrected. Furthermore, higher-order shimming over several volumes is a topic that should also be investigated further. The scans of this study were of high bandwidth, but pulse sequences requiring a narrow linewidth may require the integration of separate gradient and shim coils for each animal.

In this work, acquisitions and calculations to achieve accurate SNR comparisons were meticulously performed. A persistent and unexpected anomaly occurred through evaluating the SNR gain of the multi-animal imaging system with respect to the commercial birdcage coil. In particular, a 14% larger SNR gain was detected with spin-echo-based acquisitions compared with gradient-echo acquisitions. It is not expected to depend on the underlying sequence. The root cause of this discrepancy is either coupling of the coils and/or preamplifiers with the gradient coils or DC biasing discrepancies due to ground loops and is presently being investigated. Nonetheless, this minor deviation does not affect the overall goal to not sacrifice high-throughput SNR compared to the standard single-animal imaging configuration.

This study was performed under the assumption that 16 channels on a small-animal MRI system is state-of-the-art. To our knowledge, there are no experimental small-animal MRI systems that have actually been equipped with such a 16-channel receiver system from the manufacturer. If, or rather when, small-animal systems with more than 16 channels become available, another analysis of the optimal number of animals scanned at once and the number of array elements to dedicate to each animal should be performed. We have anticipated the jump to systems with more than 16 channels and have thus left the current modular system open for expansion to seven-mouse acquisitions. The future will tell if high-throughput applications will drive the

market for more receive channels on small-animal systems as PI has for clinical MRI systems.

Multi-animal imaging with a system similar to the one developed in this work may become a common tool that will promote the use of MRI in routine preclinical investigations. This is particularly true for research sites with limited budgets that may not be able to invest in a dedicated small-animal MRI system, and that rely on clinical systems for preclinical imaging research. Clinical systems, although typically of a lower field strength, offer the advantages of a large bore real estate, many receive channels, and sequences that are optimized for a large gradient set which can be easily translated for human imaging. To best utilize the available bore space while reducing the time spent imaging animals on a clinical system, a combination of multi-animal and parallel imaging techniques should be used.

For sites that already possess dedicated small-animal research systems, incorporating MARCs into the system should only require the addition of receiver channels and the one-time cost of the multi-animal coil and support hardware. To be feasible to sites worldwide, the development of a commercially available product will be required. Our research group is working with Bruker Biospin to commercialize this technology.

6.3 CONCLUSION

In conclusion, a throughput-optimized 20-coil array system for simultaneously imaging five mice has been simulated, manufactured, tested on phantoms, and used to demonstrate a high-throughput preclinical DCE-MRI protocol. An overall throughput of more than six was demonstrated without a loss in SNR in the target anatomy, compared with imaging using the conventional hardware. The combination of multiple-mouse MRI

and parallel imaging enables high levels of throughput, while keeping the number of mice at a manageable level. This system will lower the barriers for imaging in preclinical research and enable more thorough sampling of pathologies that evolve rapidly in time. Through future development and commercialization of high-throughput imaging systems, the cycle for drug development may be significantly shortened, and the clinical translation of experimental therapies and image-based biomarkers for robust detection and rapid evaluation of response to therapy, has the potential to broadly impact clinical care.

Appendix A: Scattering Parameters

To avoid complications in measuring matrix parameters in terms of currents and voltages at RF frequencies, a set of parameters called scattering parameters (or *S*-parameters) can be used to describe electrical networks. Consider a basic two-port network with incident wave voltage a_1 and reflective wave voltage b_1 at the input (port 1) and corresponding wave voltages a_2 and b_2 at the output (port 2). The *S*-parameters are complex variables relating the incident wave to the reflective wave, that are governed by (105):

$$b_1 = S_{11}a_1 + S_{12}a_2 \qquad (A-1)$$

$$b_2 = S_{21}a_1 + S_{22}a_2\,. \qquad (A-2)$$

The *S*-parameter given by the reflection coefficient Γ_1 at port 1 with $a_2 = 0$ is:

$$\Gamma_1 = S_{11} = \left.\frac{b_1}{a_1}\right|_{a_2=0}, \qquad (A-3)$$

the transmission coefficient T_{21} from port 1 to port 2 with $a_2 = 0$ is:

$$\mathrm{T}_{21} = S_{21} = \left.\frac{b_2}{a_1}\right|_{a_2=0}, \qquad (A-4)$$

the reflection coefficient Γ_2 at port 2 with $a_1 = 0$ is:

$$\Gamma_2 = S_{22} = \left.\frac{b_2}{a_2}\right|_{a_1=0}, \qquad (A-5)$$

and the transmission coefficient T_{12} from port 2 to port 1 with $a_1 = 0$ is:

$$\mathrm{T}_{12} = S_{12} = \left.\frac{b_1}{a_2}\right|_{a_1=0}. \qquad (A-6)$$

For a general *N*-port network, *S*-parameters of the form S_{xy} represent transmission coefficients from port y to port x, while *S*-parameters of the form S_{xx} represent reflection

coefficients at port *x*. For RF circuitry with $Z_0 = 50\ \Omega$, reflection coefficients of zero are achieved if the port is perfectly matched to 50Ω. Perfect reflextion coefficients (i.e. with linear gain = 1) correspond to 0 dB.

Appendix B: Matlab Reconstruction Code

```
%%%%%%%%%%%%%%%%%%%%%%%%%%%%%%%%%%%%%%%%%%%%%%%%%%%%%%%%%%
function MarcGRAPPA_v2(directory, varargin)


%% Read PI-accelerated data

if(directory(end)~='/')
    directory = [directory '/'];
end

lengthdir = length(directory); %% make compatible with script
directory = directory(1:(lengthdir - 8))

output.acqp = readBrukerHeader([directory 'acqp']);
output.method = readBrukerHeader([directory 'method']);
output.reco = readBrukerHeader([directory '/pdata/1/reco']);
output.visu_pars = readBrukerHeader([directory '/pdata/1/visu_pars']);

ref = -1*(output.method.PVM_Matrix(2)/2):1:((output.method.PVM_Matrix(2)/2)-1);
PEsteps = output.method.PVM_EncSteps1;
for I = length(PEsteps):-1:1,
    [J(I),index(I)] = find(PEsteps(I) == ref);
end


%% Format radw data
f = fopen([directory 'fid'],'r','l');
fid1 = fread(f,inf,'int32');
fclose(f);
nCoils = output.method.PVM_EncNReceivers;
nslices = output.method.PVM_SPackArrNSlices;
sliceOrder = output.method.PVM_ObjOrderList + 1;
nr = output.method.PVM_NRepetitions;
nro = output.method.PVM_Matrix(1);
npe_full = output.method.PVM_Matrix(2);
npe = output.method.PVM_EncMatrix(2);


meth = output.method.Method
R = output.method.PVM_EncPpiAccel1;
if (length(meth) == 7)
    if (meth == 'RAREVTR')
        rareF = output.method.PVM_RareFactor;
        nT1 = output.method.NumT1Exps;
        fid2 = reshape(fid1,[2,nro,nCoils,rareF,nslices,npe/rareF,nT1]);
        fid2 = squeeze(fid2(1,:,:,:,:,:,:) + i*fid2(2,:,:,:,:,:,:));
        if (nslices > 1)
            fid2 = permute(fid2,[1 2 3 5 4 6]);
        end
        fid2 = reshape(fid2,[nro,nCoils,npe,nslices,nT1]);
        fid = zeros(nro,nCoils,npe_full,nslices,nT1);
        fid(:,:,index,sliceOrder,:) = fid2;
        fid = permute(fid,[1 3 2 4 5]);
        nr = nT1;
    end
    if (meth == 'fSPGRv2')
        fid2 = reshape(fid1,[2,nro,nCoils,nslices,npe,nr]);

        %fid2 = squeeze(fid2(1,:,:,:,:,:)+i*fid2(2,:,:,:,:,:));
```

```
        fid2 = fid2(1,:,:,:,:,:) + i*fid2(2,:,:,:,:,:);
        fid2 = reshape(fid2,[size(fid2,2) size(fid2,3) size(fid2,4) size(fid2,5) size(fid2,6)]);

        fid2 = permute(fid2,[1 4 2 3 5]);
        fid = zeros(nro,npe_full,nCoils,nslices,nr);
        fid(:,index,:,sliceOrder,1:nr) = fid2;
        item = 0;
    end
elseif (length(meth) == 4)
    if (meth == 'RARE')
        rareF = output.method.PVM_RareFactor;
        fid2 = reshape(fid1,[2,nro,nCoils,rareF,nslices,npe/rareF,nr]);

        %fid2 = squeeze(fid2(1,:,:,:,:,:) + i*fid2(2,:,:,:,:,:));
        fid2 = fid2(1,:,:,:,:,:,:) + i*fid2(2,:,:,:,:,:,:);
        fid2 = reshape(fid2,[size(fid2,2) size(fid2,3) size(fid2,4) size(fid2,5) size(fid2,6) size(fid2,7)]);

        fid2 = permute(fid2,[1 2 3 5 4 6]);
        fid2 = reshape(fid2,[nro,nCoils,npe,nslices,nr]);
        fid = zeros(nro,nCoils,npe_full,nslices,nr);
        sizefid2 = size(fid2)
        sizefid = size(fid)
        fid(:,:,index,sliceOrder,:) = fid2;
        fid = permute(fid,[1 3 2 4 5]);
    end
    if (meth == 'MSME')
        fid2 = reshape(fid1,[2,nro,nCoils,nslices,npe,nr]);

        %fid2 = squeeze(fid2(1,:,:,:,:,:)+i*fid2(2,:,:,:,:,:));
        fid2 = fid2(1,:,:,:,:,:) + i*fid2(2,:,:,:,:,:);
        fid2 = reshape(fid2,[size(fid2,2) size(fid2,3) size(fid2,4) size(fid2,5) size(fid2,6)]);
        sizefid2 = size(fid2)

        fid2 = permute(fid2,[1 4 2 3 5]);
        fid = zeros(nro,npe_full,nCoils,nslices,nr);
        size(fid)
        sizefid2 = size(fid2)
        sizefid = size(fid)
        fid(:,index,:,sliceOrder,:) = fid2;
    end
    item = 0;
end


%% GRAPPA
frame = nr*nslices;
for reps = nr:-1:1, % for each series of repetitions
    for slice = nslices:-1:1, %and all slic
        frame % display to user
        frame = frame - 1; %run
        % Perform acceleration loop
        nCoils = nCoils;
        kgrappa(:,:,1:nCoils) = squeeze(fid(:,:,1:nCoils,slice,reps)); % work on one coil at a time
        kg = kgrappa; % kg is like kgrappa, accumulation is here? %should not have the acs lines
        temp = kgrappa(1,:,1,1); %% see which lines have data
        list = temp;
        I = find(temp~=0);    % find indicies where have data
        nAcqPE = length(I);
        if (reps == 1)&&(slice == 1) % account for unaccelerated data
            Reff = npe_full/nAcqPE
        end
        startInd = I(1);
        if startInd > 1 %choose correct stepping line
```

```
   first = startInd - 1;
else
   first = startInd + 1;
end
kg(:,first:R:end,:) = zeros(size(kg(:,first:R:end,:))); % start with empty missing rows
if R ~= 1,
   temp(startInd:R:end) = 0; % isolate ACS lines
end
origVals = zeros(size(temp));
origVals(startInd:R:end) = 1;  %% indicies where encoded
M = find(origVals == 1);
second2last = M(end-1);
ACS = find(temp~=0); % the set of ACS lines
if (reps == 1)&&(slice == 1)
   numACSlines = length(ACS); % display only once to user
end
extent = floor(.1*nro/2); %% how far to travel along ro line ... may reduce for noise was .96
stepVals = (round(nro/2)-extent):1:(round(nro/2)+extent); % consecutive RO pts to calibrate on
kgrappa = permute(kgrappa, [2 1 3]);
kg2 = permute(kg, [2 1 3]); %% to perform convolution on
for coils = 1:nCoils, % reconstruct images for each coil
   list = 1:nCoils;
   for set = 1:1:(R-1), %% use sets for each missing set of lines
      Ncols = length(ACS)/(R-1); %how many times to calibrate
      x = zeros(nCoils*3*2,1); % size of the GRAPPA kernal (expanded to one row/column)
      BB = zeros(size(x')); % initialize where result will be
      y = zeros((Ncols*length(stepVals)),1);
      B = zeros((Ncols*length(stepVals)), 2, 3, nCoils);
      count = 1;
      for acs = ACS(set:(R-1):end), % for every iacs line set
         J = find(origVals(1:(acs-1)) ~= 0);
         leftVal = J(end);
         K = find(origVals((acs+1):end) ~= 0);
         rightVal = K(1)+acs;
         if count == 1,
            vec = [leftVal acs rightVal];
            vec = vec - acs*ones(size(vec));
         end
         for step = stepVals,
            smallcount = 0;
            B(count, 1:2, 1:3, 1:nCoils) = kgrappa([leftVal rightVal], (step-1):1:(step+1), list(1:nCoils));
            list(1:nCoils);
            y(count,1) = kgrappa(acs,step, coils);
            count = count + 1;
         end
      end
      B = reshape(B, (Ncols*length(stepVals)),(nCoils*3*2));
      x = pinv(B)*y; %% decide grappa coefficients for a particular coil

      % now write data back into accumulation
      x2 = reshape(x,[2 3 nCoils]);
      kernel = zeros(3,3,3);
      kernel([3 1],:,:) = x2([1 2],end:-1:1,:);
      kernel(2,2,coils) = 1;
      ktot = conv2(kernel(:,:,1),kg2(:,:,1)) + conv2(kernel(:,:,2),kg2(:,:,2)) + conv2(kernel(:,:,3),kg2(:,:,3));
      ktot = ktot(2:(end-1),2:(end-1));
      kg(:,:,coils) = permute(ktot,[2 1]);
   end
end
kgrappa = permute(kgrappa, [2 1 3]);
kg(:,ACS,:) = kgrappa(:,ACS,:);% Add back original ACS lines
for coils = 1:nCoils,
   im(:,:,coils) = fft2c(kg(:,:,coils));
```

```
      end

      % perform sum of square recon
      square = im.*conj(im);
      sosimR = sqrt(squeeze(sum(square(:,:,:),3)));
      %figure;imshow(abs(sosimR),[])
      Images(:,:,slice,reps) = sosimR;
      CoilImages(:,:,:,slice,reps) = abs(im);
   end
end

%% account for PV display

CoilImages = CoilImages(end:-1:1,end:-1:1,:,:,:);
Images = Images(end:-1:1,end:-1:1,:,:);

%% write image data for PV

dim3 = nslices*nr;
Images2 = reshape(Images,[nro,npe_full,dim3]);
maxval = max(max(max(max(max(max(Images))))))
for I = dim3:-1:1,
   im3 = conj(squeeze(Images2(:,:,I))');
   max(max(max(im3)));
   min(min(min(im3)));
   mean(mean(mean(im3)));
   Images3(:,:,I) = 2^15*abs(im3)/maxval;
end
Images4 = reshape(Images3,[nro*npe_full*dim3 1]);
%Images4 = 2^15*Images4/max(max(max(Images4)));
f = fopen([directory '/pdata/1/2dseq'],'w');
fwrite(f,Images4,'int16');
fclose(f);

%% write visu_pars file
frames = output.visu_pars.VisuCoreFrameCount;
minimum = output.visu_pars.VisuCoreDataMin;
maximum = output.visu_pars.VisuCoreDataMax;

fin = fopen([directory '/pdata/1/visu_pars']);
fout = fopen([directory '/pdata/1/visu_pars2'],'w');

while ~feof(fin)
   s = fgetl(fin);
   for I = 1:frames,
      text = sprintf('%d',maximum(I));
      s = regexprep(s,text,'32768');
   end
   fprintf(fout,'%s \n',s);
   %disp(s);
end

fclose(fin);
fclose(fout);

%% clean up directory
copyfile([directory '/pdata/1/visu_pars'],[directory '/pdata/1/visu_pars.bak']);
delete([directory '/pdata/1/visu_pars']);
copyfile([directory '/pdata/1/visu_pars2'],[directory '/pdata/1/visu_pars']);
delete([directory '/pdata/1/visu_pars2']);
```

```
%%%%%%%%%%%%%%%%%%%%%%%%%%%%%%%%%%%%%%%%%%%%%%%%%%%%%%%%%%%%%%%%%%%

function MarcGRAPPA_v2dynamic(directory, varargin)


%% Read PI-accelerated data

if(directory(end)~='/')
    directory = [directory '/'];
end

lengthdir = length(directory); %% make compatible with script
directory = directory(1:(lengthdir - 8))

output.acqp = readBrukerHeader([directory 'acqp']);
output.method = readBrukerHeader([directory 'method']);
output.reco = readBrukerHeader([directory '/pdata/1/reco']);
output.visu_pars = readBrukerHeader([directory '/pdata/1/visu_pars']);

ref = -1*(output.method.PVM_Matrix(2)/2):1:((output.method.PVM_Matrix(2)/2)-1);
PEsteps = output.method.PVM_EncSteps1;
for I = length(PEsteps):-1:1,
    [J(I),index(I)] = find(PEsteps(I) == ref);
end


%% Format radw data
f = fopen([directory 'fid'],'r','l');
fid1 = fread(f,inf,'int32');
fclose(f);
nCoils = output.method.PVM_EncNReceivers;
nslices = output.method.PVM_SPackArrNSlices;
sliceOrder = output.method.PVM_ObjOrderList + 1;
nr = output.method.PVM_NRepetitions;
nro = output.method.PVM_Matrix(1);
npe_full = output.method.PVM_Matrix(2);
npe = output.method.PVM_EncMatrix(2);


meth = output.method.Method
R = output.method.PVM_EncPpiAccel1;
if (length(meth) == 7)
    if (meth == 'RAREVTR')
        rareF = output.method.PVM_RareFactor;
        nT1 = output.method.NumT1Exps;
        fid2 = reshape(fid1,[2,nro,nCoils,rareF,nslices,npe/rareF,nT1]);
        fid2 = squeeze(fid2(1,:,:,:,:,:,:) + i*fid2(2,:,:,:,:,:,:));
        if (nslices > 1)
            fid2 = permute(fid2,[1 2 3 5 4 6]);
        end
        fid2 = reshape(fid2,[nro,nCoils,npe,nslices,nT1]);
        fid = zeros(nro,nCoils,npe_full,nslices,nT1);
        fid(:,:,index,sliceOrder,:) = fid2;
        fid = permute(fid,[1 3 2 4 5]);
        nr = nT1;
    end
    if (meth == 'fSPGRv2')
        fid2 = reshape(fid1,[2,nro,nCoils,nslices,npe,nr]);
        fid2 = squeeze(fid2(1,:,:,:,:,:)+i*fid2(2,:,:,:,:,:));
        fid2 = permute(fid2,[1 4 2 3 5]);
        fid = zeros(nro,npe_full,nCoils,nslices,nr);
        fid(:,index,:,sliceOrder,1:nr) = fid2;
```

```
        item = 0;
    end
elseif (length(meth) == 4)
    if (meth == 'RARE')
        rareF = output.method.PVM_RareFactor;
        fid2 = reshape(fid1,[2,nro,nCoils,rareF,nslices,npe/rareF]);
        fid2 = squeeze(fid2(1,:,:,:,:,:) + i*fid2(2,:,:,:,:,:));
        fid2 = permute(fid2,[1 2 3 5 4]);
        fid2 = reshape(fid2,[nro,nCoils,npe,nslices]);
        fid = zeros(nro,nCoils,npe_full,nslices);
        fid(:,:,index,sliceOrder) = fid2;
        fid = permute(fid,[1 3 2 4]);
    end
    if (meth == 'MSME')
        fid2 = reshape(fid1,[2,nro,nCoils,nslices,npe,nr]);
        fid2 = squeeze(fid2(1,:,:,:,:,:)+i*fid2(2,:,:,:,:,:));
        fid2 = permute(fid2,[1 4 2 3 5]);
        fid = zeros(nro,npe_full,nCoils,nslices);
        fid(:,index,:,sliceOrder) = fid2;
    end
    item = 0;
end


%% GRAPPA
frame = nr*nslices;
for reps = nr:-1:1, % for each series of repetitions
    for slice = nslices:-1:1, %and all slic
        frame % display to user
        % Perform acceleration loop
        nCoils = nCoils;
        kgrappa(:,:,1:nCoils) = squeeze(fid(:,:,1:nCoils,slice,reps)); % work on one coil at a time
        kg = kgrappa; % kg is like kgrappa, accumulation is here? %should not have the acs lines
        temp = kgrappa(1,:,1,1); %% see which lines have data
        list = temp;
        I = find(temp~=0);    % find indicies where have data
        nAcqPE = length(I);
        if (reps == 1)&&(slice == 1) % account for unaccelerated data
            Reff = npe_full/nAcqPE
        end
        startInd = I(1);
        if startInd > 1 %choose correct stepping line
            first = startInd - 1;
        else
            first = startInd + 1;
        end
        kg(:,first:R:end,:) = zeros(size(kg(:,first:R:end,:))); % start with empty missing rows
        if R ~= 1,
            temp(startInd:R:end) = 0; % isolate ACS lines
        end
        origVals = zeros(size(temp));
        origVals(startInd:R:end) = 1;  %% indicies where encoded
        M = find(origVals == 1);
        second2last = M(end-1);
        ACS = find(temp~=0); % the set of ACS lines
        if (reps == 1)&&(slice == 1)
            numACSlines = length(ACS); % display only once to user
        end
        extent = floor(.1*nro/2); %% how far to travel along ro line ... may reduce for noise was .96
        stepVals = (round(nro/2)-extent):1:(round(nro/2)+extent); % consecutive RO pts to calibrate on
        kgrappa = permute(kgrappa, [2 1 3]);
        kg2 = permute(kg, [2 1 3]); %% to perform convolution on
        for coils = 1:nCoils, % reconstruct images for each coil
```

```
        list = 1:nCoils;
        for set = 1:1:(R-1), %% use sets for each missing set of lines
           Ncols = length(ACS)/(R-1); %how many times to calibrate
           x = zeros(nCoils*3*2,1); % size of the GRAPPA kernal (expanded to one row/column)
           BB = zeros(size(x')); % initialize where result will be
           y = zeros((Ncols*length(stepVals)),1);
           B = zeros((Ncols*length(stepVals)), 2, 3, nCoils);
           count = 1;
           for acs = ACS(set:(R-1):end), % for every iacs line set
              J = find(origVals(1:(acs-1)) ~= 0);
              leftVal = J(end);
              K = find(origVals((acs+1):end) ~= 0);
              rightVal = K(1)+acs;
              if count == 1,
                 vec = [leftVal acs rightVal];
                 vec = vec - acs*ones(size(vec));
              end
              for step = stepVals,
                 smallcount = 0;
                 B(count, 1:2, 1:3, 1:nCoils) = kgrappa([leftVal rightVal], (step-1):1:(step+1), list(1:nCoils));
                 list(1:nCoils);
                 y(count,1) = kgrappa(acs,step, coils);
                 count = count + 1;
              end
           end
           B = reshape(B, (Ncols*length(stepVals)),(nCoils*3*2));
           x = pinv(B)*y; %% decide grappa coefficients for a particular coil

           % now write data back into accumulation
           x2 = reshape(x,[2 3 nCoils]);
           kernel = zeros(3,3,3);
           kernel([3 1],:,:) = x2([1 2],end:-1:1,:);
           kernel(2,2,coils) = 1;
           kernelAccum(:,:,:,coils,slice,reps) = kernel;
           kg2Accum(:,:,:,slice,reps) = kg2;
           kgrappaAccum(:,:,:,slice,reps) = kgrappa;
           kgAccum(:,:,:,slice,reps) = kg;
        end
     end
     frame = frame - 1; %run
  end
end

% Bring convolution out here
frame = nr*nslices;
for reps = nr:-1:1, % for each series of repetitions
   for slice = nslices:-1:1, %and all slic
      frame % display to user
      frame = frame - 1; %run
      kgrappa = squeeze(kgrappaAccum(:,:,:,slice,reps));
      kg2 = squeeze(kg2Accum(:,:,:,slice,reps));
      kg = squeeze(kgAccum(:,:,:,slice,reps));
      % Perform acceleration loop
      for coils = 1:nCoils,
         for set = 1:1:(R-1),
            skA = size(kernelAccum)

            kernelA = squeeze(mean(kernelAccum,6));
            kernel = squeeze(kernelA(:,:,:,coils,slice));
            sizek = size(kernel)
            %kernel = squeeze(kernelAccum(:,:,:,coils,slice,reps)); %% normally would be here
            ktot = conv2(kernel(:,:,1),kg2(:,:,1)) + conv2(kernel(:,:,2),kg2(:,:,2)) + conv2(kernel(:,:,3),kg2(:,:,3));
            ktot = ktot(2:(end-1),2:(end-1));
```

```
            kg(:,:,coils) = permute(ktot,[2 1]);
        end
    end

    kgrappa = permute(kgrappa, [2 1 3]);
    kg(:,ACS,:) = kgrappa(:,ACS,:);% Option to add back original ACS lines
    for coils = 1:nCoils,
        im(:,:,coils) = fft2c(kg(:,:,coils));
    end

    % perform sum of square recon
    square = im.*conj(im);
    sosimR = sqrt(squeeze(sum(square(:,:,:),3)));
    %figure;imshow(abs(sosimR),[])
    Images(:,:,slice,reps) = sosimR;
    CoilImages(:,:,:,slice,reps) = abs(im);
  end
end



%% account for PV display

CoilImages = CoilImages(end:-1:1,end:-1:1,:,:,:);
Images = Images(end:-1:1,end:-1:1,:,:);

%% write image data for PV

dim3 = nslices*nr;
Images2 = reshape(Images,[nro,npe_full,dim3]);
maxval = max(max(max(max(max(max(Images))))))
for I = dim3:-1:1,
  im3 = conj(squeeze(Images2(:,:,I))');
  max(max(max(im3)));
  min(min(min(im3)));
  mean(mean(mean(im3)));
  Images3(:,:,I) = 2^15*abs(im3)/maxval;
end
Images4 = reshape(Images3,[nro*npe_full*dim3 1]);
%Images4 = 2^15*Images4/max(max(max(Images4)));
f = fopen([directory '/pdata/1/2dseq'],'w');
fwrite(f,Images4,'int16');
fclose(f);

%% write visu_pars file
frames = output.visu_pars.VisuCoreFrameCount;
minimum = output.visu_pars.VisuCoreDataMin;
maximum = output.visu_pars.VisuCoreDataMax;

fin = fopen([directory '/pdata/1/visu_pars']);
fout = fopen([directory '/pdata/1/visu_pars2'],'w');

while ~feof(fin)
  s = fgetl(fin);
  for I = 1:frames,
    text = sprintf('%d',maximum(I));
    s = regexprep(s,text,'32768');
  end
  fprintf(fout,'%s \n',s);
  %disp(s);
end
```

```
fclose(fin);
fclose(fout);

%% clean up directory
copyfile([directory '/pdata/1/visu_pars'],[directory '/pdata/1/visu_pars.bak']);
delete([directory '/pdata/1/visu_pars']);
copyfile([directory '/pdata/1/visu_pars2'],[directory '/pdata/1/visu_pars']);
delete([directory '/pdata/1/visu_pars2']);
```

```
%%%%%%%%%%%%%%%%%%%%%%%%%%%%%%%%%%%%%%%%%%%%%%%%%%%%%%%%%%%%%%%%%%%

function im = fft2c(d)
% im = fft2c(d)
%
% fft2c performs a centered fft2
%
im = fftshift(fft2(fftshift(d)));
```

Appendix C: Paravision Macros

%%

% Run_PI_Scan

```
#!/bin/sh

# Get the path name for matlab command
mrpath=`pvcmd -a pvScan -r pvDsetPath -path PROCNO`

# Change from User Mode to FT Mode
pvcmd -set pvScan RECO_mode FT_MODE

# Run the GOP
pvcmd -a pvScan pvStartGop -Control -Alt

# Wait until acquisition is over
pvcmd -s `pvcmd -a pvScan -r pvDsetPath -path PROCNO`

# Might need to wait until recon is over??

# Change to directory for matlab scripts
cd /home/mramirez/Scripts/

# Perform a silent matlab recon and overwrite 2dseq and displayparam
files
matlab -nojvm -nosplash -nodesktop -r "MarcGRAPPA_v2('$mrpath'); quit"

# Send reconstructed data to first display window
pvcmd -a xtip tWomActvWdw 1

pvcmd -a xtip tDsLoad $mrpath
```

%%%%%%%%%%%%%%%%%%%%%%%%%%%%%%%%%%%

% Run_PI_Scan_Dynamic

```
#!/bin/sh

# Get the path name for matlab command
mrpath=`pvcmd -a pvScan -r pvDsetPath -path PROCNO`

# Change from User Mode to FT Mode
pvcmd -set pvScan RECO_mode FT_MODE

# Run the GOP
pvcmd -a pvScan pvStartGop -Control -Alt

# Wait until acquisition is over
pvcmd -s `pvcmd -a pvScan -r pvDsetPath -path PROCNO`

# Might need to wait until recon is over??

# Change to directory for matlab scripts
cd /home/mramirez/Scripts/

# Perform a silent matlab recon and overwrite 2dseq and displayparam
files
matlab -nojvm -nosplash -nodesktop -r "MarcGRAPPA_v2dynamic('$mrpath');
quit"

# Send reconstructed data to first display window
pvcmd -a xtip tWomActvWdw 1
pvcmd -a xtip tDsLoad $mrpath
```

%%%%%%%%%%%%%%%%%%%%%%%%%%%%%%%%%%%%%%%

% PI_Recon

```
#!/bin/sh

# Determine path for matlab argument
mrpath=`pvcmd -a pvScan -r pvDsetPath -path PROCNO`

# Change to Matlab files directory
cd /home/mramirez/Scripts/

# Quietly excecute recon and overwrite files
matlab -nojvm -nosplash -nodesktop -r "MarcGRAPPA_v2('$mrpath'); quit"

# Send reconstructed image to display
pvcmd -a xtip tWomActvWdw 1
pvcmd -a xtip tDsLoad $mrpath
```

%%

% PI_Recon_Dynamic

```
#!/bin/sh

# Determine path for matlab argument
mrpath=`pvcmd -a pvScan -r pvDsetPath -path PROCNO`

# Change to Matlab files directory
cd /home/mramirez/Scripts/

# Quietly excecute recon and overwrite files
matlab -nojvm -nosplash -nodesktop -r "MarcGRAPPA_v2dynamic('$mrpath');
quit"

# Send reconstructed image to display
pvcmd -a xtip tWomActvWdw 1
pvcmd -a xtip tDsLoad $mrpath
```

References

1. Kransdorf MJ, Murphey MD. Radiologic evaluation of soft-tissue masses: a current perspective. Ajr 2000;175(3):575-587.
2. Hoshi Y. Functional near-infrared optical imaging: utility and limitations in human brain mapping. Psychophysiology 2003;40(4):511-520.
3. Gibson AP, Hebden JC, Arridge SR. Recent advances in diffuse optical imaging. Phys Med Biol 2005;50(4):R1-43.
4. Lauterbur PC. Image formation by induced local interactions. Examples employing nuclear magnetic resonance. 1973. Letters to Nature 1973;242:190-191.
5. Padhani AR. MRI for assessing antivascular cancer treatments. The British journal of radiology 2003;76 Spec No 1:S60-80.
6. Padhani AR, Husband JE. Dynamic contrast-enhanced MRI studies in oncology with an emphasis on quantification, validation and human studies. Clinical radiology 2001;56(8):607-620.
7. Heron MP, Hoyert DL, Murphy SL, Xu JQ, Kochanek KD, Tejada-Vera B. Deaths: Final data for 2006. National vital statistics reports. Volume 57. Hyattsville, MD: National Center for Health Statistics; 2009.
8. Bandettini PA, Wong EC, Hinks RC, Tikofsky RS, Hyde JS. Time course EPI of human brain function during task activation. Magn Reson Med 1992;25:390-398.
9. van Dijk P. ECG-triggered NMR imaging of the heart. Diagnostic imaging in clinical medicine 1984;53(1):29-37.
10. Choyke PL, Frank JA, Girton ME, Inscoe SW, Carvlin MJ, Black JL, Austin HA, Dwyer AJ. Dynamic Gd-DTPA-enhanced MR imaging of the kidney: experimental results. Radiology 1989;170(3 Pt 1):713-720.
11. Tieleman A, Deblaere K, Van Roost D, Van Damme O, Achten E. Preoperative fMRI in tumour surgery. European radiology 2009;19(10):2523-2534.
12. Kuittinen T, Husso-Saastamoinen M, Sipola P, Vuolteenaho O, Ala-Kopsala M, Nousiainen T, Jantunen E, Hartikainen J. Very acute cardiac toxicity during BEAC chemotherapy in non-Hodgkin's lymphoma patients undergoing autologous stem cell transplantation. Bone marrow transplantation 2005;36(12):1077-1082.
13. Choyke PL, Dwyer AJ, Knopp MV. Functional tumor imaging with dynamic contrast-enhanced magnetic resonance imaging. J Magn Reson Imaging 2003;17(5):509-520.
14. Verstraete KL, Van der Woude HJ, Hogendoorn PC, De-Deene Y, Kunnen M, Bloem JL. Dynamic contrast-enhanced MR imaging of musculoskeletal tumors: basic principles and clinical applications. J Magn Reson Imaging 1996;6(2):311-321.

15. Cha S, Johnson G, Wadghiri YZ, Jin O, Babb J, Zagzag D, Turnbull DH. Dynamic, contrast-enhanced perfusion MRI in mouse gliomas: correlation with histopathology. Magn Reson Med 2003;49(5):848-855.
16. McDonald DM, Baluk P. Significance of blood vessel leakiness in cancer. Cancer research 2002;62(18):5381-5385.
17. Tofts PS. Modeling tracer kinetics in dynamic Gd-DTPA MR imaging. J Magn Reson Imaging 1997;7(1):91-101.
18. Orth RC, Bankson J, Price R, Jackson EF. Comparison of single- and dual-tracer pharmacokinetic modeling of dynamic contrast-enhanced MRI data using low, medium, and high molecular weight contrast agents. Magn Reson Med 2007;58(4):705-716.
19. Evelhoch JL. Key factors in the acquisition of contrast kinetic data for oncology. J Magn Reson Imaging 1999;10(3):254-259.
20. Walker-Samuel S, Leach MO, Collins DJ. Evaluation of response to treatment using DCE-MRI: the relationship between initial area under the gadolinium curve (IAUGC) and quantitative pharmacokinetic analysis. Physics in medicine and biology 2006;51(14):3593-3602.
21. Li X, Rooney WD, Springer CS, Jr. A unified magnetic resonance imaging pharmacokinetic theory: intravascular and extracellular contrast reagents. Magn Reson Med 2005;54(6):1351-1359.
22. Tofts PS, Brix G, Buckley DL, Evelhoch JL, Henderson E, Knopp MV, Larsson HB, Lee TY, Mayr NA, Parker GJ, Port RE, Taylor J, Weisskoff RM. Estimating kinetic parameters from dynamic contrast-enhanced T(1)-weighted MRI of a diffusable tracer: standardized quantities and symbols. J Magn Reson Imaging 1999;10(3):223-232.
23. Roberts C, Issa B, Stone A, Jackson A, Waterton JC, Parker GJ. Comparative study into the robustness of compartmental modeling and model-free analysis in DCE-MRI studies. J Magn Reson Imaging 2006;23(4):554-563.
24. Kneeshaw PJ, Turnbull LW, Smith A, Drew PJ. Dynamic contrast enhanced magnetic resonance imaging aids the surgical management of invasive lobular breast cancer. Eur J Surg Oncol 2003;29(1):32-37.
25. O'Connor JP, Jackson A, Parker GJ, Jayson GC. DCE-MRI biomarkers in the clinical evaluation of antiangiogenic and vascular disrupting agents. British journal of cancer 2007;96(2):189-195.
26. Hara N, Okuizumi M, Koike H, Kawaguchi M, Bilim V. Dynamic contrast-enhanced magnetic resonance imaging (DCE-MRI) is a useful modality for the precise detection and staging of early prostate cancer. The Prostate 2005;62(2):140-147.
27. Pickup S, Zhou R, Glickson J. MRI estimation of the arterial input function in mice. Academic radiology 2003;10(9):963-968.

28. Mouridsen K, Christensen S, Gyldensted L, Ostergaard L. Automatic selection of arterial input function using cluster analysis. Magn Reson Med 2006;55(3):524-531.
29. Yankeelov TE, Luci JJ, Lepage M, Li R, Debusk L, Lin PC, Price RR, Gore JC. Quantitative pharmacokinetic analysis of DCE-MRI data without an arterial input function: a reference region model. Magnetic resonance imaging 2005;23(4):519-529.
30. McConville P, Moody JB, Moffat BA. High-throughput magnetic resonance imaging in mice for phenotyping and therapeutic evaluation. Curr Opin Chem Biol 2005;9(4):413-420.
31. Henderson E, Rutt BK, Lee TY. Temporal sampling requirements for the tracer kinetics modeling of breast disease. Magnetic resonance imaging 1998;16(9):1057-1073.
32. Aref M, Handbury JD, Xiuquan Ji J, Aref S, Wiener EC. Spatial and temporal resolution effects on dynamic contrast-enhanced magnetic resonance mammography. Magnetic resonance imaging 2007;25(1):14-34.
33. Radjenovic A, Ridgway JP, Smith MA. A method for pharmacokinetic modelling of dynamic contrast enhanced MRI studies of rapidly enhancing lesions acquired in a clinical setting. Phys Med Biol 2006;51(9):N187-197.
34. Blaimer M, Breuer F, Mueller M, Heidemann RM, Griswold MA, Jakob PM. SMASH, SENSE, PILS, GRAPPA: how to choose the optimal method. Top Magn Reson Imaging 2004;15(4):223-236.
35. Griswold MA, Jakob PM, Heidemann RM, Nittka M, Jellus V, Wang J, Kiefer B, Haase A. Generalized autocalibrating partially parallel acquisitions (GRAPPA). Magn Reson Med 2002;47(6):1202-1210.
36. Griswold MA, Jakob PM, Nittka M, Goldfarb JW, Haase A. Partially parallel imaging with localized sensitivities (PILS). Magn Reson Med 2000;44(4):602-609.
37. Kyriakos WE, Panych LP, Kacher DF, Westin CF, Bao SM, Mulkern RV, Jolesz FA. Sensitivity profiles from an array of coils for encoding and reconstruction in parallel (SPACE RIP). Magn Reson Med 2000;44(2):301-308.
38. Sodickson DK, Manning WJ. Simultaneous acquisition of spatial harmonics (SMASH): fast imaging with radiofrequency coil arrays. Magn Reson Med 1997;38(4):591-603.
39. Pruessmann KP, Weiger M, Scheidegger MB, Boesiger P. SENSE: sensitivity encoding for fast MRI. Magn Reson Med 1999;42(5):952-962.
40. Roemer PB, Edelstein WA, Hayes CE, Souza SP, Mueller OM. The NMR phased array. Magn Reson Med 1990;16(2):192-225.
41. Bock NA, Konyer NB, Henkelman RM. Multiple-mouse MRI. Magn Reson Med 2003;49(1):158-167.
42. Schneider JE, Bose J, Bamforth SD, Gruber AD, Broadbent C, Clarke K, Neubauer S, Lengeling A, Bhattacharya S. Identification of cardiac malformations

in mice lacking Ptdsr using a novel high-throughput magnetic resonance imaging technique. BMC Dev Biol 2004;4(1):16.
43. Lazovic J, Stojkovic DS, Collins CM, Yang QX, Vaughan JT, Smith MB. Hexagonal zero mode TEM coil: a single-channel coil design for imaging multiple small animals. Magn Reson Med 2005;53(5):1150-1157.
44. Xu S, Gade TP, Matei C, Zakian K, Alfieri AA, Hu X, Holland EC, Soghomonian S, Tjuvajev J, Ballon D, Koutcher JA. In vivo multiple-mouse imaging at 1.5 T. Magn Reson Med 2003;49(3):551-557.
45. Koutcher JA, Hu X, Xu S, Gade TP, Leeds N, Zhou XJ, Zagzag D, Holland EC. MRI of mouse models for gliomas shows similarities to humans and can be used to identify mice for preclinical trials. Neoplasia (New York, NY 2002;4(6):480-485.
46. Matsuda Y, Utsuzawa S, Kurimoto T, Haishi T, Yamazaki Y, Kose K, Anno I, Marutani M. Super-parallel MR microscope. Magn Reson Med 2003;50(1):183-189.
47. Bock NA, Nieman BJ, Bishop JB, Henkelman RM. In vivo multiple-mouse MRI at 7 Tesla. Magn Reson Med 2005;54(5):1311-1316.
48. Bock NA, Zadeh G, Davidson LM, Qian B, Sled JG, Guha A, Henkelman RM. High-resolution longitudinal screening with magnetic resonance imaging in a murine brain cancer model. Neoplasia 2003;5(6):546-554.
49. Nieman BJ, Bock NA, Bishop J, Sled JG, Josette Chen X, Mark Henkelman R. Fast spin-echo for multiple mouse magnetic resonance phenotyping. Magn Reson Med 2005;54(3):532-537.
50. Bishop J, Feintuch A, Bock NA, Nieman B, Dazai J, Davidson L, Henkelman RM. Retrospective gating for mouse cardiac MRI. Magn Reson Med 2006;55(3):472-477.
51. Esparza-Coss E, Ramirez MS, Bankson JA. Wireless self-gated multiple-mouse cardiac cine MRI. Magn Reson Med 2008;59(5):1203-1206.
52. Ramirez MS, Ragan DK, Kundra V, Bankson JA. Feasibility of multiple-mouse dynamic contrast-enhanced MRI. Magn Reson Med 2007;58(3):610-615.
53. Spraggins TA. Wireless retrospective gating: application to cine cardiac imaging. Magnetic resonance imaging 1990;8(6):675-681.
54. Kim D, Kellman P. Improved cine displacement-encoded MRI using balanced steady-state free precession and time-adaptive sensitivity encoding parallel imaging at 3 T. NMR in biomedicine 2007;20(6):591-601.
55. Kim WS, Mun CW, Kim DJ, Cho ZH. Extraction of cardiac and respiratory motion cycles by use of projection data and its applications to NMR imaging. Magn Reson Med 1990;13(1):25-37.
56. Ramirez MS, Bankson JA. A practical method for 2D multiple-animal MRI. J Magn Reson Imaging 2007;26(4):1162-1166.

57. Beuf O, Jaillon F, Saint-Jalmes H. Small-animal MRI: signal-to-noise ratio comparison at 7 and 1.5 T with multiple-animal acquisition strategies. Magma 2006;19(4):202-208.
58. Bernardo M, Kobayashi H, Metzger G, Koyama Y, Shaw C, Thomasson D, Choyke P. In-vivo multiple mouse MRI using parallel receive-only coils on a 3.0 T clinical scanner for molecular imaging research. In: Proceedings of the 14th Annual Meeting of ISMRM, Seattle, WA, USA 2003.
59. Ramirez MS, Esparza-Coss E, Bankson JA. Multiple-mouse MRI with multiple arrays of receive coils. Magn Reson Med 2010;63(3):803-810.
60. Bishop JE, Spring S, Dazai J, Chugh BP, Portnoy S, Suddarth S, Morris GR, Henkelman RM. Multiple mouse imaging of 16 live mice. In: Proceedings of the 16th Annual Meeting of ISMRM. Toronto, Ontario, Canada: International Society for Magnetic Resonance in Medicine; 2008.
61. Schwartz DL, Bankson JA, Lemos R, Jr., Lai SY, Thittai AK, He Y, Hostetter G, Demeure MJ, Von Hoff DD, Powis G. Radiosensitization and stromal imaging response correlates for the HIF-1 inhibitor PX-478 given with or without chemotherapy in pancreatic cancer. Mol Cancer Ther 2010;9(7):2057-2067.
62. Canet D. Nuclear Magnetic Resonance: Concepts and Methods. New York: John Wiley & Sons; 1996.
63. Haacke EM, Brown RW, Thompson MR, Venkatesan R. Magnetic Resonance Imaging: Physical Principles and Sequence Design. New York, NY: John Wiley & Sons, Inc.; 1999.
64. Jin J. Electromagnetic Analysis and Design. Boca Raton, FL: CRC Press; 1999.
65. Nishimura DG. Principles of Magnetic Resonance Imaging: Lulu; 2010.
66. Grissom WA, Xu D, Kerr AB, Fessler JA, Noll DC. Fast large-tip-angle multidimensional and parallel RF pulse design in MRI. IEEE Trans Med Imaging 2009;28(10):1548-1559.
67. Bracewell RN. Strip integration in radio astronomy. Aust J Phys 1956;9:198-217.
68. Breuer FA, Kannengiesser SA, Blaimer M, Seiberlich N, Jakob PM, Griswold MA. General formulation for quantitative G-factor calculation in GRAPPA reconstructions. Magn Reson Med 2009;62(3):739-746.
69. Lee TH. The Design of CMOS Radio-Frequency Integrated Circuits. New York, NY: Caimbridge University Press; 1998.
70. Bankson JA, Wright SM. Multi-channel magnetic resonance spectroscopy through time domain multiplexing. Magnetic resonance imaging 2001;19(7):1001-1008.
71. Wiggins GC, Polimeni JR, Potthast A, Schmitt M, Alagappan V, Wald LL. 96-Channel receive-only head coil for 3 Tesla: design optimization and evaluation. Magn Reson Med 2009;62(3):754-762.
72. Schmitt M, Potthast A, Sosnovik DE, Polimeni JR, Wiggins GC, Triantafyllou C, Wald LL. A 128-channel receive-only cardiac coil for highly accelerated cardiac MRI at 3 Tesla. Magn Reson Med 2008;59(6):1431-1439.

73. McDougall MP, Wright SM. 64-channel array coil for single echo acquisition magnetic resonance imaging. Magn Reson Med 2005;54(2):386-392.
74. Hardy CJ, Giaquinto RO, Piel JE, Rohling KW, Marinelli L, Blezek DJ, Fiveland EW, Darrow RD, Foo TK. 128-channel body MRI with a flexible high-density receiver-coil array. J Magn Reson Imaging 2008;28(5):1219-1225.
75. Sutton BP, Ciobanu L, Zhang X, Webb A. Parallel imaging for NMR microscopy at 14.1 Tesla. Magn Reson Med 2005;54(1):9-13.
76. Schneider JE, Lanz T, Barnes H, Medway D, Stork LA, Lygate CA, Smart S, Griswold MA, Neubauer S. Ultra-fast and accurate assessment of cardiac function in rats using accelerated MRI at 9.4 Tesla. Magn Reson Med 2008;59(3):636-641.
77. Korn M. A 6-Element Coil Array for Parallel Imaging in Arbirtary Directions. The 16th Annual ISMRM Scientific Meeting & Exhibition. Toronto, Canada: The International Society for Magnetic Resonance in Medicine; 2008.
78. Mogatadakala KV, Bankson JA, Narayana PA. Three-element phased-array coil for imaging of rat spinal cord at 7T. Magn Reson Med 2008;60(6):1498-1505.
79. Doty FD, Entzminger G, Kulkarni J, Pamarthy K, Staab JP. Radio frequency coil technology for small-animal MRI. NMR Biomed 2007;20(3):304-325.
80. Ginefri JC, Poirier-Quinot M, Girard O, Darrasse L. Technical aspects: development, manufacture and installation of a cryo-cooled HTS coil system for high-resolution in-vivo imaging of the mouse at 1.5 T. Methods (San Diego, Calif 2007;43(1):54-67.
81. Chin C-L, Collins CM, Li S, Dardzinski BJ, Smith MB. BirdcageBuilder: Design of specified-geometry birdcage coils with desired current pattern and resonant frequency. Concepts in Magnetic Resonance Part B: Magnetic Resonance Engineering 2002;15(2):156-163.
82. Lee RF, Giaquinto RO, Hardy CJ. Coupling and decoupling theory and its application to the MRI phased array. Magn Reson Med 2002;48(1):203-213.
83. Wu B, Zhang X, Qu P, Shen GX. Capacitively decoupled tunable loop microstrip (TLM) array at 7 T. Magn Reson Imaging 2007;25(3):418-424.
84. Zhang X, Webb A. Design of a capacitively decoupled transmit/receive NMR phased array for high field microscopy at 14.1T. J Magn Reson 2004;170(1):149-155.
85. Wu B, Wang C, Krug R, Kelley DA, Xu D, Pang Y, Banerjee S, Vigneron DB, Nelson SJ, Majumdar S, Zhang X. 7T human spine imaging arrays with adjustable inductive decoupling. IEEE Trans Biomed Eng 2010;57(2):397-403.
86. Reykowski A, Wright SM, Porter JR. Design of matching networks for low noise preamplifiers. Magn Reson Med 1995;33(6):848-852.
87. Ohliger MA, Sodickson DK. An introduction to coil array design for parallel MRI. NMR Biomed 2006;19(3):300-315.
88. Avdievich NI, Hetherington HP. 4 T actively detunable transmit/receive transverse electromagnetic coil and 4-channel receive-only phased array for (1)H human brain studies. Magn Reson Med 2004;52(6):1459-1464.

89. Lanz T, Muller M, Barnes H, Neubauer S, Schneider JE. A high-throughput eight-channel probe head for murine MRI at 9.4 T. Magn Reson Med 2010;64(1):80-87.
90. Hyde JS, Rilling RJ, Jesmanowicz A. Passive decoupling of surface coils by pole insertion Journal of Magn Reson 1990;89(3):485-495.
91. Wright SM, Wald LL. Theory and application of array coils in MR spectroscopy. NMR Biomed 1997;10(8):394-410.
92. Wang Z, Wang J, Detre JA. Improved data reconstruction method for GRAPPA. Magn Reson Med 2005;54(3):738-742.
93. van Vaals JJ, Brummer ME, Dixon WT, Tuithof HH, Engels H, Nelson RC, Gerety BM, Chezmar JL, den Boer JA. "Keyhole" method for accelerating imaging of contrast agent uptake. J Magn Reson Imaging 1993;3(4):671-675.
94. Gui D, Tsekos NV. Dynamic imaging of contrast-enhanced coronary vessels with a magnetization prepared rotated stripe keyhole acquisition. J Magn Reson Imaging 2007;25(1):222-230.
95. Tsao J, Boesiger P, Pruessmann KP. k-t BLAST and k-t SENSE: dynamic MRI with high frame rate exploiting spatiotemporal correlations. Magn Reson Med 2003;50(5):1031-1042.
96. Kellman P, Epstein FH, McVeigh ER. Adaptive sensitivity encoding incorporating temporal filtering (TSENSE). Magn Reson Med 2001;45(5):846-852.
97. Breuer FA, Kellman P, Griswold MA, Jakob PM. Dynamic autocalibrated parallel imaging using temporal GRAPPA (TGRAPPA). Magn Reson Med 2005;53(4):981-985.
98. Fabien N, Fusco A, Santoro M, Barbier Y, Dubois PM, Paulin C. Description of a human papillary thyroid carcinoma cell line. Morphologic study and expression of tumoral markers. Cancer 1994;73(8):2206-2212.
99. Gule MK, Chen Y, Sano D, Frederick MJ, Zhou G, Zhao M, Milas ZL, Galer CE, Henderson YC, Jasser SA, Schwartz DL, Bankson JA, Myers JN, Lai SY. Targeted therapy of VEGFR2 and EGFR significantly inhibits growth of anaplastic thyroid cancer in an orthotopic murine model. Clin Cancer Res;17(8):2281-2291.
100. Kety SS. The theory and applications of the exchange of inert gas at the lungs and tissues. Pharmacological reviews 1951;3(1):1-41.
101. Ragan DK, Lai SY, Bankson JA. Fast, reproducible measurement of the vascular input function in mice using constrained reconstruction and cardiac sampling. NMR Biomed.
102. Weissleder R, Cheng HC, Marecos E, Kwong K, Bogdanov A, Jr. Non-invasive in vivo mapping of tumour vascular and interstitial volume fractions. Eur J Cancer 1998;34(9):1448-1454.
103. Ludemann L, Wust P, Gellermann J. Perfusion measurement using DCE-MRI: implications for hyperthermia. Int J Hyperthermia 2008;24(1):91-96.

104. Craciunescu OI, Blackwell KL, Jones EL, Macfall JR, Yu D, Vujaskovic Z, Wong TZ, Liotcheva V, Rosen EL, Prosnitz LR, Samulski TV, Dewhirst MW. DCE-MRI parameters have potential to predict response of locally advanced breast cancer patients to neoadjuvant chemotherapy and hyperthermia: a pilot study. Int J Hyperthermia 2009;25(6):405-415.
105. Chang K, editor. Microwave Solid-State Circuits and Applications. New York: John Wiley & Sons, Inc.; 1994. 442 p.

Vita

Marc Stephen Ramirez was born in Houston, TX on August 28, 1980 to parents Jose and Gloria Ramirez. He graduated from Clements High School in Sugar Land, TX in 1998, after which he attended the University of Texas at Austin. In 2002, Marc graduated from UT Austin with a Bachelors of Science in Electrical Engineering. He then went on to obtain his Master of Science in Electrical Engineering in 2004 from Stanford University, where his interest and foundation in medical imaging systems were formed. Shortly after graduation, Marc joined The University of Texas M. D. Anderson Cancer Center as a research engineer under the supervision of Dr. James A. Bankson and continued in that capacity for three years before transitioning back to a graduate student in the UT Department of Biomedical Engineering. Marc married Carly Boone Ramirez in March of 2010. He and Carly currently have a wonderful son, Ryder Boone Ramirez.

Permanent address (or email): 7118 Wandering Lake Ln., Missouri City, TX, 77459; marcram@stanfordalumni.org

This dissertation was typed by Marc Stephen Ramirez.